UNIVERSIDADE FEDERAL DO RIO GRANDE DO NORTE
CENTRO DE TECNOLOGIA
PROGRAMA DE PÓS-GRADUAÇÃO EM ENGENHARIA ELÉTRICA E DE COMPUTAÇÃO

Wavelet-Based Directional Protection Supported by a Wavelet-Based Fault Classifier

Mônica Maria Leal

Supervisor: Prof. Dr. Flavio Bezerra Costa

Doctoral Thesis presented to the Graduate Program in Electrical and Computer Engineering of UFRN (concentration area: Automation and Systems) as part of the requirements for obtaining the title of Doctor of Science.

PPgEEC Order Number: D274
Natal, RN, August 2020

Universidade Federal do Rio Grande do Norte - UFRN

Sistema de Bibliotecas - SISBI

Catalogação da Publicação na Fonte - Biblioteca Central Zila Mamede

Leal, Mônica Maria.
Wavelet-Based Directional Protection Supported by a Wavelet-Based Fault Classifier. - 2020.
115 f.:il.

Federal University of Rio Grande do Norte. Center of Technology. Graduate Program in Electrical and Computer Engineering. Natal, RN, 2020
Supervisor: Flavio Bezerra Costa.

1. Directional protection. 2. Fault classifier. 3. Wavelet transform. 4. Clarke transform. 5. Transmission line protection. I. Costa, Flávio Bezerra. II. Título.

RN/UF/BCZM

To my parents, Manoel Cecílio e Maria Elvira, for the great dedication that surpasses any distance and to my husband, Pedro Araújo Medeiros, for the unconditional love.

Acknowledgment

To God for the support, strength and perseverance in the moments I needed.

To my parents, Manoel Cecílio Leal and Maria Elvira Leal, for teaching me to overcome barriers in order to achieve greater conquests, and to my siblings, Majela Maria Leal and Marciel Manoel Leal, for their continuous support.

To my husband, Pedro Araújo Medeiros, for his companionship, patience, love and essential dedication to develop this work.

To my advisor, professor Flavio Bezerra Costa, for his dedicated guidance throughout this challenging journey.

To my friends at the ProRedes laboratory, Frankelene Pinheiro, Jessika Fonseca, Marcos Sérgio, Rafael Lucas, Dénis Keuton, Rodrigo Prado, Cícero Josean and Max Rodrigues, for the shared friendship and for all the help provided for this work to be carried out.

To the Coordination for the Improvement of Higher Education Personnel (Coordenação de Aperfeiçoamento de Pessoas de Nível Superior - Capes) for the financial support during the execution of this work.

To sum it up, to all of those who, directly or indirectly, contributed in a constructive way to the development of this work.

Abstract

Fast and accurate protections are required to ensure the safety of the power system. In this research, a new directional protection based on wavelet transfom is described by using only the first wavelet decomposition level. The scaling coefficients are used in replacement of the Fourier transform in order to recreate the conventional directional protection. The torque equations were mathematically redefined in the wavelet domain by using sampled voltages and currents. Regarding the protection activation, the wavelet coefficients are used for fast detection of fault-induced transients (wavelet activators) in order to reduce the relay operating time, whereas the scaling coefficients are used for backup activation in accordance with the overcurrent protection (wavelet overcurrent activators). Evaluations have proved the feasibility to rebuild the conventional directional protection by using the real-time stationary wavelet transform (RT-SWT), which has provided better performance and faster operating time than the conventional protection based on the discrete Fourier transform (DFT). As new functionalities to the directional protection, the wavelet-based negative sequence unit can be used to identify the fault directionality to three-phase faults, even with severe voltage sags without memory strategies, which is not possible with the conventional protection. In addition, a real-time fault classification method using the real time boundary stationary wavelet transform (RT-BSWT) applied to modal components of the Clarke transform was developed to support the directional protection. The proposed classifier uses a simple threshold-based logic flow and requires three-phase current measurements from only one terminal. Furthermore, by using the wavelet coefficients energy of RT-BSWT, this classifier is fast and accurate due to the extraction of high-frequency components and the border effect. The fault classifier results have shown it is accurate and fast to identify all of the ten fault types successfully supporting the directional protection needs.

Keywords: Directional protection, fault classifier, wavelet transform, Clarke transform, transmission line protection.

Resumo

Para garantir a segurança do sistema de potência é essencial proteger o sistema de forma rápida e precisa. Neste trabalho, uma proteção direcional baseada na transformada *wavelet* é apresentada usando apenas o primeiro nível de decomposição da tranformada. Os coeficientes escalas são usados como substitutos para a transformada de Fourier a fim de recrIar a proteção direcional convencional. As equações de torque foram matematicamente redefinidas para o domínio *wavelet* usando tensões e correntes amostradas. Com respeito a ativação da proteção, os coeficientes *wavelet* são usados para uma rápida detecção dos transitórios induzidos pela falta a fim de reduzir o tempo de operação do relé, enquanto que os coeficientes escalas são usados como ativador de *backup* de acordo com a proteção de sobrecorrente. Avaliações provaram a viabilidade de reconstruir a proteção direcional convencional pelo uso da transformada wavelet discreta redundante (TWDR) e mostraram a rápida operação da proteção proposta comparada à proteção direcional tradicional baseada na transformada de Fourier. Como nova funcionalidade da proteção direcional, a unidade de sequência negativa pode ser usada para identificar a direcionalidade das faltas trifásicas mesmo diante de um severo afundamento de tensão sem o uso de memória adicional, como é realizado na proteção convencional. Além disso, um classificador de faltas usando transformada *wavelet* discreta redundante - TWDR com bordas aplicado as componentes modais de Clarke foi desenvolvido para dar suporte à proteção direcional. A metodologia proposta utiliza um simples fluxo lógico baseado em limiares e requer as medições de correntes de apenas um terminal. O uso das energias dos coeficientes *wavelets* da TWDR com bordas implica num método rápido e preciso devido à extração dos componentes de alta frequência e do efeito de borda. Os resultados sobre o classificador de faltas comprovam a potencialidade do classificador em identificar corretamente todos os dez tipos de faltas de forma rápida e precisa dando o suporte necessário para a proteção direcional proposta.

Palavras-chave: Proteção direcional, classificador de faltas, transformada *wavelet*, proteção de linhas de transmissão.

Table of Contents

List of Figures

List of Tables

List of Abbreviations and Acronyms

AC	Alternative Current
A/D	Analog-to-Digital
ANN	Artificial Neural Network
ANSI	American National Standards Institute
BPNN	Back Propagation Neutral Network
BSWT	Boundary Stationary Wavelet Transform
CCVT	Coupling Capacitor Voltage Transform
CT	Current Transform
CWT	Continuous Wavelet Transform
Chesf	Companhia Hidrelétrica do São Francisco
DC	Direct Current
DFIG	Doubly-fed Induction Generator
DFT	Discrete Fourier Transform
DG	Distribution Generation
DL	Double Line
DLG	Double Line-to-ground
DSP	Digital Signal Processor
DT	Decision Tree
DWT	Discrete Wavelet Transform
EHV	Extra-High Voltage
ELM	Extremely Learning Machine
FIR	Finite Impulse Response
HSA	Harmonic Search Algorithm
HVDC	High Voltage Direct Current
IIR	Infinite Impulse Response
IMF	Intrinsic Mode Functions
LLL	Three-phase
MFQL	Modified Fuzzy Q Learning
MM	Modulos Maxima
MODWT	Maximal Overlap Discrete Wavelet Transform
MRA	Wavelet Multiresolution Analysis
MWP	Multiwavelet Packet
PMSG	Permanent Magnet Synchronous Generator
PSD	Power Spectral Density
PWT	Packet Wavelet Transform
RT-BSWT	Real-Time Boundary Stationary Wavelet Transform
RT-SWT	Real-Time Stationary Wavelet Transform
SDV	Singular Decomposition Valuer
SLG	Single Line-to-ground

SNR	Signal-to-Noise Ratio
ST	S-transform
SVD	Singular Value Decomposition
SVM	Support Vector Machine
SWT	Stationary Wavelet Transform
VT	Voltage Transform
WMA	Wavelet Multiresolution Analysis
WSE	Wavelet Singular Entropy

List of Symbols

α Angular lag of 120°.
α^2 Angular lag of 240°.
Δk Number of samples into a cycle.
Δk_α Angular lag equivalent to 120° in time.
Δk_{α^2} Angular lag equivalent to 240° in time.
Δk_{Z_0} Angle displacement particle as a function of the zero sequence line impedance angle.
Δk_{Z_1} Angle displacement particle as a function of the positive sequence line impedance angle.
$\mathscr{E}_A^0$ Normalized zero energy.
$\mathscr{E}_A^\alpha$ Normalized αA energy.
$\mathscr{E}_B^\alpha$ Normalized αB energy.
$\mathscr{E}_C^\alpha$ Normalized αC energy.
$\mathscr{E}_{base}^w$ Total α-mode energy.
$\mathscr{E}_{i_0}^w$ Wavelet coefficients energy from i_0.
$\mathscr{E}_{i_{\alpha A}}^w$ Wavelet coefficients energy from $i_{\alpha A}$.
$\mathscr{E}_{i_{\alpha B}}^w$ Wavelet coefficients energy from $i_{\alpha B}$.
$\mathscr{E}_{i_{\alpha C}}^w$ Wavelet coefficients energy from $i_{\alpha C}$.
ε_{op} Threshold used to enhance the reliability of the directional units.
$\mathscr{E}_x^{sa}$ Scaling coefficients energy from boundary coefficients of signal x.
$\mathscr{E}_x^s$ Scaling coefficients energy of signal x.
$\mathscr{E}_x^w$ Wavelet coefficients energy of signal x.
f Fundamental frequency.
f_s Sampling frequency.
h_ϕ Low-pass IIR filter.
$\bar{h}_\phi$ Inverse IIR low-pass filter.
h_ψ IIR high-pass filter.
$\bar{h}_\psi$ Inverse IIR high-pass filter.
$\mathbf{I}_0$ Current zero sequence components in frequency domain.
i_0 Current zero sequence components in time domain to phase A.
$i_{0\alpha\beta}$ Current zero components from Clarke transform.
$\mathbf{I}_{1A}$ Current positive sequence components in frequency domain to phase A.
i_{1A} Current positive sequence components in time domain to phase A.
$\mathbf{I}_{1B}$ Current positive sequence components in frequency domain to phase B.
i_{1B} Current positive sequence components in time domain to phase B.
$\mathbf{I}_{1C}$ Current positive sequence components in frequency domain to phase C.
i_{1C} Current positive sequence components in time domain to phase C.
$\mathbf{I}_{2A}$ Current negative sequence components in frequency domain to phase A.
i_{2A} Current negative sequence components in time domain to phase A.
$\mathbf{I}_{2B}$ Current negative sequence components in frequency domain to phase B.
i_{2B} Current negative sequence components in time domain to phase B.
$\mathbf{I}_{2C}$ Current negative sequence components in frequency domain to phase C.

i_{2C} Current negative sequence components in time domain to phase C.
$\mathbf{I}_A$ Current phasor to phase A.
i_A Current samples to phase A.
i_{α_A} Current α components from Clarke transform with phase A reference.
i_{α_B} Current α components from Clarke transform with phase B reference.
i_{α_C} Current α components from Clarke transform with phase C reference.
$\mathbf{I}_B$ Current phasor to phase B.
i_B Current samples to phase B.
i_{β_A} Current β components from Clarke transform with phase A reference.
i_{β_B} Current β components from Clarke transform with phase B reference.
i_{β_C} Current β components from Clarke transform with phase C reference.
$\mathbf{I}_C$ Current phasor to phase C.
i_C Current samples to phase C.
I_{op} Currents from operating quantities.
I_{ph} Phase or sequence current phasor.
I_{ph_r} Reference of current.
$I_{un_{50}}$ Instantaneous pickup current.
$I_{un_{51}}$ Time-delay pickup current.
j Decomposition level.
k Current sampling.
L Wavelet and scaling filter length.
PF^s Scaling power factor.
P^s Scaling active power.
s Scaling coefficient.
s_j Scaling coefficients in j decomposition level.
S^s Scaling apparent power.
s_x Scaling coefficients in the fist decomposition level of signal x.
T_{51} Instant associated to the time-delay overcurrent unit being transposed.
$\tilde{T}_{op}$ Torque factor.
TMS Time multiplier settings.
T_{op} Torque provided from directional formulation.
$\tilde{T}^s_{op}$ Scaling torque factor.
T_P Time request to activate the time-delay overcurrent protection.
$\mathbf{V}_0$ Voltage zero sequence components in frequency domain.
v_0 Voltage zero sequence components in time domain to phase A.
$\mathbf{V}_{1A}$ Voltage zero sequence components in frequency domain.
v_{1A} Voltage positive sequence components in time domain to phase A.
$\mathbf{V}_{1B}$ Voltage positive sequence components in frequency domain to phase B.
v_{1B} Voltage positive sequence components in time domain to phase B.
$\mathbf{V}_{1C}$ Voltage positive sequence components in frequency domain to phase C.
v_{1C} Voltage positive sequence components in time domain to phase C.
$\mathbf{V}_{2A}$ Voltage negative sequence components in frequency domain to phase A.
v_{2A} Voltage negative sequence components in time domain to phase A.
$\mathbf{V}_{2B}$ Voltage negative sequence components in frequency domain to phase B.
v_{2B} Voltage negative sequence components in time domain to phase B.
$\mathbf{V}_{2C}$ Voltage negative sequence components in frequency domain to phase C.
v_{2C} Voltage negative sequence components in time domain to phase C.
V_{pol} Voltage from polarizing quantities.

w Wavelet coefficient.
w_j Wavelet coefficients in j decomposition level.
w_x Wavelet coefficients in the fist decomposition level of signal x.
$\mathbf{X}$ Phasor from a generic signal X.
x Sample from a generic signal x.
X_i Imaginary part of phasor $\mathbf{X}$.
X_r Real part of phasor $\mathbf{X}$.
x_{rms} Root means square of a generic signal x.
$Y_{un_{50}}$ Constant related to the instantaneous overcurrent units.
$Y_{un_{51}}$ Constant related to the time-delay overcurrent units.

Chapter 1

Introduction

The electrical energy has an essential role in the economy progress of the countries as well as in the welfare of contemporary society. Therefore, the power electric system has to assure a high level of reliability in the supply of electricity. However, interruption in the supply can be caused by different electromagnetic phenomena in the power system leading to attain different classes. The interruptions caused by short-circuit (faults) can result from natural or human impact, such as: lightning storm causing a high voltage to flash over the insulators, a high-speed wind causing tree contacts to the energized phases, ice build up on the transmission lines, earthquakes, fire explosions, falling trees, flying objects, physical contact by humans or animals, insulation contamination or vehicle crashing into power line poles or into live equipment. The frequency of fault occurrence varies with time, climate, geographical location, and man-made structure in the surrounding.

The fault current is determined by internal voltages of synchronous machines and by system impedances between the fault and the machine. The fault current magnitude may be several orders larger than the steady-state operating currents and, whether allowed to persist, may cause thermal and/or mechanical damage to equipment. In addition, faults must be cleared fast in order to the system does not lose the transient stability which lead to a possible black out. Therefore, faults need to be removed from the power system as soon as possible in order to offer a safety system, reduce the monetary losses, and follow the normative standards. Protective equipment, such as circuit breakers, fuses, relays, and instrument transformers at an extra-high voltage (EHV) to alternative current (AC) circuits is standardized to clear faults within six cycles (100 ms at 60 Hz) (ONS, 2016) and to the low voltage between 5 to 20 cycles (GLOVER; SARMA; OVERBYE, 2012). However, the aim of the protection is being precise and fast as possible because studies have been proved, for a particular line, one millisecond reduction in the fault clearance time increased the power transfer by 15 MW (SCHWEITZER et al., 2015).

Directional elements are fundamental in both transmission and distribution protection systems in order to provide information of fault direction. For instance, depending on the operative conditions in a mesh system, the overcurrent protection operate in or out of its protective zone. Hence directional overcurrent relays are used to discriminate whether the fault is located in or out of the protective zone. In transmission lines, directional elements are essential for enhancing the selectivity of distance protection or to supervise it (AUDLIN; WARRINGTON, 1943), and can be used in association with the overcurrent backup protection (PEREZ; URDANETA, 1999). In distribution systems with distributed generation, the directional information is even more needed to effectively protect the feeders (MOZINA, 2010).

Some directional protection units, as well other protection algorithms, depend on the knowledge of the fault classification or the fault type selection (PHADKE; IBRAHIM; HLIBKA, 1977; SCHWEITZER et al., 2015) to its correct operation. Therefore, the fault classification must be also as fast, accurate, and reliable as possible in order to not delay the protection

performance. The main reason to properly identify the fault type, which is divided into four categories: single line-to-ground (SLG) fault, double line-to-ground (DLG) fault, line-to-line (LL) fault, and three phases (LLL) fault, is to select different algorithms to deal with different fault situations. The importance to identify beyond the fault type is to supply information about which phases are involved in the fault. Therefore, the fault classification, which are composed by ten categories (AG, BG, CG, ABG, BCG, CAG, AB, BC, CA and ABC), plays an important role satisfying single-pole tripping and autoreclosing requirements (DONG; KONG; CUI, 2009).

Conventionally, directional elements are referred as the code 32 by the American National Standards Institute (IEEE, 1971). These protection units compare the operating current with the polarizing voltage using fundamental phasors computed by the Fourier transform, resulting in trigger for forward faults (ROBERTS; GUZMAN, 1994). A phase selector or a fault classifier is required to identify correctly the directional units suitable to be used in each fault type to avoid misoperation and provide selectivity. The performance of the conventional (Fourier-based) directional protection is usually very reliable. However, Fourier-based algorithms present well-known issues such as the influence of the direct exponential decaying current and the time request for its proper convergence.

Even though directional elements have increased lately its technologies being able to offer a reliable diagnoses within 1 ms through the traveling wave-based directional protection TW32 (SCHWEITZER; KASZTENNY; MYNAM, 2016) and between 2 to 4 ms through the time domain directional protection TD32 (GUZMÁN et al., 2018) to transmission lines, new protection studies and propositions are essential to improve the conventional methodologies and offer a different path to future technologies. In this fashion, the discrete wavelet transform (DWT) and its variants such as the stationary wavelet transform (SWT) have been properly used for accurate and fast fault diagnosis in the real-time power system protection, fault detection, fault classification and fault location (COSTA et al., 2015; OBEID et al., 2017; COSTA; SOUZA; BRITO, 2012a; PERERA; RAJAPAKSE; MUTHUMUNI, 2011). The wavelet transform decomposes a sampled signal into scaling and wavelet coefficients. Most of wavelet-based fault diagnosis and protection functions are based on the wavelet coefficients/wavelet coefficient energies in order to propose non-conventional methods such as applied to transformer or based on traveling waves (COSTA et al., 2017; EISSA, 2005; MEDEIROS; COSTA; SILVA, 2016; BOLLEN; GU, 2007; COSTA et al., 2017). In addition, recently, the conventional overcurrent protection was recreated by using the scaling coefficient energies successfully (COSTA; MONTI; PAIVA, 2017). However, this wavelet-based overcurrent protection is unable to identify the fault direction as required in most practical applications.

Regarding to fault classification, the DWT and SWT have been largely used to extract high-frequency information from power system signals (MALATHI; MARIMUTHU; BASKAR, 2010; BHALJA; MAHESHWARI, 2008; COSTA; SOUZA; BRITO, 2012b; ASHOK; YADAV; ABDELAZIZ, 2019; JAYAMAHA; LIDULA; RAJAPAKSE, 2019; DONG; KONG; CUI, 2009). However, the choice of the mother wavelet and the dumped transients can lead to a mis-classification by using SWT/DWT. Since the real time boundary stationary wavelet transform (RT-BSWT) has been successfully used in fault detection in power transformers (MEDEIROS; COSTA; SILVA, 2016) and in AC current and DC transmission lines (COSTA, 2014b; SILVA et al., 2019), this transform overcomes the mentioned drawbacks which lead to a possible option to a fault classification methodology. Nevertheless, the wavelet coefficient energy of the RT-BSWT was not used for fault classification yet.

1.1 Motivation

Transmission lines are components of the power system that are more susceptible to forced shutdowns due to their large length, which exposes them to all types of disturbances, whether due to human, environmental or operational interference. In a study in a transmission system during 10 years, 99 faults were identified, among which 84 were performed in transmission lines (COURY, 1987) and 80% of the faults in transmission lines were SLG faults (STEVENSON, 1978). Therefore, the greatest motivation of this research is the development of a fast and reliable method for fault directional identification and fault classification to act as fast as possible during a fault in order to avoid the exposition of the power system to overcurrents during large time, hence preventing damage to equipment or people which has interaction with the system, preserving the reliability and continuity of the electric power supply.

1.2 Objectives

The main objectives of this research are to develop a reliable, fast and precise fault classifier and directional protection applied in AC transmission systems by using wavelet transform which are able to attend both conventional and non-conventional trends. The specific objectives are:

- development of an algorithm to correctly identify the fault directionality by using the low-frequency information able to run in real-time;
- development of a fast fault classifier by using only local currents to support the proposed directional protection;
- identification of the most suitable mother wavelet and the utilization of the minimum decomposition level (wavelet version) for these applications;
- evaluation of the fault distance, fault inception angle, fault resistance, system noise, among other effects to these applications;
- implementation of the proposed algorithms in a DSP (digital signal processor) in order to prove its practicability.

1.3 Contributions

The contributions of the thesis are:

- development of a fast and accurate wavelet-based directional protection using low and high frequency information to improve the protection performance;
- development of a fast and accurate fault classification method to support not only the proposed directional protection, but also real-time methods demanding for a reliable classifier.

1.4 Work Methodology

This work was carried out in compliance with the following methodology:

- a revision of the state-of-the-art about fault classifiers and wavelet-based directional protections were carried out in order to understand the challenges still faced by the methodologies presented in the literature.

- some mathematical tools and classical protection principles were studied and recreated to be used into the proposed method and in comparison to it.
- the stationary wavelet transform and the classical directional principles were used to propose a wavelet-based directional protection. The overcurrent functions proposed in (COSTA; MONTI; PAIVA, 2017) were recreated to define a scaling trigger to proposed directional functions.
- the fault classifier present in (COSTA; SOUZA; BRITO, 2012a) was recreated and its limitation identified. A new fault classifier was proposed based on RT-BSWT and Clarke transform.
- Several fault cases were simulated and evaluations carried out to prove the viability of the proposed directional method and additional evaluations were performed to guarantee the well performance of the proposed fault classifier to support the directional protection and solve same drawbacks reported in the literature.

1.5 Work Structure

This thesis is organized in 7 chapters:

- Chapter 1: An introduction about the power system protection and fault classification.
- Chapter 2: A state-of-the-art about directional protections and fault classifiers.
- Chapter 3: A description of the main mathematical tools used in this work.
- Chapter 4: The directional and overcurrent protections principles.
- Chapter 5: The proposed wavelet-based directional protection method by using the conventional directional protection equations.
- Chapter 6: Several results to the wavelet-based directional protection and its comparison to the traditional protection.
- Chapter 7: The proposed fault classifier based on wavelet coefficients energy with border effect and Clarke transform.
- Chapter 8: Several results to the proposed wavelet-based fault classifier and its comparison with an existing wavelet-based method.
- Chapter 9: The conclusions about both methods are enumerated, as well as, some ideas to future works.

Chapter 2

State-of-the-art

This chapter provides a survey of the state-of-the-art of methods developed for directional protection and for a fault classifier based on the wavelet transform. The strengths and weaknesses of these schemes are also highlighted.

2.1 Directional Protection Methods to AC Power Systems

Traditionally, the fault directionality is defined by using the angle between operation current and polarization voltage by using phasors (ZIEGLER, 2011). In the literature, several directional protection methods have been published in accordance with distance and overcurrent protections mainly. The new propositions intend to minimize the shortcomings boosting the respective protections.

By using the DWT, Chen et al. (2003) presented an ultra-fast directional protection applied to transmission lines based on high frequency transients caused by the fault, known as traveling waves. The method requires a modal transformation (Clarke transform) to achieve two independent systems. Therefore, the traveling wave decomposition is made by the Mallat Pyramidal algorithm, once the wavelet B-spline transform does not present phase distortion. The modulus maxima (MM) are used to eliminate the noise and detect, by using the multiplication between the signals, the fault directionality. The method was not affected by the fault resistance or the CCVT (coupling capacitor voltage transform) resolution. However, the method can not be used under critical fault inception angles where transients are difficult to be detected by using DWT. In addition, the presented method may have difficult to identify fault near to bus-bars due to the successively reflection and refraction. In order to increase the protected zone, methods based on traveling wave, require a high sampling rate which demand a high processing and transducers with frequency response appropriate to the application are required implying in additional costs. Chen et al. (2003) did not mention the time required by the protection to offer a reliable fault diagnoses.

Eissa (2004) developed a new directional protection for high voltage bus-bar. The technique acquires voltages and currents from the system at the steady-state. In each sample time the product between the two quantities is made and the sum is accomplished after a cycle which provide the steady-state power flow directionality. In order to identify the directionality during the fault, currents and voltages from the pre-fault period are used into additional formulations. The steady-state directionality defines which formulation has to be used and a sign comparison is made to identify the direction of the fault. CT saturation and high fault resistance did not lead the directional element to misoperate. However, the fault diagnoses are delayed. The fault inception angle or the mother wavelet choice effect were not evaluated. The results are quite restricted since to each evaluation just one fault was performed and Eissa (2004) did not

mention the average time to fault directionality, the time presented are from 2.5 ms to 8.0 ms in punctual cases.

Artificial neural network (ANN) has been largely applied to solve power system issues. Lahiri, Pradhan and Mukhopadhyaya (2005) published an ANN to identify the fault directionality in transmission lines. This work treats the fault direction as a pattern classification problem. The method uses five voltage and current samples from each phase and uses backward and forward faults in two different modules to each phase during the training process. The back-propagation algorithm was used as the training function. Several evaluations were performed to SLG and to DLG faults with fixed fault distance and fault resistance. A DSP implementation was also accomplished. Although this work had achieved good results, ANN needs an expert knowledge in order to build a representative database to the training, which can be difficult to reach since different systems may needed different training.

Eissa (2005) describes the use of packet wavelet transform (PWT) applied to power transformers. Current and voltage measurements are required for this proposal. The product of these signals are processed into a cycle to be computed by the PWT. By using the mother wavelet Haar, which has filters with two coefficients, and the third level of decomposition, the fault directionality could be identified. The results encompass internal and external faults, CT saturation and magnetization inrush effect. Although the evaluated cases under the method achieved a good performance, it was not mentioned the time need to achieve it. By using the third decomposition level some delays may be incorporated to the fault detection and hence to directional diagnostic.

A directional protection applied to bus-bar using DWT was presented by Valsan and Swarup (2007). Voltages and currents were decomposed by the wavelet filter at the first level of decomposition. The high frequency components were extracted to both quantities and the product between filtered current and voltage are computed providing an instantaneous power to each sample and sum is done into a cycle. Finally, the sum is verified whether it is bigger or minor than zero, which defines the directionality. Valsan and Swarup (2007) present results to internal and external faults, transformer energization and CT saturation effects. The mother wavelet Doubechies with six coefficients are used to extract high frequency information. A downsampling by two due to the traditional DWT is performed in each decomposition level leading to a delay in the directionality diagnostic.

Aguilera, Orduna and Ratta (2007), by using travelling waves, presented a directional protection applied to transmission lines based on DWT in order to overcome shortcoming from proposals based on symmetrical components. Therefore, the second level of wavelet decomposition is used to compute energy of the voltage signal which is continuously calculated to verify if there is a fault in the system. Once a fault being detected the current and voltage slopes are computed and compared which leads to the directionality diagnoses. Four fault cases, one zero crossing fault, one close-in fault, one high resistance fault and one evolving faults were evaluated proving a good performance of the method to theses evaluations. In addition, the method is possible to be used in series-compensated lines. Although the presented results were fast and accurate, the method is affected by travelling waves generated by other sources different from the fault.

The correlogram concepts, designed by Eissa and Mahfouz (2012), was a manner to present the autocorrelation coefficients as fault directionality identification and also to inform the fault type applied to transmission lines. This method requires current samples during two cycles which are divided into two different windows being the inputs to the computation of correlogram coefficients. The sign of these coefficients informs the fault directionality and the coefficients magnitude inform the fault type. Although the method was tested under real data

provided from a transmission line (Alberta-Canada), the method requires at least one cycle to correctly inform the fault directionality. In addition, the method was not evaluated varying different fault parameters.

Ukil, Deck and Shah (2012) presented a fault directional protection by using just pre-fault and posfault current information and the reference between these phasors obtained through the recursive discrete Fourier transform. This method requires three buffers to store all the pre-fault angles of the last cycle for each phase, and an additional buffer to store the last two cycles of the angles of maximum changes. In this configuration, directionality is diagnosed from a minimum incidence angle, providing a neutral diagnosis if the fault angle is very close to zero. This method is computationally costly, unfeasible for high sampling rates, and consumes at least two cycles to give the direction diagnosis after the fault occurs. Ukil, Deck and Shah (2012) mentioned that the method presented is not a competitive alternative solution to the traditional directional relays.

Biswal, Pati and Pradhan (2013) developed a method that encompasses problems arising from series-compensated dual circuits. This method requires the current and voltage measurements from the system and performs a phasor estimation using the least squares technique. With the estimated phasors, four classifiers are designed that calculate the angles between: positive sequence current and voltage, pre-fault current positive sequence and fault current, negative sequence current and voltage, and between superimposed positive sequence voltage and current. Therefore, a selection technique is performed providing the directional diagnosis of the fault. The directional technique requires at least a cycle to provide reliable response from the phasor estimator.

Khan and Sidhu (2014) brought the directionality comparison as a protection technique for phase-shifted transformers. The method is based on the positive and negative sequence components. In order to achieve this goal, the DC component were removed by means of a cosine filter and the full cycle DFT is computed to obtain the magnitude and phase of the signals. Gathering this information it is possible to calculate the pre-fault and post-fault sequence components of voltages and currents, hence obtain a sequence impedance containing information from both situations. Therefore, an evaluation of the angle of this impedance is required to define the fault direction. This technique is based on Fourier-based phasor estimation which requires around one cycle to provide reliable information.

With a focus on distributed wind generation, Jones and Kumm (2014) highlighted the problem of non-directional overcurrent protection and created a directional overcurrent module with the objective of detecting fault currents at remote sites. Therefore, the method added to the traditional relay a function that blocks the overcurrent units under heavy system loading. In this way, the positive sequence impedance is verified if it remains in the normal operating zone, otherwise the overcurrent unit is blocked, preventing poor operation of the relay. The evaluation is quite relevant to be added into the traditional directional algorithms to enhance its performance under a future power systems with high penetration of wind turbines and solar photovoltaic inverters. However, some fault parameters or power system conditions can lead the impedance fall within the operate zone during its convergence. Although some delay can be added to assure the correct response, the protection may take more time to work accurately.

A two terminal directional method for transmission lines using transient energy was published by Kong, Zhang and Hao (2015). In this work, the overlapping components are analyzed and the transient power followed by transient energies are computed. The polarities of the energy quantities are used to define fault direction in each relay, sending the signal of opening to the circuit-breaker when the fault is in the protected line. The method was not influenced by the fault inception, the fault type, the fault resistance or the fault distance. Even though the

literature proves that the travelling waves can be completely dumped in zero cross inception angles (COSTA; SOUZA; BRITO, 2012b), the method performed well to these cases. Faults so close to the bus (close-in faults) are a challenge for traveling wave based method due to the successively reflection and refrations which requires a high sampling frequency to protect a large zone.

Saleki, Samet and Ghanbari (2016) developed a directional protection using the k - Nearest Neigbhour algorithm which achieves a high accuracy rate near 8 ms. Based on the cross-relation of the components of the Fourier transform of voltage and current, a neighborhood is considered for convergence. Using the fifth order component of the Fourier transform, the current and voltage signals are treated within a sample window. After that, the cross-correlation function is applied to the components, providing maximum values for each sample. Then a low-pass filter is used to obtain the final signal that will be compared with a defined threshold. The method has some drawbacks, such as the high computational cost and the complexity to exactly understanding leaning process.

Luo et al. (2016) presented a backup directional protection for transmission lines using the reactive energy calculated using the Hilbert transform for high voltage direct current (HVDC) systems. In this technique, the current and voltage data are read from the system and, knowing the parameters of the lines, it is possible to calculate the reactive power, which is only significant in the occurrence of fault. This power is calculated for both ends of the protected line, and then the respective energy quantities are calculated by the discrete Hilbert transform. The product of these energy indicates the fault directionality. Although the method is an innovative manner to detect the directional in HVDC power systems, the method requires two cycles to offer the diagnoses.

Pintos, Moreto and Rolim (2016) proposed a method which extracts from the system only current measurement and performs the phasor estimation by means of the recursive discrete Fourier transform. Therefore, the positive sequence components are calculated and the overcurrent activators are tested. In a fault, the overcurrent is activated and it is observed if there is variation in the sum of the present currents compared to a previous cycle. If the variation exists this information is sent to the relay of the opposite end of the protected line. When the two relays confirm the directionality information, the line is removed from the system. The work alleviates some shortcomings of previous work, but requires a communication system and relies in no synchronization failures.

The new wavelet-based protections published in literature usually explore only the high frequency information. The work developed by Costa, Monti and Paiva (2017) explore both high and low frequency proposing a new overcurrent protection. The low frequency components of the wavelet transform obtained through the scaling coefficients are employed to reconstruct the classical overcurrent protection by means the scaling coefficients energy, it is shown the equivalence of the wavelet method with the traditional phase and neutral protection. In addition, the high frequency components can provide additional information about the fault. In general, the wavelet-based overcurrent protection was equivalent to the classical approach, but with faster fault detection. The approach was not extended the concept to the other units, as a positive and negative sequences. As the aim was overcurrent protection, the fault directionality was not mentioned which restricts the use of this method.

The method created by Samet et al. (2019) requires information from the two previous cycles to detect the fault. The method computes the module of the sample from two previous cycles, the module of the sample from one previous cycle and the module from the difference between the current sample and the sample from the previous cycle. Then, the difference among the three portions are calculated and its result is compared with a empirical threshold based

on the current average during the normal power flow. After the fault being detected, the real instant of the fault occurrence is computed through evaluations of each sample. Then, the fault directionality is achieved through the summation of the multiplications between the real fault sampling and the samples until the fault detection. The method was largely evaluated with simulated and experimental faults achieving 97.1% of accuracy and the direction identification time average was 2.7 ms. Even though Samet et al. (2019) just mentioned the need of a CT with high specification, the complete method uses voltage as an option when face low transients, which would require also a CCVT with high specifications to offer a reliable directionality.

2.2 Fault Classifier Methods for AC Transmission Lines

The power system currents usually present an increase during the fault, and its magnitude (low-frequency information) has been used to identify faulted phases through discrete Fourier transform (DFT)-based phasor (PHADKE; IBRAHIM; HLIBKA, 1977). In a similar fashion, the low-frequency information can be extracted with other techniques, such as the SWT, to verify the magnitude growth in faulted phases. Jung et al. (2007) proposed a SWT-based method using the scaling components (low frequency) on the 4th level decomposition to verify the magnitude growth in the phases involved into the fault. Those methods relies on a significantly changes on the magnitude of currents or voltages during the fault. Although low-frequency information contains features which can be used to classify faults, several fault parameters, e.g: fault distance and resistance, can cause a miss-classification due to the low increase of the fault currents.

In addition to low-frequency information, when a fault takes place upon a transmission line, high frequency electromagnetic transients occur in both voltages and currents. Theses transients have been used to identify which phases are involved in the faults (PRASAD; EDWARD; RAVI, 2018a, 2018b). According to Chen, Huang and He (2016), most fault classification methods are based on artificial intelligence and logic flow. Artificial intelligence is a vast concept which encompasses several techniques, for instance, artificial neural network, support vector machine, fuzzy logic, and decision tree applied to diversified endings, for instance, fault classification in AC power systems. Fault classification methods based on the logic flow can be seen as a set of rules which considers statistic parameters or defined thresholds in the classification logic.

2.2.1 Artifical Neural Network

Liu et al. (2014) proposed a fault detection and classification method based on multiwavelet packet, Shannon entropy and radial bases function neural network. Four entropies were defined with the multiwavelet packet to extract features to be used on the radial basis function training identify e classify faults in transmission lines. The multiwavelet packet was compared with the wavelet packet and the Shannon entropy was compared with Tsallis entropy. The fault simulations were performed at power transmission line and the signals were measured at a local bus. A cycle of samples, half of it at pre-fault and half after the fault, were required to training the neural network. The methodology was evaluated under different fault distance, fault inception angle and fault resistance. The recognition rate were 100% for Tsallis entropy regardless the use of multiwavelet packet or wavelet packet.

Zin et al. (2015) used Clarke transform to decouple the three phase currents from the system which were used by DWT to extract the high frequency components. The mother wavelet db4 and the first until the fourth decomposition level were used to process the fault detection on parallel transmission lines. The sum of high frequency wavelet components were used as

inputs to the back propagation neutral network (BPNN). The methodology were evaluated under different fault types, fault distance, fault resistance and fault inception angles. The errors involved in the classification processes were compared between the use of the preprocessing with and without Clarke transform. The Clarke transform usage provide better results. Besides, the BPNN performance was compared with pattern recognition network and fit network which proved to be the best choice to the designated problem.

A robust artificial neural network methodology was published by Raval and Pandya (2020) to classify eleven different fault types in a power system with series compensated lines. The currents from one end of the transmission line are decomposed through the multiresolution analyses from wavelet transform. The 4th and 5th wavelet decomposition levels are used as fault detection and the 8th wavelet decomposition level is used as inputs to several ANN topology. A combination of techniques led to the development of the particle swarm optimization based on neural network with feature selection. This technique was compared with back-propagation, genetic algorithm and the particle Swarm. The number of hidden neurons, the features number and the features size were varied for the training and testes procedures. Besides that, the fault types, fault distance, fault resistance and source impedance were varied to composed the database for the evaluations. The method best performance achieved 99.7% of accuracy. Unfortunately, the results were not performed in real time to be able to inform the time request to the classifier provide a reliable diagnoses. In addition, the method is based on wavelet transform which has issues in fault with damped transients and the use of several decomposition levels would imply delays in the method response.

Even though ANN-based techniques usually provide a high recognition rate, these techniques require a diversified and large amount of data to perform a robust training which can be difficult to acquire from the power system in most applications.

2.2.2 Support Vector Machine

Support vector machine (SVM) is an automatic learning system based on the optimal separation of hiperplanes. Therefore, Malathi, Marimuthu and Baskar (2010) proposed intelligent approaches using SVM and extremely learning machine (ELM) for transmission lines. The inputs to both machines were the wavelet coefficients provided by the DWT from the fist decomposition level. A half cycle of currents after the fault were needed to train the machines. The mother wavelet Doubechies with 4 coefficients was used to extract the features to identify, classify and locate the fault. The 9600 faults were performed varying the fault resistance, fault inception angle, fault distance, the pre-fault power level and the source impedance. The fault classification computed by SVM achieved 99.11% and by ELM was 91.89%. The time requested to provide the fault classification was not mentioned through the paper.

Unlike most methods presented in the literature, Parikh, Das and Maheshwari (2010) did not require any preprocessing to the three phase currents and the ground current signals to classify the faults in series compensated transmission lines. A SVM was dedicated to each of the 4 currents signals. The evaluations covered fault resistance, fault inception angles, fault distance, compensation line level and the source strength. The accuracy obtained to one cycle of samples (20 ms) as inputs to SVM was 98.703%. The methodology was also evaluated to half cycle of samples (10 ms) which achieved 98.186% of accuracy. The method was not evaluated in real-time to obtain the time required to correctly classify the faults.

Wani (2018) used the SVM and DWT to identify, classify and locate the faults. Currents were collected from the system and positive sequence was computed. The wavelet coefficients and its energy at the fist decomposition level is used as a fault identification. Therefore, the

wavelet coefficients at the 7th decomposition level was computed to classify the faults and the SVM was used to locate the fault. The results presented are limited and the conclusions scarce. The fault inception angle, which is a challenge to DWT, was not evaluated. The SVM is a robust technique to separate different classes which lead some researchers apply it to fault classification achieving a high accuracy rate. However, the selection of the kernel and parameters needed to correctly tune the SVM can be a challenge to this application.

2.2.3 Fuzzy Logic

Youssef (2004) presented a fault type classifier by using fuzzy-logic applied to transmission lines. The method acquired the tree line currents and two samples were used to minimize the DC offset components. The high frequency harmonic and nonharmonic components were removed by using ten sample data window wavelet-based approach with mother wavelet db8 at the fourth decomposition level. The zero, positive and negative sequence components were computed in time to be used as inputs to the fuzzy-logic. The fuzzy-set approach involves the stages of fuzzification, inference, composition, and de-fuzzification. The rule matrix was set to classify single SLG faults, DL faults, DLG faults and identify the phases involved in the fault. Simulations were performed in a transmission line varying the type of shunt faults at different locations, inception angles, and pre-fault conditions of the system (source impedance). The results were satisfactory after 10 ms. The fuzzy classifier was unable to classify three-phase faults and took 2/3 cycles to identify the faulted phases.

Malik and Sharma (2017) proposed a new approach for fault classification based on modified fuzzy Q learning (MFQL). This artificial intelligence was modified in order to minimize the drawbacks existent in the original version. The new technique could classify eleven conditions, ten fault types and one health condition. The feature extracted technique called EMD, which is similar to Fourier transform, was used to decompose currents and voltages in components called intrinsic mode functions (IMF). The J48 algorithm, which is a decision tree algorithm, identifies eight most relevant IMF provided by the EMD method. After that, the final classification is determined by MFQL. The method was evaluated by using a 500 kV power system with a 300 km transmission line and accomplished the accuracy of 99.97% by using 10000 samples and of 92% by using 200 samples. Besides, this method was compared with ANN and SVM techniques, the comparison proved to be better the accuracy of the MFQL methodology. Although the technique was evaluated to several cases and provided a good accuracy rate, fuzzy logic is dependent on huge samples and training for knowledge representation, leading to an excessively complicated processing.

2.2.4 Decision Tree

Recently, a new approach using wavelet transform was proposed by Abdelgayed, Morsi and Sidhu (2018) in order to classify eleven fault types. The proposition used harmonic search algorithm (HSA) to determine the most suitable wavelet function and the optimal number of wavelet decomposition level. A difference between two cycles is computed followed by the computation of coefficients and energies at four decomposition levels to both quantities. By using the energies at the 4th levels, a matrix containing 30 elements is created and applied to all 11 fault types. A reference vector during the steady-state is computed and a normalization of the matrix elements are required once wavelet and scaling coefficients are used. The Euclidean distance is applied to identify the similarity between the reference vector and the normalized information from each fault type. The variance is maximized when the suitable wavelet function

and the decomposition level is achieved. A K-Nearest Neighbour and a decision tree are two machines learning used to, in fact, classify the fault types. A cross validation is employed to evaluate the performance of the classifier by estimating the prediction error for unseen cases. The method was evaluated in a power system to all 11 fault types varying the fault resistance and location. All the four decomposition levels were needed and the ideal wavelet function was a combination between the biorthogonal bior1.5 and db4. The accuracy was 100% for evaluated cases and the time required was not mentioned through the article. The fault types were just ten once the three-phase fault and the three-phase-to-ground fault ended being classify as the same type, symmetrical fault. Although the results presented an accuracy of 100%, the fault inception angle was not evaluated which is one of the greatest challenges when the methodology uses high frequency information.

A fault classification scheme for series capacitor compensated transmission line was published in Mishra, Yadav and Pazoki (2018). The method uses a combination of the fast discrete orthogonal S-transform, which is a less redundant compared to Stockwell's transform, and the singular value decomposition (SVD) in order to extract feature to detect the faults. The bagged tree ensemble, which is a simple method employed to machine learning with high variance in order to reduce it, is used for the presented fault classification. The method was extensively evaluated under different fault resistance, fault distance, fault inception angle, close-in faults, source strength (reverse power flow), signal-noise ratio, CT saturation, serie-compensated level. The results prove to be accurate to detect and classify the faults in less than 10 ms. The bagged tree is compared to other methodology which presented better results, this method only required half cycle wheres the other methodologies take one cycle to correctly classify the faults.

2.2.5 Logic Flow

One of the first methods presented in literature about fault classification by using the DWT was published in 1998 by Liang, Elangovan and Devotta (1998). The method classifies all fault types by using only the wavelet coefficients provided by the convolution between the sampling signal and the Daubechies filter with 4 coefficients (db4) at the first level of the decomposition. The algorithm computed the current wavelet coefficients by using a sampling frequency of 600 Hz. Three sharps at the wavelet coefficients signals were required to start the classification conditions by comparing the four signals in different ways to identify each fault type. In addition to this comparison, some thresholds were defined by analyzing fault simulations in a specific transmission system. Although the presented results evidence that the method was able to detect all the fault types regardless the fault distance, fault inception angle or fault resistance, the results presented are quite limited which could not be so conclusive. By using just the wavelet coefficients the threshold are quite difficult to be defined according to distance, resistance, and fault inception angle since theses parameters affect directly the coefficients magnitudes. Besides, thresholds fixed according to the system fault condition probably will change with load variation or in a different systems. The time required to the classification be achieved or its accuracy was not mentioned through the article.

Youssef (2003) proposed a wavelet classifier which uses three-level decomposition and reconstruction process to extract the high frequency components. The high coefficients are computed to zero sequence current and to other six signals provided from the sum and difference of each two phase currents. The condition to define all the ten fault types are based in a defined error. The method performance was evaluated under some fault inception angles, fault distances, and fault resistances. The evaluations took place in a system composed by a 300 km, 400 kV transposed double-end fed transmission line with 70% series compensation. Some analyses

were made about the data window and the sampling frequency which led them to conclude that the methodology could work properly using 20 or 8 samples at 2 kHz, 4 kHz or 8 kHz with the mother wavelet being Doubechies with 4 or 8 coefficients or Symlets with 4 or 8 coefficients. The time need to correctly classify the faults was not mentioned. Although the method was tested for some fault inception angles, some critical angles were neglected. The fault resistance and distance also were not widely evaluated and the combinations of all critical situations was not mentioned.

A fault classification and faulted-phase selection based on travelling wave concepts was developed by Dong, Kong and Cui (2009). The system signals are treated by Karenbauer transformation which provide important information to be extracted by the cubic B-Spline dyadic wavelet. The second, third and fourth wavelet scales are used to compute the modulus maxima to identify the fist travelling wave. An amount of rules are described to identify correctly the fault type and the faulted-phases. The presented simulated results describe good performance of the method. However, the method cannot provide good results to faults with inception angles under 6° and some three-phase faults are incorrectly classified as DLG fault. In addition, the results presented in the paper are limited because they just provide case studies.

He et al. (2010) developed a fault detection and classification in EHV transmission lines by using DWT in association with singular decomposition valuer (SDV) and Shannon entropy, been called as wavelet singular entropy (WSE). The DWT used db4 mother wavelet in the fourth decomposition level to compose a matrix. A SDV is applied to matrix A and a new large matrix is computed. In order to turn this stage faster and more effective some conditions were defined to neglect the tiny singular values. The entropy of the singular-value array was found computing the probability from the new matrix elements. Finally, the WSE is obtained which is used to map the correlative wavelet space into independent linearity space and to indicate the uncertain of the energy distribution in time-frequency domain with high immunity to noise. The performance of the method was evaluated using a window with 100 samples shifted by a step of 100 samples and the fault classifier took 200 samples after the fault detection. Different fault types, fault inception angles, fault distance, fault resistance and noise added to the system were evaluated and the results showed that the method is accurate. Although other methods were compared with the previous described method and which present a better accuracy, the time required to fault classification was not clear or compared through the paper. The classifier required half cycle after the fault had been detected which means that the minimum assumption is 10 ms, but it is not clear how much time was need to detected the fault, once the four decomposition level is used and a 100 sampling window is required to the detection.

The SWT was used to extract high-frequency components from local currents by means of the wavelet coefficient energy, and a normalization was performed to design the fault classification logic flow. After the fault identification the method address a fault type for each sample during half cycle, then the most frequent fault type during the half cycle is declared as being the correctly fault type. This method was performed in real time and achieved a good accuracy. However, the fault-induced transients are heavily damped in specific fault inception angles (COSTA; SOUZA; BRITO, 2012a), and this may lead to inaccuracy of DWT- and SWT-based fault classification methods. Furthermore, the DWT/SWT is highly affected by the choice of the mother wavelet (COSTA, 2014b). Nevertheless, the real-time boundary SWT (RT-BSWT) could overcome these drawbacks because it is sensitive to both fault-induced transients and low frequency (COSTA, 2014a, 2014b).

A two terminal classifier based on wavelet multiresolution analysis (MRA) was used in the forth decomposition level in a proposition made by Rajaraman et al. (2016). The method uses current signals from both ends of the transmission line from a double fed system modeling in

Simulink with 300 km line length and a certain amount of sample rules were defined to identify the fault type and the phases evolved. The best mother wavelet was identified as been db4 between 16 different wavelet functions. Case studies were used to point the fault distance and fault inception angle influence to the classifier which achieved satisfactory results. However, it is not clear how these evaluations were done, for instance, it was not mentioned which angles were covered. The time required to classify the faults was not mentioned.

A methodology for time-frequency analysis through power spectral density (PSD) was released by Guillen et al. (2018) in order detect and classify faults. This approach obtain two PSDs: one in time and other in frequency. The PSD in frequency based on wavelet transform at the third decomposition level were used to preserve high-frequency components supporting the classification process. In order to analyze transient information, the line currents were scaled up to build one matrix to be analyzed by means of covariance matrix. A classification process is launched using the Hellinger distance, which quantify the degree of similitude between two variables. The threshold stage were substituted by some machine learning to prove the achievement of better results by the new methodology. The method was evaluated by using simulations from a radial system and by using real data from the New England power grid. The method worked well to all evaluations excepted to faults with fault resistance bigger than 100 Ω to DLG, which are misclassified, in some cases, to SLG.

2.3 Summary of Literature Review

Table 2.1 summarizes, in chronological order, the main publications related to fault directional protection methods. The employed technique, the targeted application, the sampling frequency and the validation type (simulation or/and experimental) are highlighted to each method. In addition, Table 2.2 summarizes publications related to fault classifier highlighting the employed technique, the number of fault types the methods are able to classify, the time required to the method classifies the faults, the accuracy of the methods, the quantities which are required to implement the method, the sampling frequency and, if exists, the used mother wavelet.

Regarding the directional protection, the wavelet transform has been widely applied to correctly identify the fault directionality by following different methodologies. However, the high-frequency information contained in the transients are the most common information used into the development of the reviewed methods. Therefore, those methods neglect the low-frequency information which can be used to create reliable protection such as the conventional methods to be working as main or redundancy units to the protection proposed based on high frequency information.

The fault classification reviewed presented some problem to identify all of the ten fault types fast and accurate. The fault inception angles are one of the most frequent challenges faced by those methods due to the damped transients. Even by using other technique associated with the wavelet transform the fault classification accuracy is low. In the cases where the accuracy achieved 100%, the average time requested to correctly classify the fault was near to 10 ms. Therefore, there are demand in the literature for a fast and reliable wavelet-based fault classifier.

Table 2.1: Summary of the literature review related to directional protection methods.

Reference	Employed technique	Application	Sampling Freq. (kHz)	Validation	
				Sim.	Exp.
Chen et al. (2003)	DWT	Transmission Lines	100.0	√	-
Eissa (2004)	-	Bus-Bar	0.8	√	-
Lahiri et al. (2005)	RNA	Transmission Lines	1.0	√	√
Eissa (2005)	PWT	Transformers	20.0	√	-
Valsan e Swarup (2007)	DWT	Bus-Bar	2.0	√	√
Aguilera et al. (2007)	DWT	Transmission Lines	80	√	-
Eissa e Mahfouz (2012)	CC	Transmission Lines	6.0	√	-
Ukil et al. (2012)	DFT	Transmission Lines	2.5	√	-
Biswal et al. (2013)	LS	Transmission Lines	1.0	√	-
Khan e Sidhu (2014)	-	Transformers	-	√	-
Jones e Kumm (2014)	DFT	Distribution System	-	√	√
Kong et al. (2015)	TE	Transmission Lines	10.0	√	-
Saleki et al. (2015)	*k*-NN	Transmission Lines	10.0	√	√
Luo et al. (2016)	DHT	HVDC Lines	10.0	√	-
Pintos et al. (2016)	TDFR	Microgrids	3.84	√	-
Costa et al. (2017)	MODWT	Distribution System	15.36	√	√
Samet et al. (2019)	Time-Domain	Transmission Lines	3.84	√	√

CC - correlogram coefficients; LS - least squares; TE - transients energy; *k*-NN - *k-Nearst Neigbhour*; MODWT - *maximal overleap discrete wavelet transform*; RDFT - recursive discrete Fourier transform.

Table 2.2: Summary of the literature review related to wavelet-based fault classifier methods.

Reference	Employed technique	Fault types	Time	Accuracy	Quantities number	Sampling Freq.(kHz)	Wavelet Level
Liang et. al.(1998)	DWT	10	-	-	4 (I)	10 kHz	1 (db4)
Youssef (2003)	DWT	10	-	-	7 (I)	1-8 kHz	3 (db4)
Youssef (2004)	DWT+Fuzzy	9	10 ms	-	6 (I)	4.5 kHz	4 (db8)
Dong et. al.(2009)	DWT+DT	10	-	<100%	4 (I)	400 kHz	4 (B)
He et al. (2010)	WSE	10	>10 ms	100%	7 (I,V)	20 kHz	4 (db4)
Parikh et. al(2010)	SVM	10	10 ms	98.16%	3 (I)	4 kHz	-
Malathi et. al(2014)	DWT+SVM	10	8.2 ms	99.11%	3 (I)	1.6 kHz	4 (db4)
Liu et. al(2015)	MWP+ANN	10	-	100%	3 (I)	10 kHz	3 (db4)
Zin et. al(2015)	DWT+ANN	10	-	< 100%	3 (I)	200 kHz	4 (db4)
Rajaraman et al. (2016)	MRA	10	-	100%	6 (I,I)	3 kHz	1 (db4)
Malik et. al(2017)	DWT+Fuzzy	10	-	99.32%	3 (I)	3 kHz	-
Mishara et. al(2017)	ST+DT	10	8.3 ms	100%	3 (I)	-	-
Abdelgayed et. al.(2018)	DWT + DT	10	-	100%	6 (I,V)	3.84 kHz	4 (db4)
Guillen et. al.(2018)	DWT + PSD	10	-	< 100%	3 (I)	3.84 kHz	3 (db4)
Raval and Pandya (2020)	MRA + ANN	11	-	99.7%	3 (I)	20 kHz	8 (db4)

DT - decision tree; MM - modulus maxima; ST - S-transform; ANN - artificial neural network; MWP - multiwavelet packet.

Chapter 3

Mathematical Tools

This chapter presents the reasoning of the mathematical tools used for the development of this work: Fourier transform to support the phasor estimation description; symmetrical components in the frequency domain to recreate the classical directional units; the symmetrical components in time domain to support the development of the proposed directional protection; Clarke transformation to support the developed of the proposed fault classifier, the discrete wavelet transform and some of its variants to support all the proposed method.

3.1 Discrete Fourier Transform - DFT

Joseph Fourier proposed that any periodic signal in time could be represented for a series of sine and cosine weighted sums in 1807. However, this work did not present the high mathematical stringency which caused its publication just 15 years late when the book title *Analytical Theory of Heat* was released (FOURIER, 1878).

Since then, the Fourier transform has become a useful tool to revel a time signal composition in frequency. Particularly in protection applications, the phasor estimation is usually computed by full cycle Fourier algorithm and its variants. Therefore, based in Phadke and Thorp (2008), the phasor estimation can be computed in real-time as follows:

$$\mathbf{X} = \frac{2}{\Delta k} \sum_{n=k-\Delta k+1}^{k} x(k) \left\{ \cos\left(\frac{2\pi n}{\Delta k}\right) + j\sin\left(\frac{2\pi n}{\Delta k}\right) \right\}, \tag{3.1}$$

where $\mathbf{X}$ is the phasor estimation; $\Delta k = f_s/f$ is the number of samples into a power cycle; f_s is the sampling frequency; f is the fundamental frequency; $x(k)$ is the original signal sample associated in time to the sampling index k. The phasor is a complex number which can be written in terms of module ($|\mathbf{X}(k)|$) and angle ($\angle\mathbf{X}(k)$) as follows (PHADKE; THORP, 2009):

$$|\mathbf{X}(k)| = \sqrt{X_r(k)^2 + X_i(k)^2} \tag{3.2}$$

and

$$\angle\mathbf{X}(k) = \tan^{-1}\left(\frac{X_i(k)}{X_r(k)}\right), \tag{3.3}$$

where X_r e X_i are, respectively, the real and imaginary part of phasor $\mathbf{X}$.

The traditional manner to compute the DFT of a signal with Δk samples per cycle is doing a product of two matrices with size Δk x Δk. Even though, traditionally the DWT does not requires several samples to estimate the fundamental frequency, those matrices present the kth sample being $e^{-j2\pi/\Delta k}$ which leads to a costly processing as the number of samples grows.

Therefore, in order to minimize the computational burden, a recursive version of this algorithm is used in this work (PHADKE; THORP, 2008):

$$\mathbf{X}(k) = \mathbf{X}(k-1) + (x(k) - x(k-\Delta k)) \left\{ \cos\left(\frac{2\pi k}{\Delta k}\right) + j\sin\left(\frac{2\pi k}{\Delta k}\right) \right\}. \tag{3.4}$$

The phasor computed at sampling k ($\mathbf{X}(k)$) is based in the calculation made to the last phasor ($\mathbf{X}(k-1)$) neglecting the contribution of the older sample ($x(k-\Delta k)$) and adding the newest sample, received in the time k/f_s ($x(k)$), where f_s is the sampling frequency. Therefore, the number of operations computed at each sampling is minimized and the phasor is estimated more computational efficiently.

In general, traditional protection requires phasor estimation information to process its protection logic. However, the phasors based on DFT do not reveal how the components represented in frequency vary with the time, which lead the DFT be better applied only to stationary signals (GAO; YAN, 2010).

3.2 Symmetrical Components

Symmetrical components, also known as sequence components, are classical mathematical techniques to analyze unbalanced three-phase electrical power systems. Fortescue (1918), who is responsible for the development of this efficient tool, proposed to decompose an unbalanced three-phase sinusoidal system into three different balanced system naming as positive sequence, negative sequence, and zero sequence.

In order to minimize the complexity of the power system analyses, in some applications, the use of symmetrical components is needed. These components can be computed before or after the phasor estimation. Since both procedures are linear, the result is the same (KASZTENNY et al., 2000). In this work, the sequence components computed before and after the phasor estimation will be called as symmetrical components in time domain and frequency domain, respectively.

3.2.1 Symmetrical Components in the Frequency Domain

As being computed after the phasor estimation, the symmetrical components in the frequency domain is computed by using both module and angle information. For instance, by using phasors of current signals from three phases ($\mathbf{I}_A$, $\mathbf{I}_B$, $\mathbf{I}_C$), the positive ($\mathbf{I}_{1A}$, $\mathbf{I}_{1B}$, $\mathbf{I}_{1C}$), negative ($\mathbf{I}_{2A}$, $\mathbf{I}_{2B}$, $\mathbf{I}_{2C}$) and zero ($\mathbf{I}_0$) current sequence components can be computed (BLACKBURN, 1993).

The positive sequence represents a balanced system with phase-displacement of 120°. The vectors have the same amplitude and rotate in the same direction of the original circuit, considering a system with phase sequence ABC (positive). The behaviour of the phasors of positive sequence currents $\mathbf{I}_A$, $\mathbf{I}_B$ and $\mathbf{I}_C$ is illustrated in Figure 3.1(a).

In order to better represent the lack of 120°, the operator α is defined as follows:

$$\alpha = 1\angle 120^\circ = -0.5 + j0.886 \tag{3.5}$$

and

$$\alpha^2 = 1\angle 240^\circ = -0.5 - j0.886. \tag{3.6}$$

Therefore, the positive sequence to the phasors of current signals are defined as follows (BLACKBURN, 1993):

$$\mathbf{I}_{1A} = \frac{1}{3}(\mathbf{I}_A + \alpha\mathbf{I}_B + \alpha^2\mathbf{I}_C), \tag{3.7}$$

$$\mathbf{I}_{1B} = \alpha^2\mathbf{I}_{1A} = \frac{1}{3}(\alpha^2\mathbf{I}_A + \mathbf{I}_B + \alpha\mathbf{I}_C) \tag{3.8}$$

and

$$\mathbf{I}_{1C} = \alpha\mathbf{I}_{1A} = \frac{1}{3}(\alpha\mathbf{I}_A + \alpha^2\mathbf{I}_B + \mathbf{I}_C). \tag{3.9}$$

One sequence phase is enough to define the other. Therefore, whether one exist the other will exist.

The negative sequence components are three-phase balanced with the same magnitude and 120° between phases with the rotation direction opposite to the original circuit. Figure 3.1(b) represents the negative sequence components $\mathbf{I}_{2A}$,$\mathbf{I}_{2B}$ and $\mathbf{I}_{2A}$ to a current signal. The negative sequence components in the frequency domain to current phasors are computed as follow (BLACKBURN, 1993):

$$\mathbf{I}_{2A} = \frac{1}{3}(\mathbf{I}_A + \alpha^2\mathbf{I}_B + \alpha\mathbf{I}_C), \tag{3.10}$$

$$\mathbf{I}_{2B} = \alpha\mathbf{I}_{2A} = \frac{1}{3}(\alpha\mathbf{I}_A + \mathbf{I}_B + \alpha^2\mathbf{I}_C) \tag{3.11}$$

and

$$\mathbf{I}_{2C} = \alpha^2\mathbf{I}_{2A} = \frac{1}{3}(\alpha^2\mathbf{I}_A + \alpha\mathbf{I}_B + \mathbf{I}_C). \tag{3.12}$$

The zero sequence components possess the same magnitude and the same angle to all three phases as depicted in Figure 3.1(c). Therefore, the zero sequence components ($\mathbf{I}_0$) can be computed as follow (BLACKBURN, 1993):

$$\mathbf{I}_0 = \frac{1}{3}(\mathbf{I}_A + \mathbf{I}_B + \mathbf{I}_C). \tag{3.13}$$

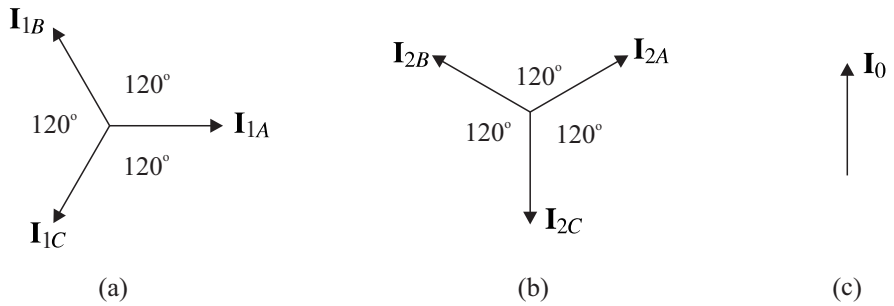

Figure 3.1: Current sequence components in frequency domain: (a) positive sequence; (b) negative sequence; (c) zero sequence.

All definitions made to current phasors may be extended to voltage phasors which lead to voltage positive sequence $\mathbf{V}_{1A}$, $\mathbf{V}_{1B}$, $\mathbf{V}_{1C}$, voltage negative sequence $\mathbf{V}_{2A}$, $\mathbf{V}_{2B}$, $\mathbf{V}_{2C}$ and voltage zero sequence $\mathbf{V}_0$ in the frequency domain.

In the traditional relays, the overcurrent and directional units use, into the protection logic, some specific symmetrical components since these components are more suitable to identify specific fault types, as presented in Table 3.1.

Table 3.1: Sequence components to each fault type.

Fault Type	Positive Seq.	Negative Seq.	Zero Seq.
Single Line-to-ground (SLG)	√	√	√
Double Line-to-ground (DLG)	√	√	√
Double Line (DL)	√	√	-
Three-phase (LLL)	√	-	-

3.2.2 Symmetrical Components in the Time Domain

The symmetrical components can be represented in the time domain by using time samples from a three-phase system (i_A, i_B and i_C). The positive, negative and zero sequences will be properly computed in an equivalent manner as by using phasors (DAS, 2016).

The positive sequence components in time domain follow the same logic from those computed in the frequency domain. However, the lag of 120° cannot be done in angle terms in time domain, these lag is done using a time complacent equivalent to 120°. As a cycle can be divided in three portions of 120°, the equivalent representation of α e α^2 in terms of time or samples is written as Δk_α and Δk_{α^2}, respectively, and defined as follow:

$$\Delta k_\alpha = \Delta k - \left[\frac{2\Delta k}{3}\right] \tag{3.14}$$

and

$$\Delta k_{\alpha^2} = \Delta k - \left[\frac{\Delta k}{3}\right], \tag{3.15}$$

where the operator [] is the nearest integer function, as the Δk should be a integer number, the Δk_α and Δk_{α^2} will complement each other. This arrangement guarantees the correctly angle which is quite relevant when the sampling frequency is low, because the difference of only one sample can lead to a totally different angle. Therefore, the positive sequence components in time domain are defined as follow:

$$i_{1A}(k) = \frac{1}{3}(i_A(k) + i_B(k - \Delta k_\alpha) + i_C(k - \Delta k_{\alpha^2})), \tag{3.16}$$

$$i_{1B}(k) = \frac{1}{3}(i_A(k - \Delta k_{\alpha^2}) + i_B(k) + i_C(k - \Delta k_\alpha)) \tag{3.17}$$

and

$$i_{1C}(k) = \frac{1}{3}(i_A(k - \Delta k_\alpha) + i_B(k - \Delta k_{\alpha^2}) + i_C(k)), \tag{3.18}$$

where i_{1A}, i_{1B} and i_{1C} are, respectively, the current positive sequence in time domain from phases A, B and C.

The negative sequence in time domain follow the same reasoning from frequency domain with the proper modifications, as follow:

$$i_{2A}(k) = \frac{1}{3}(i_A(k) + i_B(k - \Delta k_{\alpha^2}) + i_C(k - \Delta k_\alpha)), \tag{3.19}$$

$$i_{2B}(k) = \frac{1}{3}(i_A(k - \Delta k_\alpha) + i_B(k) + i_C(k - \Delta k_{\alpha^2})) \tag{3.20}$$

and

$$i_{2C}(k) = \frac{1}{3}(i_A(k-\Delta k_{\alpha^2}) + i_B(k-\Delta k_{\alpha}) + i_C(k)), \tag{3.21}$$

where i_{2A}, i_{2B} and i_{2C} are current negative sequence components in time domain from phases A, B e C, respectively.

The zero sequence components correspond the 1/3 from the sum of the three-phases at the sampling k, as follows:

$$i_0(k) = \frac{1}{3}(i_A(k) + i_B(k) + i_C(k)), \tag{3.22}$$

where i_0 is current zero sequence components to any reference phase.

All definitions here presented are also valid to voltage signals, which lead to obtain voltage positive sequence components (v_{1A}, v_{1B}, v_{1C}), voltage negative sequence components (v_{2A}, v_{2B}, v_{2C}) and voltage zero sequence component v_0 in time domain.

3.3 Clarke Transformation

The Clarke transformation, also known as αβ transformation, uses three-phase currents i_A, i_B, and i_C to calculate currents in the two-phase orthogonal stator axis α and β as presented in Figure 3.2. A homopolar component $i_{0\alpha\beta}$ is also extracted by using Clarke transform (DAS, 2016).

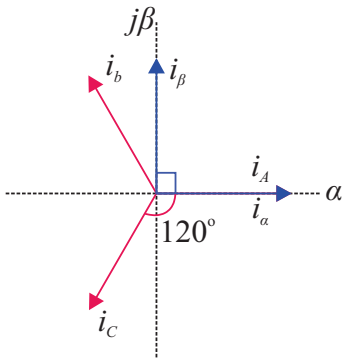

Figure 3.2: Current α and β components from Clarke transform.

There are several Clarke matrix representations, depending how the axes are defined and what requirements the representation aim to fulfill such as power or magnitude preservative or an orthonormal matrix (preserves neither). The importance in those representations is that the Matrix rows have to be orthogonal. In this work, the Clarke used matrix will be the power conservative representation, as follows (ROBBA, 1973):

$$\begin{bmatrix} i_{\alpha_A}(k) \\ i_{\beta_A}(k) \\ i_{0\alpha\beta}(k) \end{bmatrix} = \sqrt{\frac{2}{3}} \begin{bmatrix} 1 & -\frac{1}{2} & -\frac{1}{2} \\ 0 & \frac{\sqrt{3}}{2} & -\frac{\sqrt{3}}{2} \\ \frac{1}{\sqrt{2}} & \frac{1}{\sqrt{2}} & \frac{1}{\sqrt{2}} \end{bmatrix} \begin{bmatrix} i_A(k) \\ i_B(k) \\ i_C(k) \end{bmatrix}, \tag{3.23}$$

where i_{α_A}, i_{β_A} and $i_{0\alpha\beta}$ are α, β and zero Clarke components or modes to a three-phase system with positive sequence ABC with phase A as the reference. By changing the matrix reference to phase B and to phase C, (3.23) is extended as follows (ROBBA, 1973):

$$\begin{bmatrix} i_{\alpha_B}(k) \\ i_{\beta_B}(k) \\ i_{0\alpha\beta}(k) \end{bmatrix} = \sqrt{\frac{2}{3}} \begin{bmatrix} 1 & -\frac{1}{2} & -\frac{1}{2} \\ 0 & \frac{\sqrt{3}}{2} & -\frac{\sqrt{3}}{2} \\ \frac{1}{\sqrt{2}} & \frac{1}{\sqrt{2}} & \frac{1}{\sqrt{2}} \end{bmatrix} \begin{bmatrix} i_B(k) \\ i_C(k) \\ i_A(k) \end{bmatrix}, \tag{3.24}$$

$$\begin{bmatrix} i_{\alpha_C}(k) \\ i_{\beta_C}(k) \\ i_{0\alpha\beta}(k) \end{bmatrix} = \sqrt{\frac{2}{3}} \begin{bmatrix} 1 & -\frac{1}{2} & -\frac{1}{2} \\ 0 & \frac{\sqrt{3}}{2} & -\frac{\sqrt{3}}{2} \\ \frac{1}{\sqrt{2}} & \frac{1}{\sqrt{2}} & \frac{1}{\sqrt{2}} \end{bmatrix} \begin{bmatrix} i_C(k) \\ i_A(k) \\ i_B(k) \end{bmatrix}, \tag{3.25}$$

where i_{α_B} and i_{β_B} are the α-mode and β-mode from the matrix with the reference being phase B; i_{α_C} and i_{β_C} are the $\alpha\beta$ components with phase C as the reference; $i_{0\alpha\beta}$ did not appear with any subscript because the homopolar component is equal regardless the matrix phase reference. The $i_{0\alpha\beta}$ is equal to i_0 from symmetrical components in a balanced system during the stead-state. The Clarke components can be summarized as follows:

$$\begin{bmatrix} i_{\alpha_A}(k) \\ i_{\alpha_B}(k) \\ i_{\alpha_C}(k) \\ i_{\beta_A}(k) \\ i_{\beta_B}(k) \\ i_{\beta_C}(k) \\ i_{0\alpha\beta}(k) \end{bmatrix} = \sqrt{\frac{2}{3}} \begin{bmatrix} 1 & -\frac{1}{2} & -\frac{1}{2} \\ -\frac{1}{2} & 1 & -\frac{1}{2} \\ -\frac{1}{2} & -\frac{1}{2} & 1 \\ 0 & \frac{\sqrt{3}}{2} & -\frac{\sqrt{3}}{2} \\ -\frac{\sqrt{3}}{2} & 0 & \frac{\sqrt{3}}{2} \\ \frac{\sqrt{3}}{2} & -\frac{\sqrt{3}}{2} & 0 \\ \frac{1}{\sqrt{2}} & \frac{1}{\sqrt{2}} & \frac{1}{\sqrt{2}} \end{bmatrix} \begin{bmatrix} i_A(k) \\ i_B(k) \\ i_C(k) \end{bmatrix}. \tag{3.26}$$

3.3.1 Fault Characterization under Clarke Transformation

Single Line-to-Ground Fault

The fault boundary conditions to AG fault are $i_B = i_C = 0$, to BG fault are $i_A = i_C = 0$ and to CG are $i_B = i_C = 0$. By using Eq. (3.26), SLG fault are characterized in terms of Clarke's transform as follows in Table 3.2. Therefore, SLG faults present zero component and the phase involved in the fault present the highest amplitude value, while the phases not involved into the fault present equally a smaller amplitude.

Table 3.2: SLG faults under Clarke Transfom.

	i_{α_A}	i_{α_B}	i_{α_C}	$i_{0\alpha\beta}$
AG	$\sqrt{\frac{2}{3}}i_A$	$-\sqrt{\frac{1}{6}}i_A$	$-\sqrt{\frac{1}{6}}i_A$	$\sqrt{\frac{1}{3}}i_A$
BG	$-\sqrt{\frac{1}{6}}i_B$	$\sqrt{\frac{2}{3}}i_B$	$-\sqrt{\frac{1}{6}}i_B$	$\sqrt{\frac{1}{3}}i_B$
CG	$-\sqrt{\frac{1}{6}}i_C$	$-\sqrt{\frac{1}{6}}i_C$	$\sqrt{\frac{2}{3}}i_C$	$\sqrt{\frac{1}{3}}i_C$

Double Line Fault

The fault current boundary conditions to AB fault is $i_A = -i_B$, to BC fault is $i_B = -i_C$ and to CA is $i_C = -i_A$. By using Eq. (3.26), DL faults are characterized in terms of Clarke transform as follows in Table 3.3. Therefore, DL faults can be differentiated from other faults by using zero

component and observing that the phase not involved in the fault assume the zero amplitude value and the phases involved in the fault achieve a proportion of 50% of the fault current.

Table 3.3: DL faults under Clarke Transfom.

	i_{α_A}	i_{α_B}	i_{α_C}	$i_{0\alpha\beta}$
AB	$\sqrt{\frac{3}{2}}i_A$	$-\sqrt{\frac{3}{2}}i_A$	0	0
BC	0	$\sqrt{\frac{3}{2}}i_B$	$-\sqrt{\frac{3}{2}}i_B$	0
CA	$-\sqrt{\frac{3}{2}}i_C$	0	$\sqrt{\frac{3}{2}}i_C$	0

Double Line-to-Ground Fault

The fault current boundary conditions to ABG fault is $i_C = 0$, to BCG fault is $i_A = 0$ and to CAG is $i_B = 0$. DLG fault are characterized in terms of Clarke transform as follows in Table 3.4. These fault cases are reduced to a composition of two phases and the presence of zero component.

Table 3.4: LLG faults under Clarke Transfom.

	i_{α_A}	i_{α_B}	i_{α_C}	$i_{0\alpha\beta}$
ABG	$\frac{2i_A-i_B}{\sqrt{6}}$	$\frac{2i_B-i_A}{\sqrt{6}}$	$\frac{-i_A-i_B}{\sqrt{6}}$	$\frac{i_A+i_B}{\sqrt{3}}$
BCG	$\frac{-i_B-i_C}{\sqrt{6}}$	$\frac{2i_B-i_C}{\sqrt{6}}$	$\frac{2i_C-i_B}{\sqrt{6}}$	$\frac{i_B+i_C}{\sqrt{3}}$
CAG	$\frac{2i_A-i_C}{\sqrt{6}}$	$\frac{-i_C-i_A}{\sqrt{6}}$	$\frac{2i_C-i_A}{\sqrt{6}}$	$\frac{i_C+i_A}{\sqrt{3}}$

Three Phase Fault

The fault current boundary conditions to ABC fault are $i_A \neq 0$, $i_B \neq 0$ and $i_C \neq 0$. By using Eq. (3.26), LLL fault is characterized in terms of Clarke transform as follows in Table 3.5. Therefore, LLL faults do not present zero component and the alpha components values are different those present in LL faults.

Table 3.5: LLL faults under Clarke Transfom.

	i_{α_A}	i_{α_B}	i_{α_C}	$i_{0\alpha\beta}$
ABC	$\frac{2i_A-i_B-i_C}{\sqrt{6}}$	$\frac{2i_B-i_C-i_A}{\sqrt{6}}$	$\frac{2i_C-i_A-i_B}{\sqrt{6}}$	0

3.4 Discrete Wavelet Transform - DWT

The first mention of the wavelet transformation were provided by Haar (1910) where the simplest mother wavelet developed until today was proposed. Several applications were added to the literature applying this techniques through the years. The highest contribution at the time

was made by Jean Morlet who implemented a windowing function and was the first to use the nomenclature wavelet in this area (MACKENZIE et al., 2001).

The work of Grossmann and Morlet (1984) had a huge impact because it assured that a signal could be transformed in wavelet form and return to original manner without losing information, defining the Continuous Wavelet Transform (CWT). However, this representation is very redundant which requires a high computational burden impracticable in some real-time applications. After some years, in order to overcome this drawback, the multiresolution analysis was proposed by Mallat (1989) and the Discrete Wavelet Transform (DWT) was introduced by Daubechies (1992).

The multiresolution analysis defines that digital filters can be used to decompose a discrete signal into scaling and wavelet coefficients, in distinct decomposition levels, being trusted and with low computational burden, as follow:

$$s_j(k) = s_{j-1} * \overline{h}_\phi(2k) = \sum_{n=-\infty}^{\infty} h_\phi(n-2k) s_{j-1}(n) \tag{3.27}$$

and

$$w_j(k) = s_{j-1} * \overline{h}_\psi(2k) = \sum_{n=-\infty}^{\infty} h_\psi(n-2k) s_{j-1}(n), \tag{3.28}$$

where $j \geq 1$; $*$ represents the convolution operation; s_j and w_j are, respectively, scaling and wavelet coefficients at the jth decomposition level; s_0 is the original signal in the time domain ($x = s = s_0$); h_ϕ e h_ψ are (Infinite Impulse Response (IIR)) digital filters, low-pass (scaling) filter and high-pass (wavelet) filter, respectively; $\overline{h}_\phi$ and $\overline{h}_\psi$ are inverse IIR filters low- and high-pass, respectively.

Based on (3.27) and (3.28), the scaling and wavelets coefficients can be computed by a circular convolution ($\circledast$) between the finite signal and the finite impulse response (FIR) filters, as follows:

$$s_j(k) = s_{j-1} \circledast \overline{h}_\varphi(2k) = \sum_{l=0}^{L-1} h_\varphi(l) \overset{\circ}{s}_{j-1}(2k+l) \tag{3.29}$$

and

$$w_j(k) = s_{j-1} \circledast \overline{h}_\psi(2k) = \sum_{l=0}^{L-1} h_\psi(l) \overset{\circ}{s}_{j-1}(2k+l), \tag{3.30}$$

where $j \geq 1$; $0 \leq k \leq \Delta k/2^j - 1$; $\Delta k \leq 2^{j-1}L$; L is the filter length and may be power of 2 and $\overset{\circ}{s}(n + p\Delta k/2^j) = s_j(n)$

The scaling s_j and wavelet w_j coefficients at the jth decomposition level is computed by doing the convolution between the filters and the scaling coefficients from a level decomposition immediately below (s_{j-1}), followed by a downsampling by two, as exemplified in Figure 3.3.

In Figure 3.3, x is the original signal in the time domain and $\downarrow 2$ represents the downsampling by two. The signal x is decomposed into scaling (s_1) and wavelet (w_1) coefficients at the first decomposition level by using low-pass filter (h_ψ) and high-pass (h_φ) filters, respectively, followed by a downsampling by two. Therefore, w_1 represents the high frequency present in the signal whereas s_1 represents the low frequency information at the first decomposition level. At the next decomposition ($j = 2$), the same procedure is followed. However, the scaling coefficients from the first decomposition level is used as the input signal to the second decomposition level. This procedure can be repeated to several decomposition levels, always using the scaling coefficients from the previous level to compute the next level.

During this process, the sample numbers are being reduced due to the downsampling in

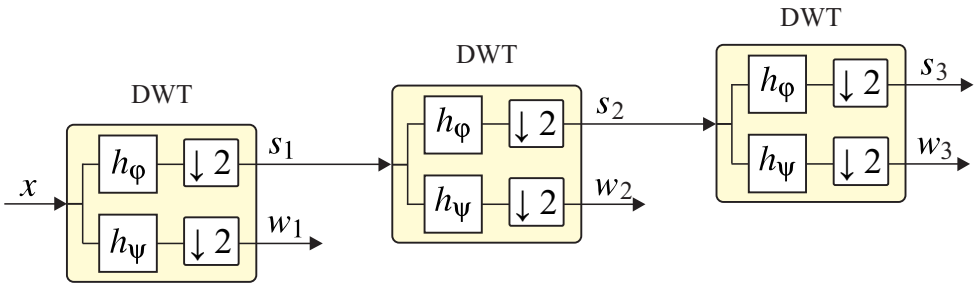

Figure 3.3: Block diagram to illustrate three decomposition levels of DWT.

each decomposition level. For instance, considering the original signal contain Δk samples, the first, second and third decomposition level will contain, respectively, $\Delta k/2$, $\Delta k/4$ and $\Delta k/8$. Regarding to the reconstruction of the original signal being composed by a spectral frequency band of [0 - f_s], the reconstruction process needs the wavelet coefficients information from first [$f_s/2$ - f_s], second [$f_s/4$ - $f_s/2$], third [$f_s/8$ - $f_s/4$] decomposition levels and the scaling coefficients in the third decomposition level [0 - $f_s/8$].

Scaling and Wavelet Filters

The digital filters used by the DWT decomposition process, the wavelet filter h_ψ and scaling filter h_φ, follow the propriety presented below:

$$h_\varphi(l) = (-1)^{l+1} h_\psi(L-l-1), \tag{3.31}$$

and

$$h_\psi(l) = (-1)^{l+1} h_\varphi(L-l-1), \tag{3.32}$$

where:

$$h_\varphi = \{h_\varphi(0),\, h_\varphi(1), ...,\, h_\varphi(L-2),\, h_\varphi(L-1)\} = \{-h_\psi(L-1),\, h_\psi(L-2),\, ...,\, -h_\psi(1),\, h_\psi(0)\}, \tag{3.33}$$

$$h_\psi = \{h_\psi(0),\, h_\psi(1),\, ...,\, h_\psi(L-2),\, h_\psi(L-1)\} = \{h_\varphi(L-1),\, h_\varphi(L-2),\, ...,\, h_\varphi(1),\, -h_\varphi(0)\} \tag{3.34}$$

Other proprieties that the filters follow are (PERCIVAL; WALDEN, 2000):

$$\sum_{l=0}^{L-1} [h_\psi(l)]^2 = 1 \Rightarrow \sum_{l=0}^{L-1} [h_\varphi(l)]^2 = 1, \tag{3.35}$$

$$\sum_{l=0}^{L-1} h_\psi(l) h_\psi(l+2n) = 0 \Rightarrow \sum_{l=0}^{L-1} h_\varphi(l) h_\varphi(l+2n) = 0 \tag{3.36}$$

and

$$\sum_{l=0}^{L-1} h_\psi(l) = 0 \Rightarrow \sum_{l=0}^{L-1} h_\varphi(l) = \sqrt{2}, \tag{3.37}$$

where $n \in \mathbb{Z}^*$ and $l = 0,\, 1,\, ...,\, L-1$.

3.4.1 Stationary Wavelet Transform - SWT

The SWT, also referred as maximal overlap discrete wavelet transform, is a variation of the DWT, in which the downsamples are suppressed, becoming invariant in time, providing a faster transient detection leading to be suitable for real-time applications (COSTA; SOUZA; BRITO, 2010). Although wavelet and scaling filters are also present in SWT, the downsampling by a factor of two does not occur, as exemplified in Figure 3.4. Therefore, the SWT becomes a non-orthogonal transform and can be applied to any number of samples since $N > L$, where N is the number of samples on the signal.

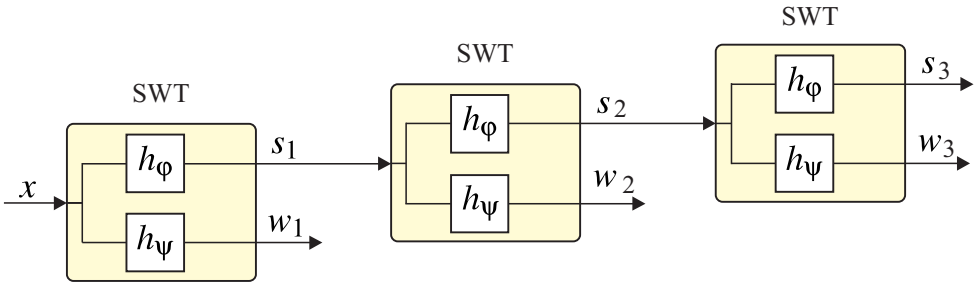

Figure 3.4: Block diagram presenting three decomposition levels of SWT.

Similar to the DWT, the SWT has its scaling and wavelet coefficients defined as follows:

$$s_j(k) = \frac{s_{j-1} * \overline{h}_\varphi(k)}{\sqrt{2}} = \frac{1}{\sqrt{2}} \sum_{n=-\infty}^{\infty} h_\varphi(n-k) s_{j-1}(n) \tag{3.38}$$

and

$$w_j(k) = \frac{s_{j-1} * \overline{h}_\psi(k)}{\sqrt{2}} = \frac{1}{\sqrt{2}} \sum_{n=-\infty}^{\infty} h_\psi(n-k) s_{j-1}(n), \tag{3.39}$$

where $j \geq 1$.

Rewriting the (3.29) and (3.30) to finite signals, the equations become:

$$s_j(k) = \frac{s_{j-1} \circledast \overline{h}_\varphi(k)}{\sqrt{2}} = \frac{1}{\sqrt{2}} \sum_{l=0}^{L-1} h_\varphi(l) \overset{\circ}{s}_{j-1}(k+l) \tag{3.40}$$

and

$$w_j(k) = \frac{s_{j-1} \circledast \overline{h}_\psi(k)}{\sqrt{2}} = \frac{1}{\sqrt{2}} \sum_{l=0}^{L-1} h_\psi(l) \overset{\circ}{s}_{j-1}(k+l), \tag{3.41}$$

where $j \geq 1; 0 \leq k \leq N; N \geq L$.

3.4.2 Real-Time Stationary Wavelet Transform - RT-SWT

In order to compute scaling and wavelet coefficients related to the conventional SWT based on the pyramid algorithm, all samples of the analyzed signal are required, which became an obstacle for real-time applications. In addition, by assuming the signal being periodic and circular, border distortions may occur (COSTA, 2014b). Therefore, RT-SWT decomposes a sampled signal x in the first level scaling s_x and wavelet w_x coefficients as follows (COSTA;

DRIESEN, 2013):

$$s_x(k) = \frac{1}{\sqrt{2}} \sum_{l=0}^{L-1} h_\phi(l) x(k+l-L+1) \tag{3.42}$$

and

$$w_x(k) = \frac{1}{\sqrt{2}} \sum_{l=0}^{L-1} h_\psi(l) x(k+l-L+1), \tag{3.43}$$

where only L samples are required to obtain s_x and w_x. Therefore, the RT-SWT can achieve similar result of SWT without requiring all samples of the signal as depicted in Figure 3.5, where a filter with 4 coeffcients from family Daubechies (db(4) mother wavelet) is employed to calculate the wavelet coefficients. At each sampling step ($1/f_s$ seconds) a new sample is incorporated into the window and the older sample is excluded, which allow the window shift. The wavelet coefficients of the main window (Figure 3.5(b)) computed through (3.43) are equal to those achieved using the SWT pyramid algorithm, with exception of the $L-1$ coefficients, which cannot be computed in real-time (COSTA, 2014b).

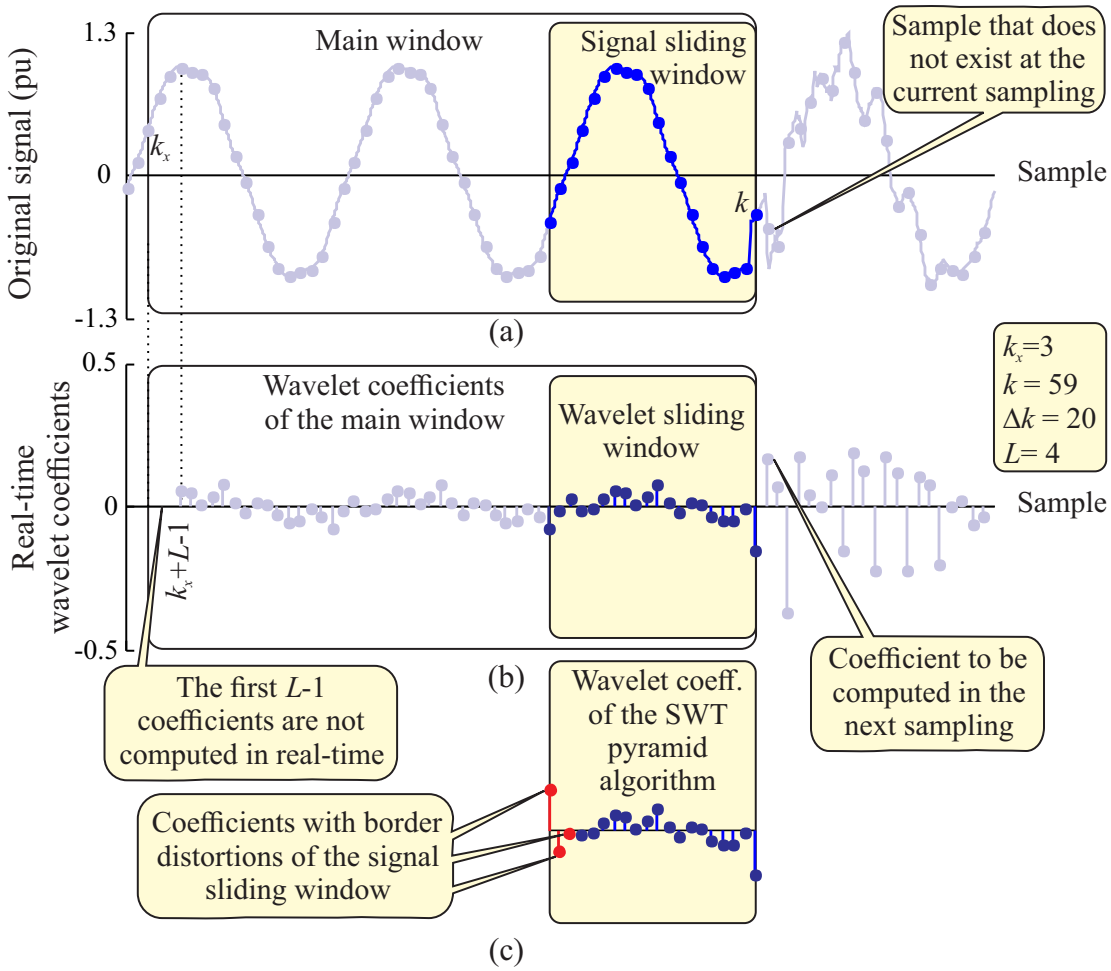

Figure 3.5: Recursive computation of the wavelet coefficients: (a) original signal; (b) recursive SWT wavelet coefficients; (c) wavelet coefficients of the SWT pyramid algorithm related to the signal sliding window. **Source**: Costa (2014b)

.

Scaling and Wavelet Coefficients Energy to RT-SWT

According to the Parseval theorem (BURRUS; RAMESH; GUO, 1998), the spectral energy of a signal x is equals the sum of the energy of the wavelet coefficients at the decomposition levels $1 \leq j \leq J$ with the energy of the scaling coefficients at the decomposition level j. Therefore, the energy of the wavelet and scaling coefficients for RT-SWT is defined by:

$$\sum_{k=0}^{\Delta k-1} |x(k)|^2 = \sum_{k=0}^{\Delta k-1} |s_J(k)|^2 + \sum_{j=0}^{J} \sum_{k=1}^{\Delta k-1} |w_j(k)|^2, \tag{3.44}$$

where the first equation sum is the energy of the original signal, the second sum refers to the energy of the scaling coefficients at the decomposition level j and the last sum is the energy of the wavelet coefficients at all decomposition levels.

For real-time implementation, it is necessary to use a window with Δk samples. Thus, the energy of the wavelet coefficients ($\mathscr{E}_x^w$) and the energy of the scaling coefficients ($\mathscr{E}_x^s$), at the current sampling k, for the first level of decomposition, are defined as follows (COSTA; DRIESEN, 2013):

$$\mathscr{E}_x^s(k) = \sum_{n=k-\Delta k+1}^{k} s_x^2(n) \tag{3.45}$$

and

$$\mathscr{E}_x^w(k) = \sum_{n=k-\Delta k+1}^{k} w_x^2(n), \tag{3.46}$$

where $k > \Delta k$. Recursively, these energies are calculated for each sample k as follows:

$$\mathscr{E}_x^s(k) = \mathscr{E}_x^s(k-1) - [s_x(k-\Delta k)]^2 + [s_x(k)]^2 \tag{3.47}$$

and

$$\mathscr{E}_x^w(k) = \mathscr{E}_x^w(k-1) - [w_x(k-\Delta k)]^2 + [w_x(k)]^2. \tag{3.48}$$

3.4.3 Real-Time Boundary Stationary Wavelet Transform - RT-BSWT

The border effects can cause a difference between the wavelet coefficients inside the wavelet sliding window and the coefficients of the signal sliding window, as depicted in Figures 3.5(b) and 3.5(c). Some methods were developed to deal with this problem (COHEN; DAUBECHIES; VIAL, 1993; COSTA, 2014a). In this work, in order to achive a fast fault detection, the border effects will be employed to provide additional information (COSTA, 2014a).

The sequence of $2L-1$ samples of the signal sliding window $x(k-L+1)$, ..., $x(k-1)$, $x(k)$, $x(k-\Delta k+1)$, ..., $x(k-\Delta k+L-1)$ is employed to compute each sample of the wavelet coefficients, which means that boundary coefficients are determined through some last and first samples of the signal sliding window. For instance, in Figure 3.6 the procedure to evaluate the db(4) wavelet coefficient with boundary effect is presented. The first sample affected by transients is placed among a group of steady-state operation samples and, due to this, SWT coefficients and those computed with border effects present significant changes in their magnitudes. Then, the usage of boundary coefficients instead of the conventional ones may present a highest magnitude when the transients affect a sample which lead to an easier disturbance detection Costa (2014a).

The first level of RT-BSWT scaling and wavelet coefficients associated to the current sampling k are computed through inner products between L coefficients of the wavelet h_ψ and

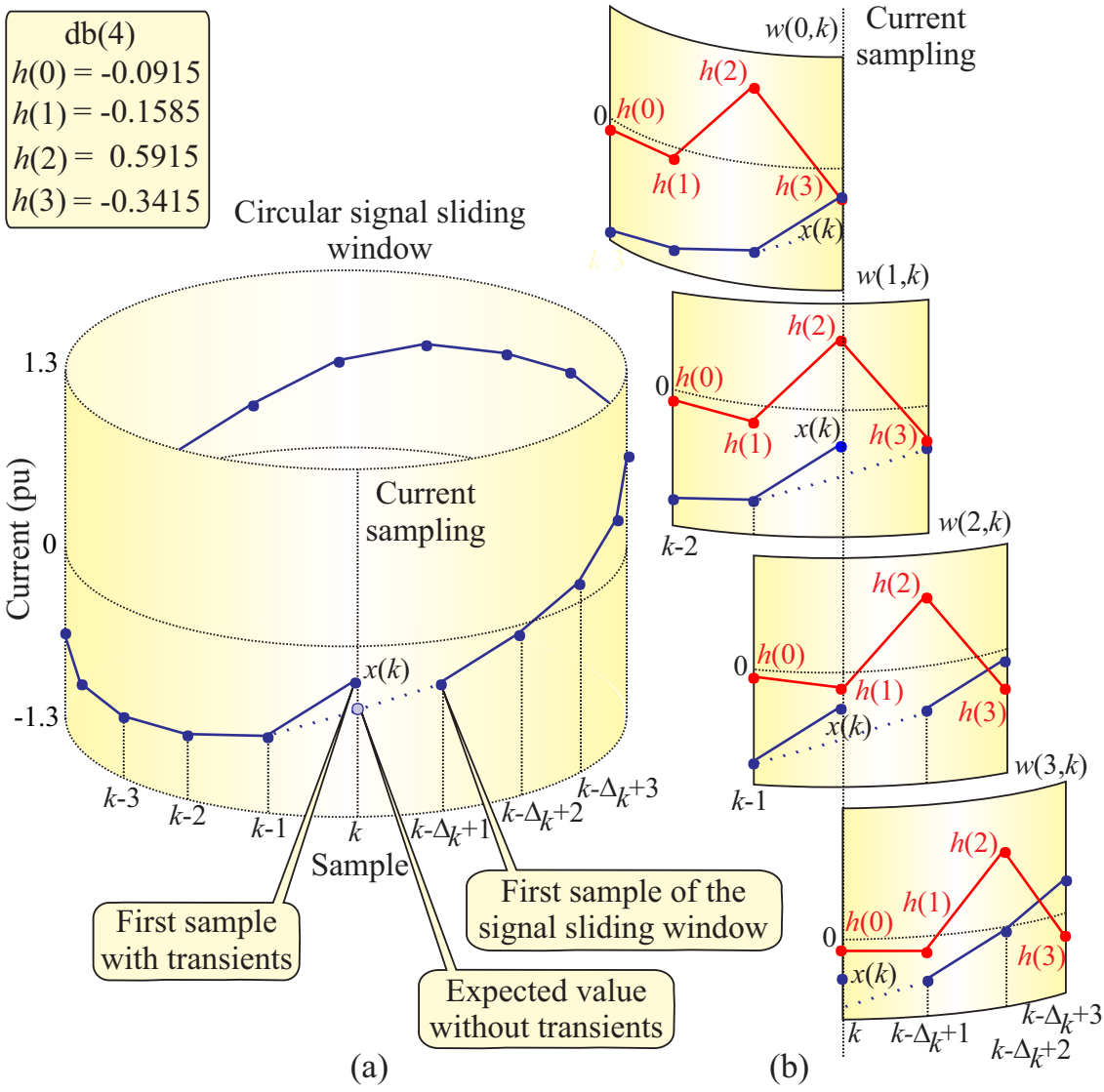

Figure 3.6: RT-SWT wavelet coefficients: (a) circular signal sliding window and (b) computation of boundary coefficients. **Source**: Costa (2014b).

scaling h_φ filters and L samples of the time-domain signal x inside a circular sliding window $\mathring{x}$ with Δk samples, as follows (COSTA, 2014a):

$$s_x(l,k) = \frac{1}{\sqrt{2}} \sum_{n=0}^{L-1} h_\varphi(n)\mathring{x}(k-L+n+1+l) \tag{3.49}$$

and

$$w_x(l,k) = \frac{1}{\sqrt{2}} \sum_{n=0}^{L-1} h_\psi(n)\mathring{x}(k-L+n+1+l), \tag{3.50}$$

where $0 \leqslant l < L$; $L \leqslant \Delta k$; $k \geqslant \Delta k - 1$; $\mathring{x}(k+m) = x(k+m)$ if $\Delta k < m \leqslant 0$ and $\mathring{x}(k+m) = x(k-\Delta k+m)$ if $0 < m \leqslant L$ (periodical signal in Δk samples).

According to (3.49) and (3.50), x is decomposed in L scaling and wavelet coefficients: 1) $w(0,k) = w(k)$ and $s(0,k) = s(k)$, which is equal to wavelet coefficient of the RT-SWT, and 2) $w(l,k)$ and $w(l,k)$ with $l \neq 0$, which are $L-1$ coefficients termed as boundary coefficients (coefficients with border distortions).

Scaling and Wavelet Coefficients Energy to RT-BSWT

As described before, the spectral energy of a signal x at the first decomposition level should be the sum the scaling and wavelet coefficients energy. However, as the boundary distortion occurs the total energy should consider the boundary coefficients contribution. Therefore, the scaling and wavelet coefficients energy from RT-BSWT is defined as follows:

$$\mathscr{E}_x^s(k) = \mathscr{E}_x^{sa}(k) + \mathscr{E}_x^{sb}(k) = \sum_{l=1}^{L-1} [s_x(l,k)]^2 + \sum_{n=k-\Delta k+L}^{k} [s_x(n)]^2 \tag{3.51}$$

and

$$\mathscr{E}_x^w(k) = \mathscr{E}_x^{wa}(k) + \mathscr{E}_x^{wb}(k) = \sum_{l=1}^{L-1} [w_x(l,k)]^2 + \sum_{n=k-\Delta k+L}^{k} [w_x(n)]^2, \tag{3.52}$$

where $k \leq \Delta k + 1$; $\mathscr{E}_x^{sa}$ and $\mathscr{E}_X^{wa}$ are, reactively, scaling ""and wavelet coefficients energy related to boundary distortion; $\mathscr{E}_x^{sb}$ and $\mathscr{E}_x^{wb}$ are scaling and wavelet coefficients energy excluding the boundary distortion, respectively. $\mathscr{E}_x^{w} \approx \mathscr{E}_x^{wb}$ in stead-state and during the $\Delta k - L + 1$ (Costa (2014a)).

3.5 Summary

In this chapter, an overview of the Fourier transform, Clarke transformation, symmetrical components in frequency and time domain were presented. In addition, the discrete wavelet transform and some of its variants, which provide better performance to fault detection in real-time, were detailed.

Chapter 4

Directional and Overcurrent Protection Principles

In this chapter the mathematical principles of classical directional and overcurrent protections will be presented showing details about the phase and sequence units (positive, negative and neutral) to both directional and overcurrent functions in order to provide the understanding of the further proposed method. In addition, the wavelet-based overcurrent protection proposed in literature will be detailed.

4.1 Signal Digital Pre-processing

Analog data from the electrical system can not be directly delivered to the protection system due to the high amplitudes, requiring a pre-processing. CT and voltage transformers (VT) or coupling capacitor voltage transformer (CCVT) are required for this purpose, reducing current and voltage levels to values as 1 or 5 A and 110 or 120 V (PHADKE; THORP, 2008), respectively. In addition, analog signals are not suitable to digital relays, requiring an analog-to-digital (A/D) converter.

In traditional relays, prior to the sampling process, filtering is performed using low pass filters to eliminate high frequency components, undesirable for the sampling process (JOHNS; SALMAN, 1997). This filtering needs to follow the criteria of the Nyquist-Shannon's theorem (ZAYED, 1993) to avoid poor representation in the sampling process, known as the aliasing effect. This issue is solved by ensuring that the sampling frequency is at least twice the desired highest frequency component on the signal.

Although the signals resulting from this pre-preprocessing are adequate data for traditional relays, most of the protection logics require magnitude and angle information, which require phasor estimation of current and voltage signals. Therefore, digital filters are required to obtain these phasors and the most commonly filters used to protection applications are based on Fourier algorithms.

4.2 Conventional Overcurrent Protection

Considered as one of the most frequent events in the power system, overcurrents can be caused due to overload or short-circuit (faults) situations. Overloads are characterized by more loads than expected connected to electric power system, causing moderate variations in the levels of current flowing in the system. On the other hand, short-circuits are caused by distinct

effects, but in general, they cause a more severe current variation compared to the overload (ANDERSON; ANDERSON, 1999).

The overcurrent protection evaluates, at each sample, the level of current present in the system by using the module of the estimated current phasor. When the measured current exceeds the permissible values, the shutdown of the protected area by the overcurrent unit is required. The current values permitted depend on system parameters such as short-circuit levels and load current, as well as the coordination and selectivity required for any the protection. The overcurrent levels in the system can activate the instantaneous or time-delay overcurrent function.

4.2.1 Conventional Instantaneous Overcurrent Units

The instantaneous overcurrent unit will be activated whether at least one of the system currents exceeds the instantaneous pickup current ($I_{un_{50}}$), as follows:

$$|I_{ph}| > I_{un_{50}} = Y_{un_{50}} I_{ph_r}, \tag{4.1}$$

where ph and un_{50} variable can assume $ph = \{A,\ B,\ C,\ 1A,\ 1B,\ 1C,\ 2A,\ 2B,\ 2C,\ 0\}$ and $un_{50} = \{50,\ 50_P,\ 50_Q,\ 50_N\}$, for instance, the instantaneous overcurrent unit of negative sequence will be activated whether the negative sequence current ($|I_2| = |I_{2A}| = |I_{2B}| = |I_{2C}|$) exceed the condition $|I_2| > I_{50_Q} = Y_{50_Q} I_{2_r}$; $Y_{un_{50}}$ is a constant related to the overcurrent protection sensibility according to the system requirements, i.e., it defines the pickup current of instantaneous overcurrent units; I_{ph_r} is the reference current, usually used as the load current. Therefore, $Y_{un_{50}}$ parameter usually is set higher than one to phase and positive sequence units and the remaining units allow it assume any value higher than zero. The reason of these rules are related with the load level to each unit. The choice of which values being used to each unit depends on the sensibility aimed to be achieve with the protection. In Table 4.1, the quantities associated to each instantaneous overcurrent unit are presented.

Table 4.1: Quantities to conventional instantaneous overcurrent units.

Instantaneous Overcurrent Units	Quantities		
	I_{ph}	$I_{un_{50}}$	$Y_{un_{50}}$
Phase A (50A)	I_A	I_{50}	Y_{50}
Phase B (50B)	I_B	I_{50}	Y_{50}
Phase C (50C)	I_C	I_{50}	Y_{50}
Positive Sequence (50P)	I_1	I_{50_P}	Y_{50_P}
Negative Sequence (50Q)	I_2	I_{50_Q}	Y_{50_Q}
Zero Sequence (50N)	I_0	I_{50_N}	Y_{50_N}

4.2.2 Conventional Time-delay Overcurrent Units

The time-delay overcurrent unit, unlike the instantaneous unit, has an intentional delay. This unit aims to ensure that low magnitude overcurrents, which can not sensitize the instantaneous threshold, will not be maintained for long periods causing damage to the system and to whom is connected to it. At the same time, the delay is useful to avoid unnecessary shutdowns due to temporary faults, which are characterized by its rapid disappearance from the system without any the interference of the energy company. In those cases, the time-delay unit identifies the overcurrent and starts the counting of the delay, when the fault disappears the protection will

not require the circuit breaker opening. Therefore, the dealership will not lose financial income due to temporary faults at the same time that assures the power system is safe to be used.

This delay is defined as being inversely proportional to the current magnitude, which means the larger the current is smaller is the time need to this unit operates. Figure 4.1 presents the IEEE standards to inverse time curves. The curves are classified as: moderately inverse (MI), very inverse (VI) and extremely inverse (EI). The suitable curve to the system depends on the relay parameters and the coordination requirements.

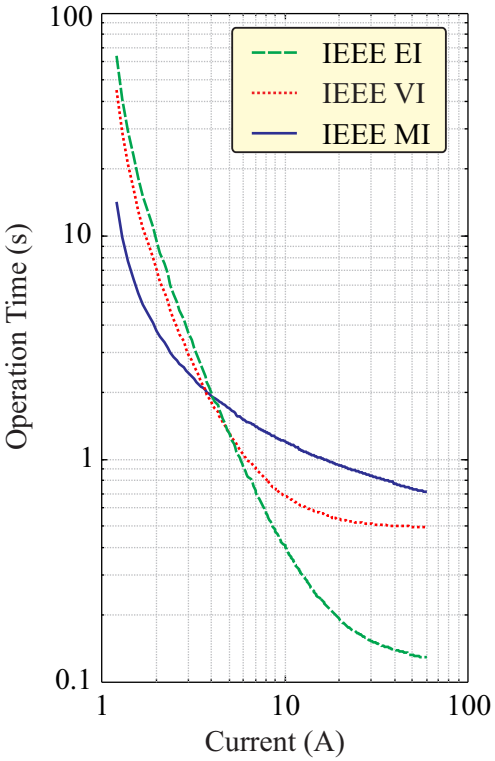

Figure 4.1: IEEE standard to overcurrent inverse-time relay curves. **Source**: (COSTA; MONTI; PAIVA, 2017)

.

The illustrated curves are provided from an exponential equation from the IEEE C37.112 standard (Institute of Electrical and Electronics Engineers, 1997), as follows:

$$T_P = \left(\frac{\delta}{\left(\frac{|I|}{I_r}\right)^{\rho} - 1} + \gamma \right) TMS, \tag{4.2}$$

where T_P is the time requested for protection activation, computed in seconds; TMS (time multiplier settings) is the variable that allows the shifting in time axis assuming values between 0 and 1; $|I|$ is the current module from the system; δ, γ e ρ are defined following Table 4.2.

Table 4.2: IEEE C37.112 curves and its parameters.

Curva	δ	γ	ρ
Moderately inverse (MI)	0.0515	0.1140	0.02
Very inverse (VI)	19.61	0.491	2.0
Extremely inverse (EI)	28.20	0.1217	2.0

The time-delay overcurrent function has an activation threshold (pickup current) lower than that required for the instantaneous unit, but this activation is only the start of the timer and it does not provide a trip. The trip will be guaranteed when the current instant t is equal or greater than the activation time plus the waiting time calculated by (4.2). Therefore, the time-delay overcurrent unit is activated when:

$$t \geq T_{51} + T_P, \tag{4.3}$$

where T_{51} is the instant when the time-delay overcurrent unit threshold is transposed.

Therefore, the time-delay units start the timer count when at least one of the system currents exceeds the time-delay pickup current, as follows:

$$|I_{ph}| > I_{un_{51}} = Y_{un_{51}} I_{ph_r}, \tag{4.4}$$

where un_{51} variable can assume $un_{51} = \{51,\ 51_P,\ 51_Q,\ 51_N\}$, for instance, the time-delay overcurrent unit of negative sequence will start the time counting whether the negative sequence current ($|I_2|$) exceeds the condition $|I_2| > I_{51_Q} = Y_{51_Q} I_{2_r}$; $Y_{un_{51}}$ is a constant related to the overcurrent protection sensibility according to the system requirements; Therefore, the parameter $Y_{un_{51}}$ usually is set higher than one to phase and positive sequence units and the remaining units allow it assume any value higher than zero. Table 4.1 presents the quantities associated to time-delay overcurrent unit.

Table 4.3: Quantities to conventional time-delay overcurrent units.

Time-delay	Quantities		
Overcurrent Units	I_{ph}	$I_{un_{51}}$	$Y_{un_{51}}$
Phase A (51A)	I_A	I_{51}	Y_{51}
Phase B (51B)	I_B	I_{51}	Y_{51}
Phase C (51C)	I_C	I_{51}	Y_{51}
Positive Sequence (51P)	I_1	I_{51_P}	Y_{51_P}
Negative Sequence (51Q)	I_2	I_{51_Q}	Y_{51_Q}
Zero Sequence (51N)	I_0	I_{51_N}	Y_{51_N}

As presented in Tables 4.1 and 4.3, the current phasors from the phase and sequence units are used to be compared with their respective thresholds as summarized in Figure 4.2. All thresholds are usually computed in steady-state and the time-delay units present an intentional delay inversely proportional to the system current magnitude. The units work in parallel, which means if any unit is activated, the trip is sent requiring the circuit break opening.

4.3 Conventional Directional Overcurrent Protection

Directional protection is generally found in association with other protections, such as overcurrent, distance, and differential protection aiming to aid the disturbance diagnosis in transmission lines, busbars, transformers, and generators. By adding the directional function, the

protection becomes able to provide information about the fault direction, with the measurement point as the reference. The directionality information simplifies the coordination between the relays, since the relay parametrization does not need to consider the change of the short circuit current direction, working in only one direction.

The classical directional protection uses information from the full cycle Fourier algorithm and implements the torques calculation based on the operation and polarization quantities, to provide the direction of the short circuit current that propagates at the measurement point. This method assumes that the angle formed between voltage and current (impedance angle) behaves differently for each situation. Four directional modules are traditionaly proposed: phase, positive sequence, negative sequence, and zero sequence units (ROBERTS; GUZMAN, 1994).

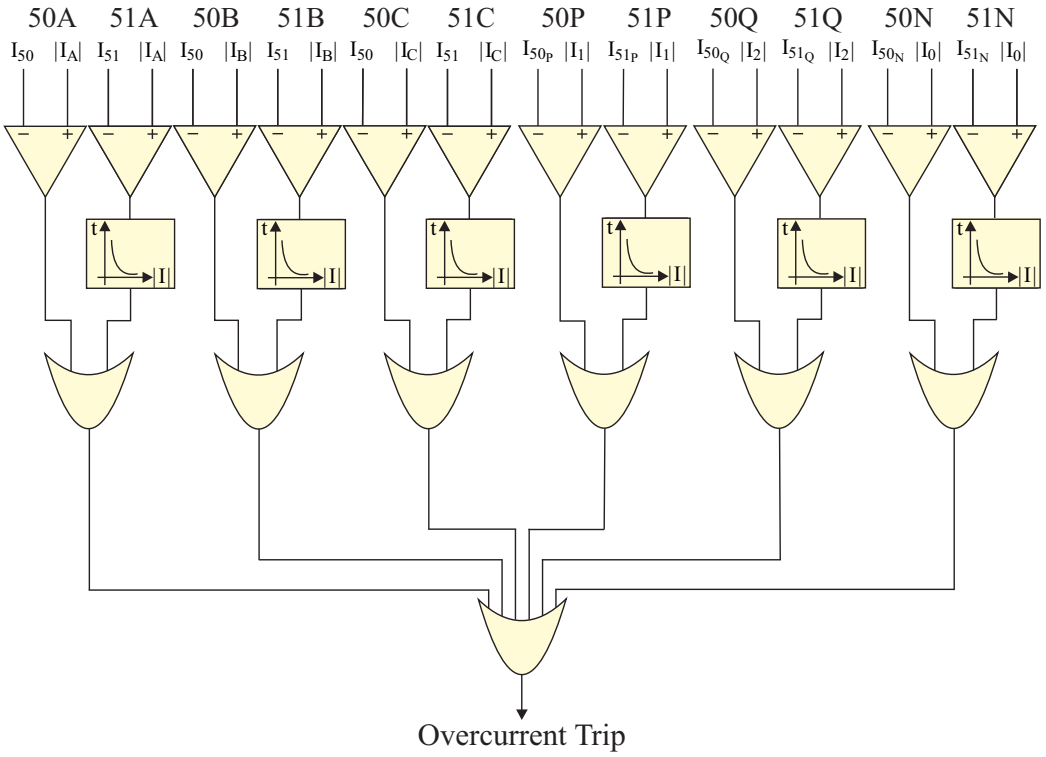

Figure 4.2: Instantaneous and time-delay overcurrent protection units.

The torque, at the current sampling k, is given by (ZIEGLER, 2011):

$$T_{op}(k) = |V_{pol}(k)||I_{op}(k)|\cos(\angle V_{pol}(k) - \angle I_{op}(k)), \tag{4.5}$$

where V_{pol} and I_{op} are fundamental phasors of the polarizing voltage and operating current, respectively, estimated through the full cycle Fourier algorithm; the underscripts $\{pol, op\}$ represent phase or line quantities as well as positive, negative, or zero sequences (Table 4.4). For instance: I_A, I_B, and I_C are phase current phasors; V_{BC}, V_{CA}, and V_{AB} are line voltage phasors, e.g., $V_{BC} = V_B - V_C$; I_1, I_2, and I_0 are positive, negative and zero sequence current phasors, respectively; V_1, V_2, and V_0 are positive, negative and zero sequence voltage phasors, respectively; Z_1 and Z_0 are positive and zero sequence line impedance, respectively.

By combining the overcurrents function (50 and 51) with directional funtion (32), the directional overcurrent function (67) is achieved.

The fault directionality is defined through the torque sign of (4.5): positive sign for forward fault and negative sign for reverse fault, obtained through the normalized torque ($\tilde{T}(k)$), as

Table 4.4: The conventional operating and polarizing quantities.

Directional Protection	Quantities	
	I_{op}	V_{pol}
Phase A (67A)	I_A	V_{BC}
Phase B (67B)	I_B	V_{CA}
Phase C (67C)	I_C	V_{AB}
Positive Sequence (67P)	I_1	$V_1(1\angle Z_1)$
Negative Sequence (67Q)	I_2	$-V_2(1\angle Z_1)$
Zero Sequence (67N)	I_0	$-V_0(1\angle Z_0)$

follows:

$$\tilde{T}_{op}(k) = \frac{T_{op}(k)}{|V_{pol}(k)||I_{op}(k)|}, \tag{4.6}$$

where $\tilde{T}_{op}(k)$ will be termed as torque factor in this thesis. Therefore, a forward fault is identified when:

$$\tilde{T}_{op}(k) = \cos(\angle V_{pol}(k) - \angle I_{op}(k)) > \varepsilon_{op}, \tag{4.7}$$

where $-1 \leq \tilde{T} \leq 1$; the threshold $\varepsilon_{op} > 0$ is used to enhance the reliability.

Phase units may have its diagnosis compromised in cases of reverse SLG faults when the infeed remote current exist and it was zero sequence predominant. In addition, the fault type need to be correctly identified in order to the directional protection works properly. During faults without the ground involvement (DL or LLL), the zero sequence unit is not applied. In balanced fault (LLL) the negative sequence unit has to be blocked to avoid false trigger. The phase units need to know the phases evolved in the fault to define which unit is reliable. Therefore, a fault type classifier is required to correctly chose the better units to deal with the fault present in the system. A summary of directional protection is illustrated in Figure 4.3, where the fault type classification enables which comparators should be used to assure the forward fault identification.

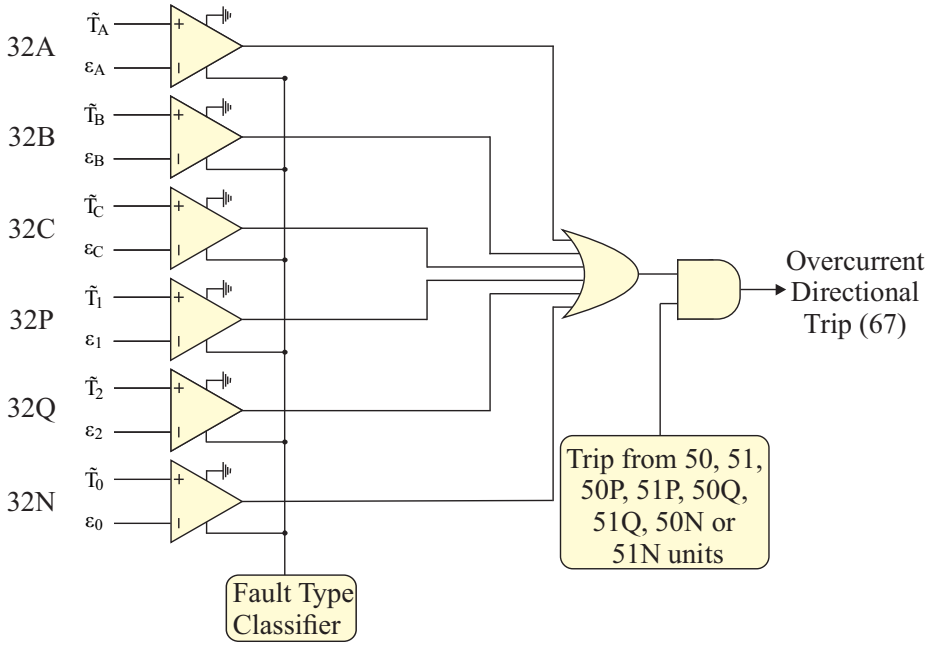

Figure 4.3: Directional protection units.

The overcurrent directional units 67A, 67B, 67C, 67Q and 67N are properly activated when the overcurrent modules of any current I_A, I_B, I_C, I_1, I_2, and I_0 reaches the time-delay pickup value (low threshold). The directional protection units are selected by a fault classifier and activated after the overcurrent units are sensitized. The final trip occurs when the overcurrent function and the proper directional units give a trigger.

4.4 Existing Wavelet-Based Overcurrent Function

According to Costa, Monti and Paiva (2017), the classical overcurrent units can be recreated by using the current scaling coefficient energy from the RT-SWT. These units do not require phasor estimation and provide a correct diagnosis in less time than the conventional method. Moreover, all the development of these units are based on classical logic, keeping the conservative side of protection. However, at the same time, this technique presents the possibility of a faster diagnosis of the fault by means of the high frequency components coming from the wavelet coefficient energy which attend the non-conservative protection side.

4.4.1 Wavelet-based Instantaneous Overcurrent Units

The wavelet-based instantaneous overcurrent units, as defined by Costa, Monti and Paiva (2017), will be activated whether at least one of scaling coefficient energy of the currents exceeds the instantaneous pickup energy ($E_{un_{50}}$), as follows:

$$\mathscr{E}^{s}_{i_{ph}} > E_{un_{50}}, \tag{4.8}$$

where ph and un_{50} variable can assume $ph = \{A,\ B,\ C,\ 1A,\ 1B,\ 1C,\ 2A,\ 2C,\ 2C,\ 0\}$ and $un_{50} = \{50,\ 50_P,\ 50_Q,\ 50_N\}$, for instance, the neutral wavelet-based instantaneous overcurrent unit will be activated whether the energy of the current zero sequence coefficient ($\mathscr{E}^{s}_{i_0}$) exceed the condition $\mathscr{E}^{s}_{i_0} > E_{50_N}$. The scaling coefficient energy of currents can be expressed in function of rms (root means square) current (I_{rms}), as follows (COSTA; MONTI; PAIVA, 2017):

$$\mathscr{E}^{s}_{i_{ph}} = \Delta k I^2_{rms}. \tag{4.9}$$

Therefore, the $E_{un_{50}}$ can be defined in terms of pickup current or reference current from the conventional protection, as follows:

$$E^{s}_{i_{un50}} = \Delta k I^2_{un_{50}} = \Delta k (Y_{un_{50}} I_{ph_r})^2. \tag{4.10}$$

Assuming $\mathscr{E}^{s}_{i_{ph_r}}$ as the scaling coefficient energy of the current provided from the average of the steady-state energy, (4.10) can be rewritten as follows:

$$E^{s}_{50} = Y^2_{un_{50}} \mathscr{E}^{s}_{i_{ph_r}}. \tag{4.11}$$

From (4.8) and (4.11), the wavelet-based instantaneous overcurrent units will be activated if the following condition is true:

$$\mathscr{E}^{s}_{i_{ph}} > Y^2_{un_{50}} \mathscr{E}^{s}_{i_{ph_r}}. \tag{4.12}$$

In the Table 4.5, the quantities associated to each wavelet-based instantaneous overcurrent unit are presented.

Table 4.5: Quantities to wavelet-based instantaneous overcurrent units.

Instantaneous Overcurrent Units	Quantities		
	$\mathscr{E}_{ph}$	$E_{un_{50}}$	$Y_{un_{50}}$
Phase A (50WA)	$\mathscr{E}_A$	E_{50}	Y_{50}
Phase B (50WB)	$\mathscr{E}_B$	E_{50}	Y_{50}
Phase C (50WC)	$\mathscr{E}_C$	E_{50}	Y_{50}
Positive Sequence A (50WPA)	$\mathscr{E}_{i_{1A}}$	E_{50_P}	Y_{50_P}
Positive Sequence B (50WPB)	$\mathscr{E}_{i_{1B}}$	E_{50_P}	Y_{50_P}
Positive Sequence C (50WPC)	$\mathscr{E}_{i_{1C}}$	E_{50_P}	Y_{50_P}
Negative Sequence A (50WQA)	$\mathscr{E}_{i_{2A}}$	E_{50_Q}	Y_{50_Q}
Negative Sequence B (50WQB)	$\mathscr{E}_{i_{2B}}$	E_{50_Q}	Y_{50_Q}
Negative Sequence C (50WQC)	$\mathscr{E}_{i_{2C}}$	E_{50_Q}	Y_{50_Q}
Zero Sequence (50WN)	$\mathscr{E}_{i_0}$	E_{50_N}	Y_{50_N}

Wavelet-based Time-delay Overcurrent Units

The wavelet-based time-delay overcurrent units are activated whether at least one of scaling coefficient energy of the currents exceeds the time-delay pickup energy ($E_{un_{51}}$), as follows:

$$\mathscr{E}^s_{i_{ph}} > E_{un_{51}} = Y^2_{un_{51}} \mathscr{E}^s_{ir}. \tag{4.13}$$

where un_{51} variable can assume $un_{51} = \{51,\ 51_P,\ 51_Q,\ 51_N\}$, for instance, the neutral wavelet-based time-delay overcurrent unit will start the time counting whether the energy of the current zero sequence coefficient ($\mathscr{E}^s_{i_0}$) exceed the condition $\mathscr{E}^s_{i_0} > E_{51_N}$. In Table 4.6, all the time-delay units are defined with its respectively quantities.

Table 4.6: Quantities to wavelet-based time-delay overcurrent units.

Time-delay Overcurrent Units	Quantities		
	$\mathscr{E}_{ph}$	$E_{un_{51}}$	$Y_{un_{50}}$
Phase A (50WA)	$\mathscr{E}_A$	E_{51}	Y_{51}
Phase B (50WB)	$\mathscr{E}_B$	E_{51}	Y_{51}
Phase C (50WC)	$\mathscr{E}_C$	E_{51}	Y_{51}
Positive Sequence A (50WPA)	$\mathscr{E}_{i_{1A}}$	E_{51_P}	Y_{51_P}
Positive Sequence B (50WPB)	$\mathscr{E}_{i_{1B}}$	E_{51_P}	Y_{51_P}
Positive Sequence C (50WPC)	$\mathscr{E}_{i_{1C}}$	E_{51_P}	Y_{51_P}
Negative Sequence A (50WQA)	$\mathscr{E}_{i_{2A}}$	E_{51_Q}	Y_{51_Q}
Negative Sequence B (50WQB)	$\mathscr{E}_{i_{2B}}$	E_{51_Q}	Y_{51_Q}
Negative Sequence C (50WQC)	$\mathscr{E}_{i_{2C}}$	E_{51_Q}	Y_{51_Q}
Zero Sequence (50WN)	$\mathscr{E}_{i_0}$	E_{51_N}	Y_{51_N}

The final trip from these units will be sent after the counter achieve time defined from the inverse curves, as follows:

$$t \geq \frac{k_{un_{51}}}{f_s} + T_P, \tag{4.14}$$

where t current time; $k_{un_{51}}$ is the k-th sample at which the overcurrent time-delay threshold was sensitized; f_s is the sampling frequency; T_P is the delay time from the inverse curve that varies with the currents levels. As presented in (4.9), the scaling coefficient energy has a practicable

relation with rms currents. Therefore, (4.2) can be defined to cover the scaling coefficient energy, as follows (COSTA; MONTI; PAIVA, 2017):

$$T_P = \left(\frac{\delta}{\left(\frac{\mathscr{E}^s_{i_{ph}}(k)}{E_{un_{51}}} \right)^{\rho/2} - 1} + \gamma \right) TMS, \tag{4.15}$$

where δ, γ and ρ were previous defined in Table 4.2. The comparison of the inverse curves in terms of current magnitudes and current scaling coefficient energy are presented in Figure 4.4. The wavelet curves were designed to achieve the same general behaviour of the conventional curves. Therefore, the axis X present higher values due to the scaling coefficient energy following (4.15).

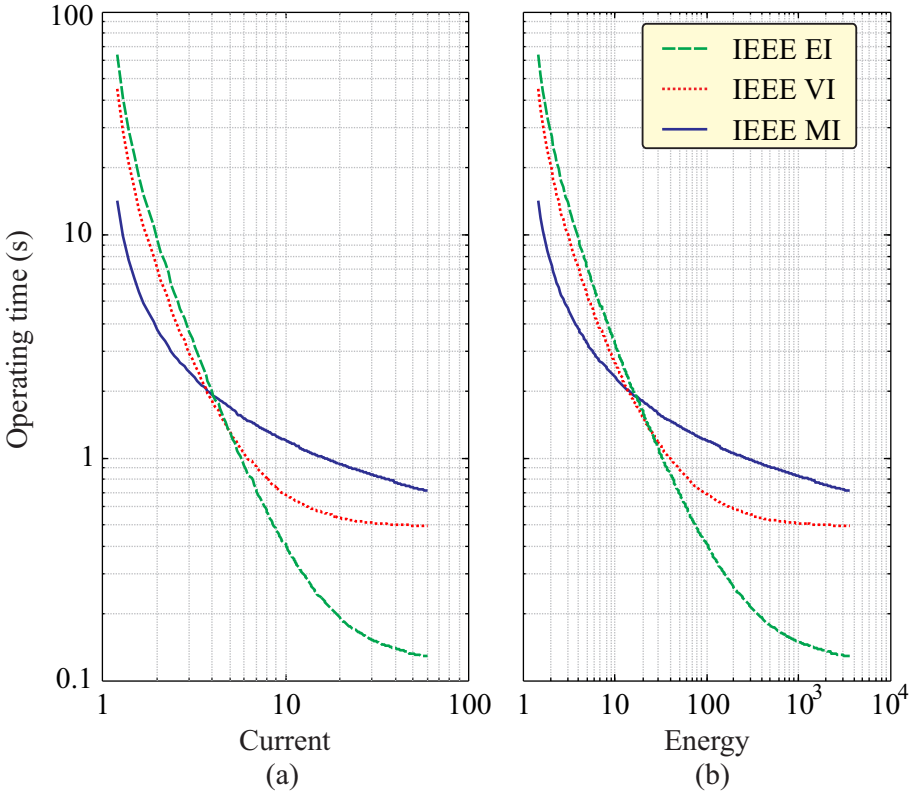

Figure 4.4: Overcurrent inverse-time relay curves: (a)IEEE standard; (b)wavelet-based inverse curves. **Source**: (COSTA; MONTI; PAIVA, 2017)

4.5 Existing Wavelet-Based Fault Classification

As aforementioned, the directional protection requires a unit selector to correctly identify the appropriated directional unit for each fault type. The wavelet fault classifier proposed in (COSTA; SOUZA; BRITO, 2012b) was an attempt to classify the ten fault types by using RT-SWT. The wavelet coefficient energy from the three phases and the zero is computed and they are used to associate one fault type to each sample, after half cycle the most frequently fault

type is declared to be the correctly fault type. The energy from phases and zero are computed to each sample, when a fault is detected the energies are normalized and the logic flow sequence is computed to each sample, as follows:

- If $G(k) > 0.1$:
  (a) If $B(k) < 1/3$ and $C(k) < 1/3$, so fault type is AG.
  (b) Otherwise, $C(k) < 1/3$ and $A(k) < 1/3$, so fault type is BG.
  (c) Otherwise, $A(k) < 1/3$ and $B(k) < 1/3$, so fault type is CG.
  (d) Otherwise, $A(k) \geq 1/3$ and $B(k) \geq 1/3$, so fault type is ABG.
  (e) Otherwise, $B(k) \geq 1/3$ and $C(k) \geq 1/3$, so fault type is BCG.
  (f) Otherwise, $C(k) \geq 1/3$ and $A(k) \geq 1/3$, so fault type is CAG.
- Otherwise:
  (a) Otherwise, $A(k) \geq 1/3$ and $B(k) \geq 1/3$, so fault type is AB.
  (b) Otherwise, $B(k) \geq 1/3$ and $C(k) \geq 1/3$, so fault type is BC.
  (c) Otherwise, $C(k) \geq 1/3$ and $A(k) \geq 1/3$, so fault type is CA.
  (d) Otherwise, fault type is ABC.

where, $A(k)$, $B(k)$, $C(k)$ and $G(k)$ are, repetitively, the normalized current energy from phase A, phase B, phase C and ground by using the RT-SWT.

In Figures 4.5 and 4.6, the fault classifier proposed by (COSTA; SOUZA; BRITO, 2012b) was used to classify the 1810 fault cases performed in the system described in Section 8.1 varying the fault type and fault inception angle. The SLG and DL faults are clearly separated in distinct regions inside the triangle by using only the energy from the three phases, as depicted in Figure 4.5(a) and (b), respectively. Additionally, the SLG faults present a higher level of energy from zero components compared to DL faults. On the other hand, the energy distribution on the triangle to DLG and LLL are harder to be able to isolate the fault types among them and among the previous fault types, as seen in Figure 4.5(a) and (b), respectively. The LLL can be differentiated from SLG and DLG faults due to its lack of high zero information. However, some LLL faults could be misclassified as DL and some the DLG fault can be miscalssified as SLG faults in certain fault inception angles.

In this thesis a fault classifier is proposed by using RT-BSWT in order to overcome the issues faced by the previous discussed method. The method proposed by (COSTA; SOUZA; BRITO, 2012b) is going to be compared compared with the proposed method in Section 8.1.2.

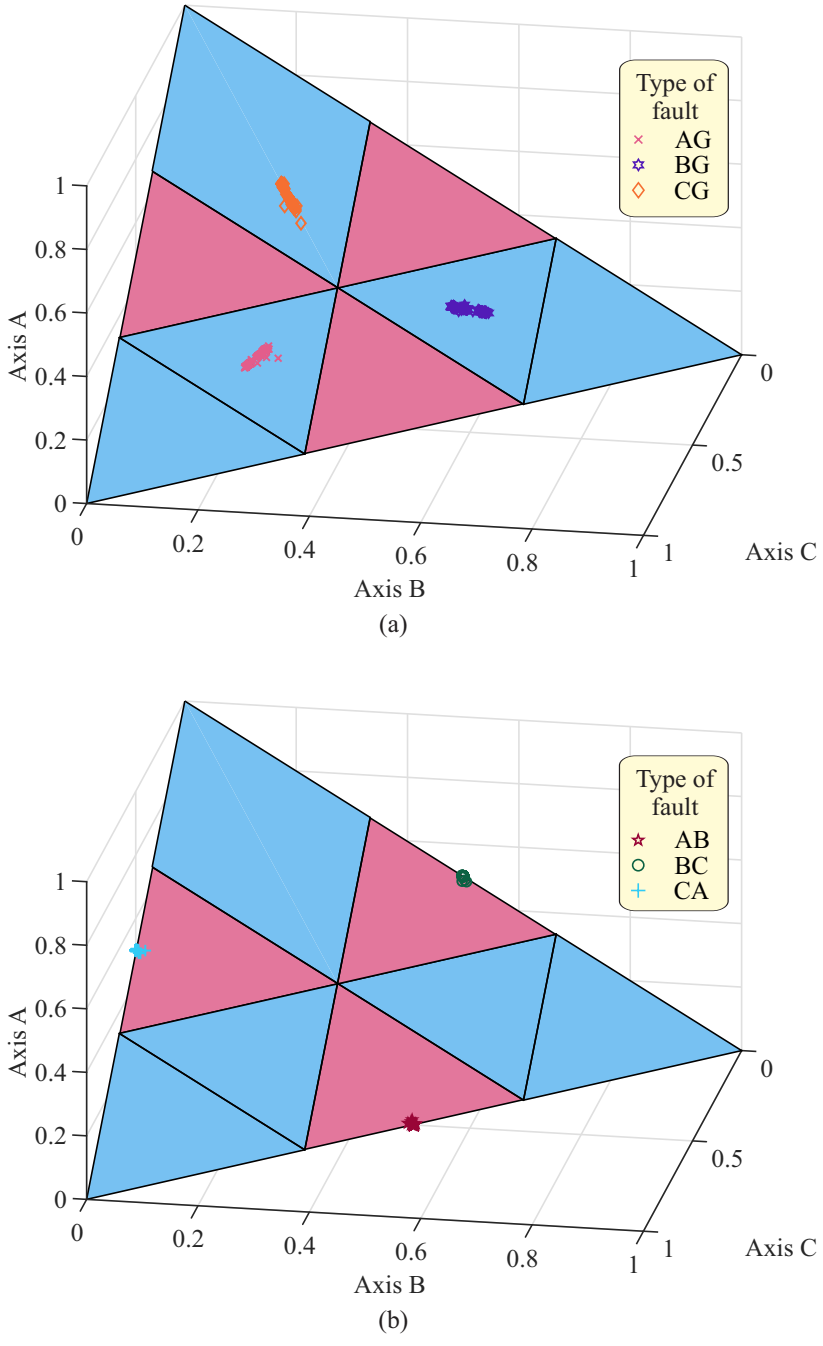

Figure 4.5: Classifier proposed in (COSTA; SOUZA; BRITO, 2012b): (a)SLG faults; (b)DL faults.

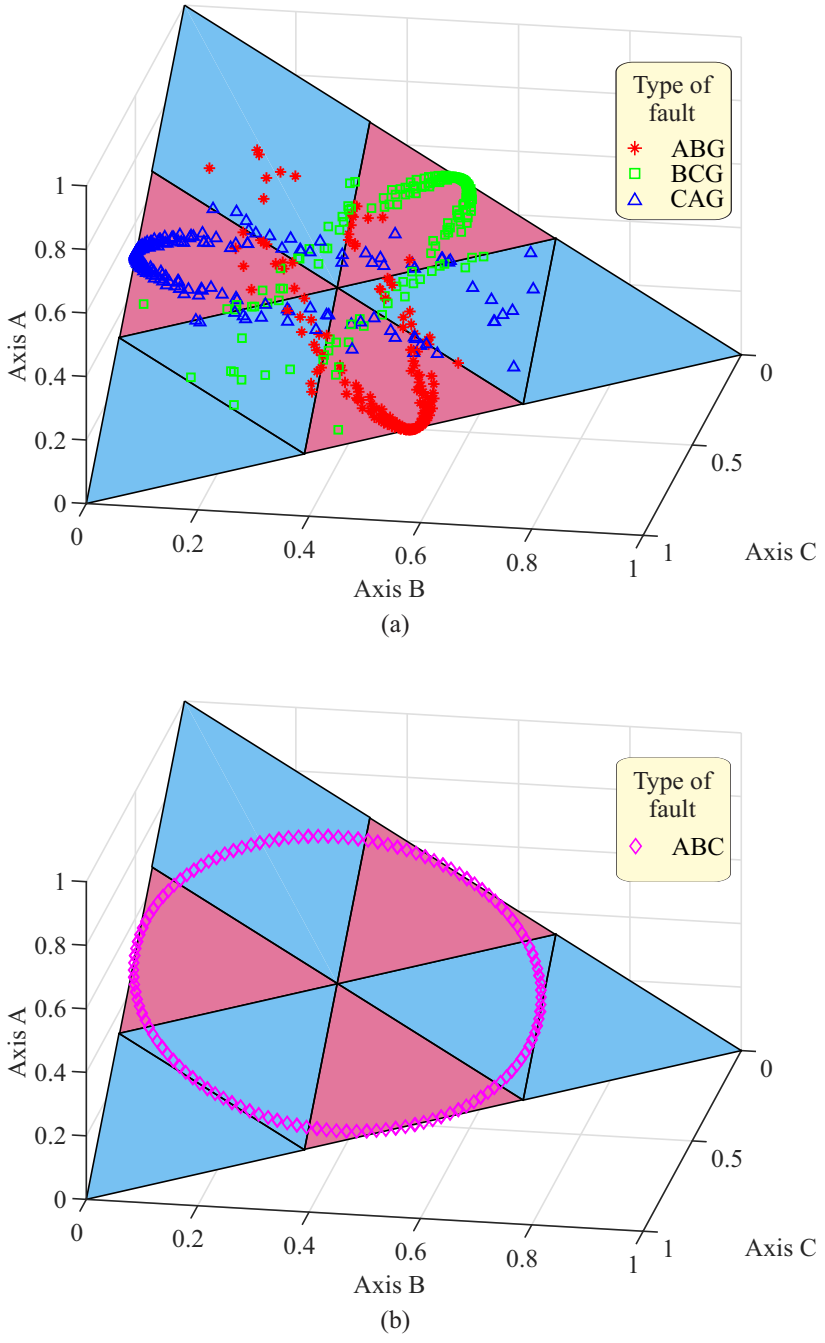

Figure 4.6: Classifier proposed in (COSTA; SOUZA; BRITO, 2012b): (a)DLG faults; (b)LLL faults.

4.6 Summary

In this chapter, the basic principals of Fourier-based overcurrent protection and directional overcurrent protection were summarized. These traditional protections were presented to be used as comparative methods to the proposed protection. In addition, the wavelet-based overcurrent protection methodology were presented and the necessity of a fault type classifier was highlighted.

Chapter 5

The Proposed Wavelet-Based Directional Method

In this chapter, an improved directional protection based on the real-time SWT (RT-SWT) is described. By using only the first level, the scaling coefficients are used in replacement of the Fourier transform in order to recreate the conventional directional protection, and four conventional-based protection units are proposed (wavelet directional units): phase (67W) and positive (67PW), negative (67QW), and zero (67NW) sequences. The torque equations were mathematically redefined in the wavelet domain by using sampled voltages and currents. The wavelet coefficients are used for fast detection of fault-induced transients (wavelet activators) in order to reduce the relay operating time, whereas the scaling coefficients are used for backup activation in accordance with the overcurrent protection (wavelet overcurrent activators).

5.1 The Wavelet-Based Overcurrent Directional Protection

The wavelet-based overcurrent units process currents and voltages from the power system and verifies if there is an overcurrent which increase the current wavelet and scaling coefficients above the operating thresholds (pickup energy). The proposed directional units operate in parallel with the overcurrent protection and provide the diagnosis if the fault is forward or reverse to the monitoring point. Therefore, similarly to classical protection, the proposed method would only send the trip when the overcurrent unit identifies the fault and the directional unit reports that the fault is forward, after the correctly units being selected by a fault classifier.

The procedures mentioned in the pre-possessing of the classical protection in Chapter 4 are also required here, with the exception of phasor estimation, which does not require the use of Fourier algorithm. The CTs and CCVTs acquire currents and voltages, respectively, from the system. These related discretized inputs are used by the phase, positive sequence, negative sequence and zero sequence wavelet-based directional overcurrent units as presented in Figure 5.1. When a forward fault is identified, the flag is sent informing the direction of the possible fault, since the fault being recognized for a main protection, for instance, overcurrent protection, the circuit breaker (52) opening will be requested.

5.1.1 The Proposed Wavelet-Based Directional Functions

The true rms value (x_{rms}) of x in a cycle is given by (COSTA; DRIESEN, 2013):

$$x_{rms}(k) = \sqrt{\frac{1}{\Delta k} \sum_{n=k-\Delta k+1}^{k} x^2(n)}. \tag{5.1}$$

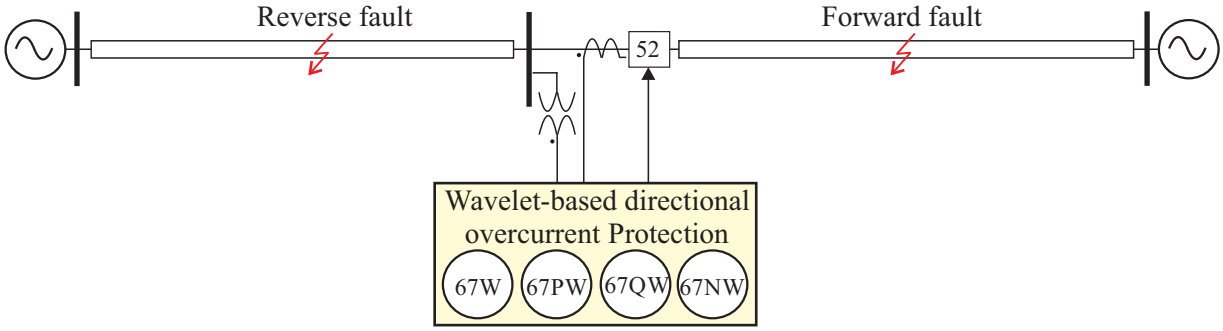

Figure 5.1: Proposed wavelet-based directional overcurrent units.

Based on the Percival theorem (PERCIVAL; WALDEN, 2000), the rms value can be rewritten in terms of scaling and wavelet coefficient energies, at the first level, as follows:

$$x_{rms}(k) = \sqrt{\frac{1}{\Delta k}\left(\sum_{n=k-\Delta k+1}^{k} s_x^2(n) + \sum_{n=k-\Delta k+1}^{k} w_x^2(n)\right)}. \tag{5.2}$$

A proper sampling rate ($f_s >> f$) can assure the fundamental and relevant harmonic components placed on the band frequency of the scaling coefficients, yielding wavelet coefficients irrelevant during the steady-state period ($\sum w_x^2 << \sum s_x^2$). Therefore, (5.2) is approximated to:

$$x_{rms}(k) \approx \sqrt{\frac{1}{\Delta k}\sum_{n=k-\Delta k+1}^{k} s_x^2(k)} = \sqrt{\frac{\mathscr{E}_x^s}{\Delta k}}. \tag{5.3}$$

Based on (ALVES et al., 2017), but including some modifications such as the use of scaling coefficients instead of wavelet coefficients and the use of only the first level, the scaling active power (P^s) and apparent power (S^s) are proposed here as:

$$P^s(k) \approx \frac{1}{\Delta k}\sum_{n=k-\Delta k+1}^{k} s_v(n)s_i(n), \tag{5.4}$$

$$S^s(k) \approx \frac{1}{\Delta k}\sqrt{\sum_{n=k-\Delta k+1}^{k} s_v(n)\sum_{n=k-\Delta k+1}^{k} s_i(n)} \approx \frac{1}{\Delta k}\sqrt{\mathscr{E}_v^s \mathscr{E}_i^s}, \tag{5.5}$$

where s_v and s_i are voltage and current scaling coefficients, respectively; $\mathscr{E}_v^s$ and $\mathscr{E}_i^s$ are voltage and current scaling coefficient energies, respectively. The superscript s in power quantities indicates the scaling coefficients.

Based on the classical power theory (STEINMETZ, 1916), the power factor is the ratio between active and apparent power. Equivalently, the scaling power factor (PF^s) is the ratio between scaling active and apparent power, which is approximated to the actual power factor as follows:

$$PF^s(k) = \frac{P^s(k)}{S^s(k)} = \frac{\sum_{n=k-\Delta k+1}^{k} s_v(n)s_i(n)}{\sqrt{\mathscr{E}_v^s \mathscr{E}_i^s}} \approx \cos(\angle V - \angle I) = \cos(\theta), \tag{5.6}$$

where θ is the angle between the voltage and current at the same phase, and the power factor is lead or lag (always positive) in accordance with the displacement between the phase voltage

and current.

Based on the scaling power factor defined in (5.6), and using operating current and polarizing voltage instead of phase current and voltage, respectively, this work proposes the scaling torque factor ($\tilde{T_{op}}^{s}$) as follows:

$$\tilde{T}^{s}_{op}(k) = \frac{\sum_{n=k-\Delta k+1}^{k} s_{v_{pol}}(n) s_{i_{op}}(n)}{\sqrt{\mathscr{E}^{s}_{v_{pol}}(k)\mathscr{E}^{s}_{i_{op}}(k)}}, \tag{5.7}$$

where $-1 \leq \tilde{T_o p}^{s} \leq 1$; $f_s \geq 8f$, which is required to the fundamental frequency be less or equal to the center frequency of the scaling filter at the first decomposition level, minimizing the influence of the fundamental frequency in the wavelet coefficients; $s_{v_{pol}}$ is the polarizing voltage scaling coefficient; $s_{i_{op}}$ is the operating current scaling coefficient; $\mathscr{E}^{s}_{v_{pol}}$ is the polarizing voltage scaling coefficient energy; $\mathscr{E}^{s}_{i_{op}}$ is the operating current scaling coefficient energy.

Based on (4.5), the directionality is defined by the sign of $\tilde{T}^{s}_{op}(k)$, and a forward fault is detected when:

$$\tilde{T}^{s}_{op}(k) > \varepsilon_{op}. \tag{5.8}$$

The wavelet-based positive, negative and zero sequence directional units use, as operating current, the positive (i_{1A}, i_{1B}, i_{1C}), negative (i_{2A}, i_{2B}, i_{2C}), and zero (i_0) sequence currents, respectively, computed with samples instead of phasors (symmetrical components in time domain according to (3.16)-(3.22)). Therefore, the operating current considers both current and past samples. Table 5.1 summarizes the directional protection units proposed in this work and its association with the respective polarizing voltages and operating currents.

Table 5.1: The proposed operation and polarization quantities.

Wavelet-Based Directional Protection	Quantities	
	I_{op}	V_{pol}
Phase A (67WA)	$i_A(k)$	$v_{BC}(k)$
Phase B (67WB)	$i_B(k)$	$v_{CA}(k)$
Phase C (67WC)	$i_C(k)$	$v_{AB}(k)$
Pos. Seq. A (67PWA)	$i_{1A}(k)$	$v_A(k-\Delta k_{Z_1}) + v_B(k-\Delta k_\alpha - \Delta k_{Z_1}) + v_C(k-\Delta k_{\alpha^2} - \Delta k_{Z_1})$
Pos. Seq. B (67PWB)	$i_{1B}(k)$	$v_A(k-\Delta k_{\alpha^2} - \Delta k_{Z_1}) + v_B(k-\Delta k_{Z_1}) + v_C(k-\Delta k_\alpha - \Delta k_{Z_1})$
Pos. Seq. C (67PWC)	$i_{1C}(k)$	$v_A(k-\Delta k_\alpha - \Delta k_{Z_1}) + v_B(k-\Delta k_{\alpha^2} - \Delta k_{Z_1}) + v_C(k-\Delta k_{Z_1})$
Neg. Seq. A (67QWA)	$i_{2A}(k)$	$v_A(k+\frac{\Delta k}{2} - \Delta k_{Z_1}) + v_B(k-\Delta k_{\alpha^2} + \frac{\Delta k}{2} - \Delta k_{Z_1}) + v_C(k-\Delta k_\alpha + \frac{\Delta k}{2} - \Delta k_{Z_1})$
Neg. Seq. B (67QWA)	$i_{2B}(k)$	$v_A(k-\Delta k_\alpha + \frac{\Delta k}{2} - \Delta k_{Z_1}) + v_B(k+\frac{\Delta k}{2} - \Delta k_{Z_1}) + v_C(k-\Delta k_{\alpha^2} + \frac{\Delta k}{2} - \Delta k_{Z_1})$
Neg. Seq. C (67QWA)	$i_{2C}(k)$	$v_A(k-\Delta k_{\alpha^2} + \frac{\Delta k}{2} - \Delta k_{Z_1}) + v_B(k-\Delta k_\alpha + \frac{\Delta k}{2} - \Delta k_{Z_1}) + v_C(k+\frac{\Delta k}{2} - \Delta k_{Z_1})$
Zero Seq. (67NW)	$i_0(k)$	$v_A(k+\Delta k/2 - \Delta k_{Z_0}) + v_B(k+\Delta k/2 - \Delta k_{Z_0}) + v_C(k+\Delta k/2 - \Delta k_{Z_0})$

Based on the classical protection (ROBERTS; GUZMAN, 1994), the polarizing voltages of the positive and negative sequence directional units present an additional angle displacement particle as a function of the positive sequence line impedance angle ($\angle Z_1$), in radians, which is rewritten in sampling terms as follows:

$$\Delta k_{Z_1} = \Delta k - \left\lfloor \frac{\Delta k \angle Z_1}{2\pi} \right\rfloor, \tag{5.9}$$

whereas the zero sequence directional unit presents an angle displacement particle as a function

of the zero sequence line impedance angle, which in sampling terms becomes:

$$\Delta k_{Z_0} = \Delta k - \left\lfloor \frac{\Delta k \angle Z_0}{2\pi} \right\rfloor. \tag{5.10}$$

Both negative and zero sequence units need an additional half-cycle angle displacement particle ($\Delta k/2$) according to the classical directional definition in Table 4.4.

Figures 5.2 and 5.3 depict examples of wavelet- and Fourier-based directional protection units under ABG reverse and forward faults with fault distance, inception angle, and resistance being $d_f = 100$, $\theta_f = 20^\circ$, and $r_f = 1.0\ \Omega$, respectively simulated in a power system which will be properly addressed in Section 6.1. The general performance of both wavelet- and Fourier-based torque factors were similar (Figures 5.2 and 5.3): all the torque factors converged to the minimum value in reverse faults and to the maximum value in forward faults after the transient period (with the exception of the units 67C and 67WC), i.e., the directionality in all units was correct for this kind of fault. Conversely, the wavelet- and Fourier-based torque factors presented their particularities:

1. The wavelet-based positive and negative units have three quantities instead of one. However, the best one can easily be identified through a faulted phase selection or a fault classifier.
2. The best wavelet-based units (67PWA and 67QWA in Figures 5.3(c) and (d)) were faster than the related conventional units.

5.1.2 The Scaling Directional Triggering (Overcurrent Triggering)

By using the RT-SWT, all overcurrent units could be recreated as previously presented (COSTA; MONTI; PAIVA, 2017). However, in this work, only the time-delay overcurrent conditions (scaling trigger) will be verified to activate the wavelet directional units by using (4.13) without waiting for the intentional delay. Therefore, the scaling trigger proposed is defined in terms of operating current, as follows:

$$\mathscr{E}^{s}_{i_{op}} > Y^2_{un_{51}} \mathscr{E}^{s}_{ir_{op}}. \tag{5.11}$$

The wavelet based direcional protection will be activated if the condition (5.11) is true for any operating current scalling coefficient energy.

5.1.3 The Wavelet Directional Triggering

The operating current wavelet coefficients energy ($\mathscr{E}^{w}_{i_{op}}$) provides an additional and fast triggering method as follows (wavelet trigger):

$$\mathscr{E}^{w}_{i_{op}}(k) > E^{w_{pickup}}_{i_{op}}, \tag{5.12}$$

where $E^{w_{pickup}}_{i_{op}}$ is the wavelet coefficient energy pickup statistically defined in terms of the average energy obtained through the Gaussian noise presented in the steady-state ($\mu\varepsilon_{op}$) to each unit (MEDEIROS; COSTA; SILVA, 2016), as follows:

$$\mathscr{E}^{w}_{i_{op}}(k) = \mu\varepsilon_{op}. \tag{5.13}$$

The proposed directional function defined in (5.8) is enabled when (4.13) or (5.12) is true.

By using the wavelet activator, faults are identified faster and the directionality can be computed earlier. In addition, the wavelet information can be used to identify the fault type needed by the directional protection, which will be better explored in the chapter 7. However, as the RT-SWT was used to developed this method, same faults with dumped transients can be difficult for the wavelet trigger to detect. In these cases, the scaling trigger will identifies and activates the directional units.

5.1.4 The Proposed Method Algorithm

A summary of the proposed wavelet-based directional method, per sampling time, is presented in the flowchart in Figure 5.4. The currents and voltages are acquired from the system and its sequence components are computed. The phase and sequence operating currents and polarizing voltages are obtained. By using these operating currents, the wavelet coefficients and energies are computed to define the wavelet trigger (wavelet activator). The scaling coefficients and energies of the polarizing voltages and operating currents are computed. By using the operating current scaling coefficient energies, the scaling trigger (scaling activator) is defined. If at least one of these two activators were activated the directionality is computed. The active and apparent power are defined through voltages and currents computed from the scaling coefficients and energies. The torque factor is computed by using the active and apparent power information and the directional diagnostic is obtained by competing with the threshold defined to each unit. A unit selection is necessary to correctly identify which units are capable of acting during each fault. The final trip is reached if the fault is forward and the protection associated with the directional is activated.

5.1.5 Unit Selection

According to Figure 5.3, the phase protection units 67A, 67B, 67WA and 67WB (conventional and wavelet) offered an appropriate diagnosis for the ABG fault. However, 67C and 67WC did not give an appropriate directionality, since the fault did not involve the phase C, which means that both protections should consider a proper phase selection, for instance, a fault classifier as proposed in Chapter 7.

The wavelet-based directional units that should be activated through a phase selection according to the fault type are summarized in Table 5.2. Therefore, the fault type identification as being SLG, DLG, DL or LLL is not enough to correctly select the units for the proposed directional protection. The phases involved into the fault requires to be known in order to activate the respective units. The ideal unit selector must be a fast, reliable and accurate fault classifier able to identify the ten fault types. In order to reach the defined requirements to support the directional protection, a fault classifier is proposed in Chapter 7.

Table 5.2: Wavelet-based directional units activation per fault type.

Wavelet-based Directional Unit	Fault Type
67WA	AG, ABG, CAG, AB, CA, ABC
67WB	BG, ABG, BCG, AB, BC, ABC
67WC	CG, BCG, CAG, BC, CA, ABC
67PWA	AG, ABG, CAG, AB, CA, ABC
67PWB	BG, ABG, BCG, AB, BC, ABC
67PWC	CG, BCG, CAG, BC, CA, ABC
67QWA	AG, ABG, CAG, AB, CA
67QWB	BG, ABG, BCG, AB, BC
67QWC	CG, BCG, CAG, BC, CA
67NW	AG, BG, CG, ABG, BCG, CAG

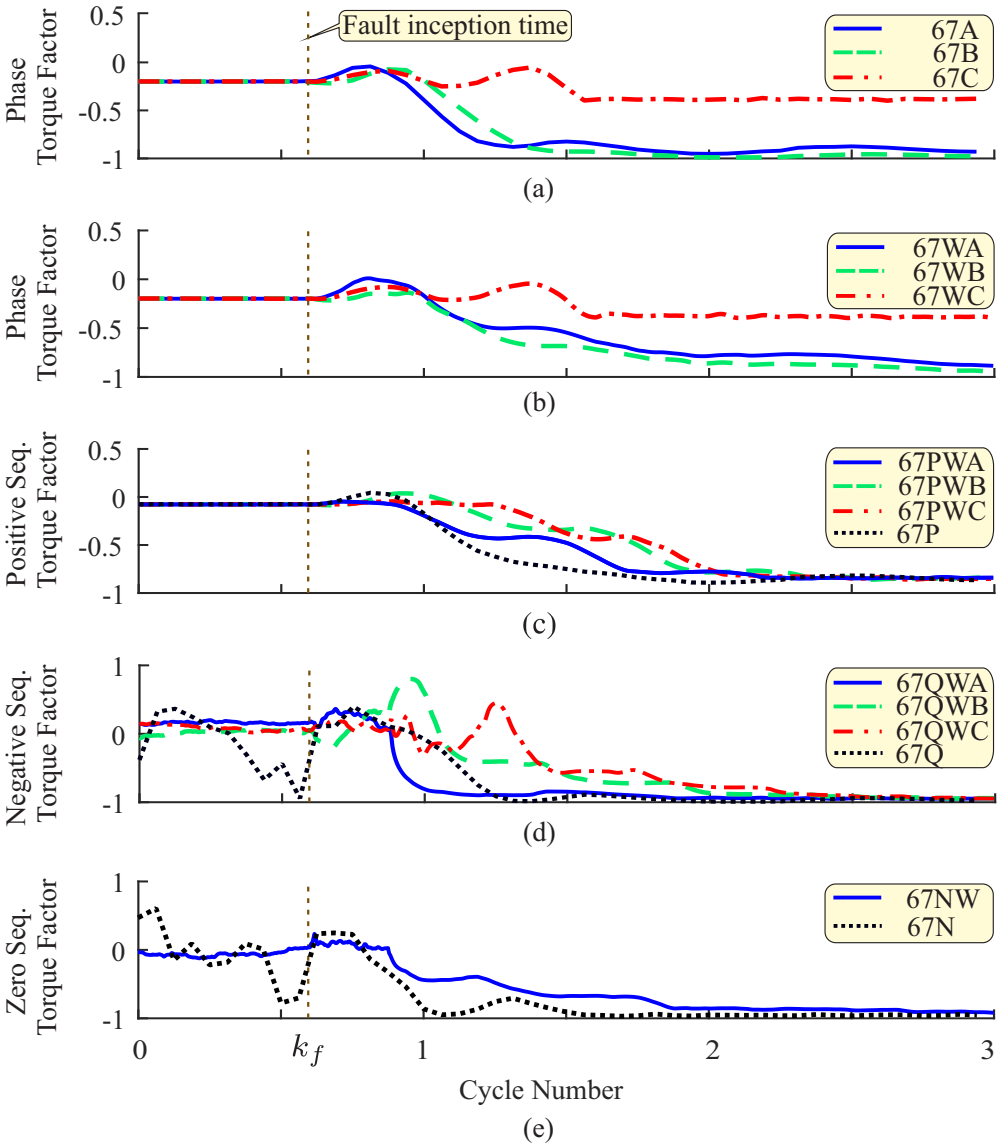

Figure 5.2: ABG reverse fault: a) Fourier-based phase module; b) wavelet-based phase module; c) Fourier- and wavelet-based positive sequence modules; d) Fourier- and wavelet-based negative sequence modules; e) Fourier- and wavelet-based zero sequence modules.

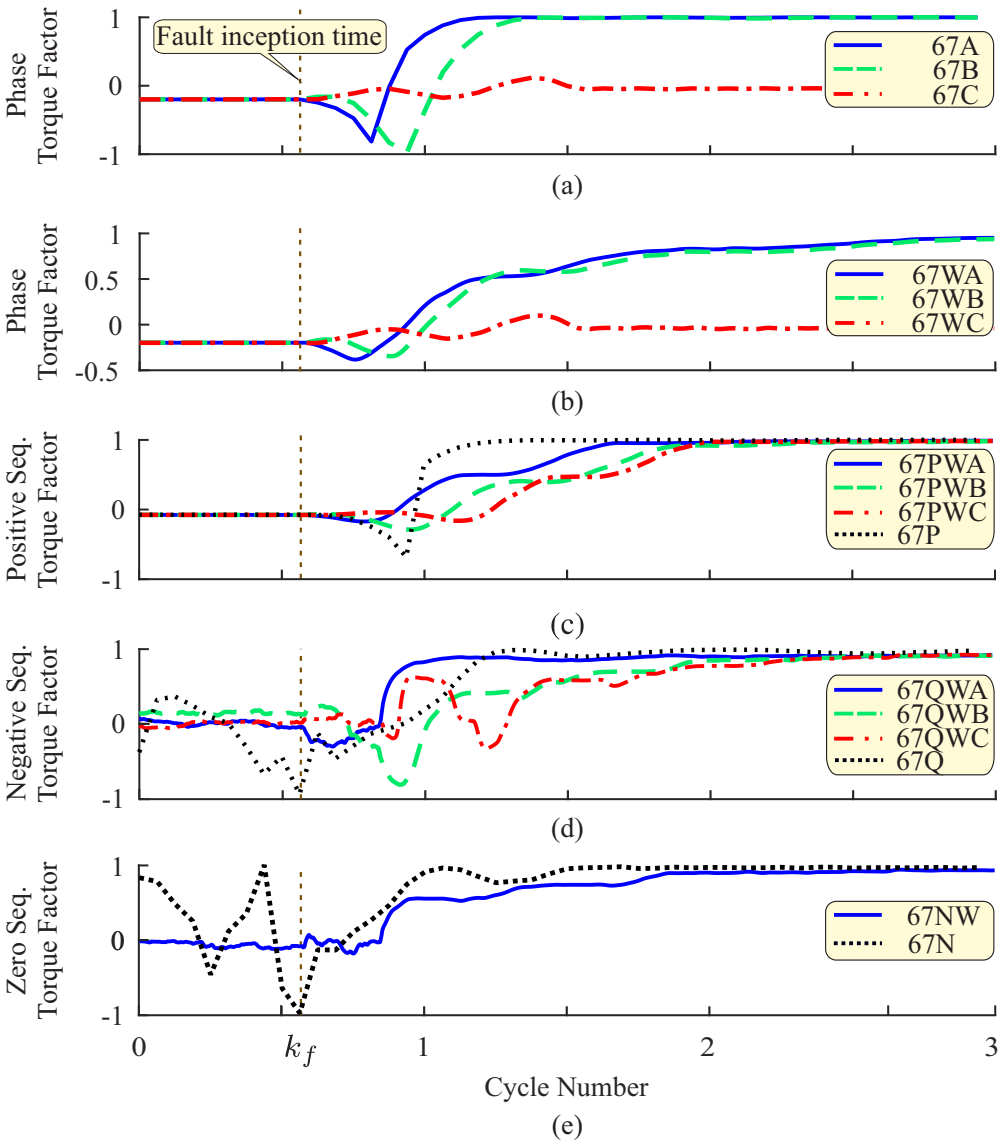

Figure 5.3: ABG forward fault: a) Fourier-based phase module; b) wavelet-based phase module; c) Fourier- and wavelet-based positive sequence modules; d) Fourier- and wavelet-based negative sequence modules; e) Fourier- and wavelet-based zero sequence modules.

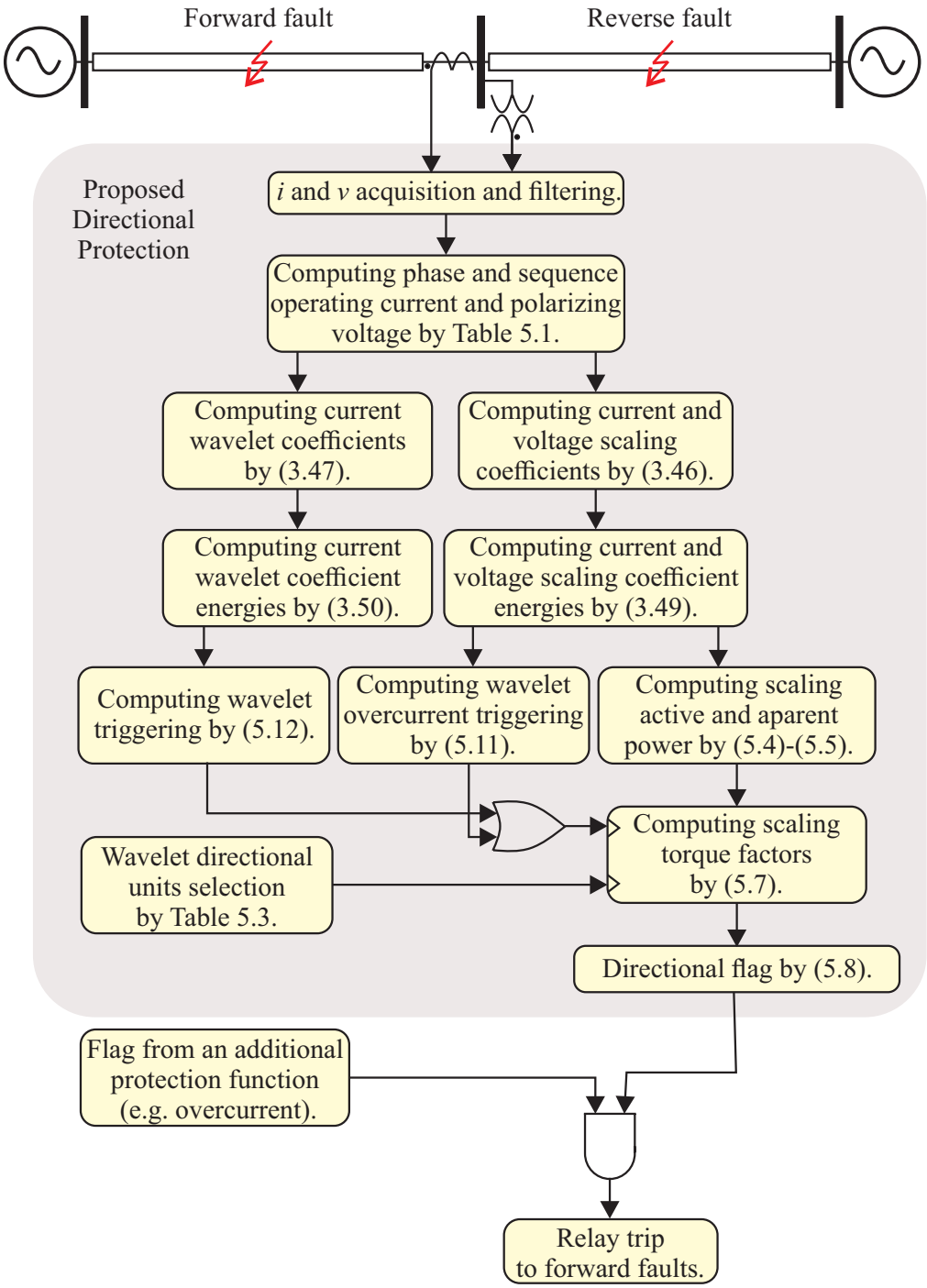

Figure 5.4: The wavelet-based directional overcurrent protection flowchart per sampling time.

5.2 Summary

In this chapter the description of phase, positive, negative and zero sequence overcurrent directional protections were presented using the wavelet transform. Wavelet overcurrent units are implemented by the energies of the current scale coefficients, while the product between the current and voltage scale coefficients is used to provide the directional diagnosis. In addition, a fault classifier was highlighted as necessary to the proposed protection works properly, following the same behaviour of the conventional directional overcurrent protection. A summary of the proposed method is presented in Figure 7.4.

Chapter 6

Performance Assessment of the Proposed Directional Protection

In this chapter, several evaluations are reported in order to demonstrate the robustness of the proposed wavelet-based directional overcurrent protection. The results are mainly performed in transmission system and same specific studies are performed in a distribution system with distributed generation.

6.1 Transmission System and Protection Parameterization

A simple transmission system was designed based on the 230 kV IEEE power system test parameters (COMMITTEE et al., 2004), the system in Figure 8.13 was considered for evaluating the performance of both the proposed wavelet-based directional protection as well as the classical Fourier-based directional method. The lines present the same length (L1 = L2 = 200 km) and were modeled with distributed parameters. The CTs and CCVT were considered ideals. The relay was strategically positioned at bus B2 to trip for forward faults on line L1, whereas no trip must be issued for reverse faults on line L2. The final trip occurs when both overcurrent and directional protections trip. However, the overcurrent behavior is not the objective of this thesis.

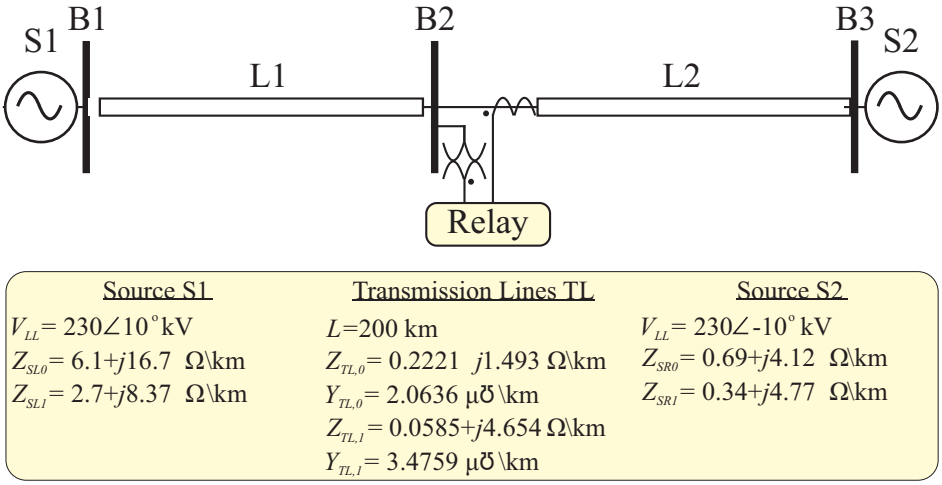

Figure 6.1: 230 kV IEEE system.

A typical 40 db SNR (Signal-to-Noise Ratio) was added to the simulated signals to make

them more realistic. A second order Butterworth filter, described as follows:

$$\frac{1}{s^2 + 1.412s + 1} \tag{6.1}$$

was used as the antialiasing filter. The time-delay pickup overcurrent thresholds to activate the directional protections are summarized in Table 6.1. These thresholds are valid for both Fourier- and wavelet-based overcurrent protections, and were set empirically for the sake of simplicity since the overcurrent protection performance verification and coordination are not the goals of this work.

The Fourier-based protection uses the conventional sampling frequency of fs = 960 Hz, whereas the wavelet-based method needs a higher one and uses a sampling frequency of $f_s =$ 15360 Hz, which is also practical in protective relays currently (COSTA; SOUZA; BRITO, 2012b). The full cycle Fourier algorithm was used to estimated the phasors. The conventional protection is based on (4.7) and supported by Table 4.4, whereas the proposed wavelet-based protection is based on (5.7) and supported by Table 5.1. The faulted phases are considered to be known to all evaluations for the sake of simplicity. However, a fault classifier is also detailed in the follow chapter.

Table 6.1: Overcurrent protection thresholds.

Protection Units	$Y_{un_{51}}$
Phase (51)	2.0
Positive Sequence (51P)	2.0
Negative Sequence (51Q)	0.2
Zero Sequence (51N)	0.2

Some torque factors (Fourier and wavelet) in Figure 5.2 (expected to be lower than zero) were higher than zero during the fault transient period. Fortunately, all of the selected units converged accurately to the right answer after the fault transient period. Therefore, suitable directional thresholds can be set to overcome this problem. This work considered that: the phase and positive units are accurate, and the torque factor needs small thresholds; negative and zero sequence units are sensitive and require high thresholds. Therefore, the directional thresholds (wavelet and Fourier) the same ones used for both were set based on preliminary evaluations to identify how the directional units behave under the system configurations, which leads to define the threshold presented in Table 6.2.

Table 6.2: Directional protection thresholds.

Protection Modules	ε_{op}
Phase	0.10
Positive Sequence	0.10
Negative Sequence	0.70
Zero Sequence	0.75

6.2 Proposed Wavelet-based Protection Evaluation

The proposed method was firstly evaluated in the transmission system of Figure 8.13 to verify its coverage and robustness. The suitable mother wavelet to this application is identified and the average time requested to this protection offers a correctly fault directionality is

highlighted. In addition, the fault inception angle (θ_f), distance (d_f), and resistance (r_f) effects were evaluated in this system.

6.2.1 The Effect of the Mother Wavelet

A total of 2000 SLG faults (1000 forward and 1000 reverse faults) were simulated with random fault resistance and fault inception angle, whose the parameters details are presented in Table 6.3. Faults were randomly positioned at the remote buses B1 and B2, at local bus B2 and in the line extension far from bus B2 (both lines L1 and L2).

Table 6.3: Data base parameters to evaluate the better mother wavelet.

Parameter	Variation
Fault distance	$20 \leq d_f \leq 180$ km and at bus B1, B2 and B3
Fault inception angle	$0^\circ \leq \theta_f \leq 180^\circ$ ($\Delta\theta_f = 1^\circ$)
Fault resistance	$0.001 \leq r_f \leq 10\ \Omega$
Fault Position	Forward and reverse
Fault type	AG

Mother wavelets of the Doubechies family with 2 (Haar), 4 (db4), 8 (db8), 12 (db12), and 50 (db50) coefficients (short and long wavelets) were used. Combining the units, all SLG faults were correctly diagnosed for any mother wavelet, attesting the robustness of the proposed method. However, the mother wavelet impacts the directional operating time. Table 6.4 summarizes the average time spent to each mother wavelet to detect forward faults.

Table 6.4: Effects of the mother wavelet.

Protection	Directional operating time (ms)				
Units	Haar	db4	db8	db12	db50
67WA	5.7	6.0	6.1	6.1	8.3
67PWA	7.1	8.4	7.2	7.4	9.6
67QWA	15.1	16.3	16.9	17.3	19.7
67NWA	16.4	17.5	18.0	18.3	20.7

It is well-known that the wavelet answer tends to be slower for long wavelets by considering the equations adapted to the real-time analysis due to the filtering processes (COSTA; SOUZA; BRITO, 2012b). Indeed, the fastest diagnosis was provided by the Haar, followed by the db4 wavelet. For instance, Figure 6.2 depicts the directional operating time using the mother wavelets Haar and db50 to an AG forward fault with r_f = 9.88 Ω, d_f = 27.3 km, and θ_f = 26.2°. The directionality was correctly identified in both cases. However, the Haar provided the fastest operating time. The Haar wavelet was selected for the remainder results.

6.2.2 The Effect of the Fault Inception Angle

A total of 3620 faults (including forward and backward faults) were simulated with fixed distance and resistance and varying the fault incidence angle to all fault types, as presented in Table 6.5, in order to verify the fault inception angle influence in both proposed and classical directional protections. Therefore, critical faults for traveling wave-based methods such as AG faults with zero fault inception angle were considered.

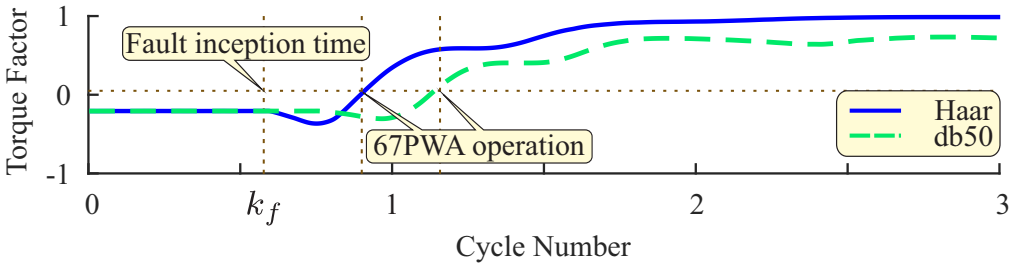

Figure 6.2: 67PWA unit to AG forward fault by using Haar and db50.

Table 6.5: Data base parameters to evaluate the fault inception angle effect.

Parameter	Variation
Fault distance	100 km
Fault inception angle	$0° \leq \theta_f \leq 180°$ ($\Delta\theta_f = 1°$)
Fault resistance	$r_f = 1.0\ \Omega$
Fault Position	Forward and reverse
Fault type	AG, BG, CG, ABG, BCG, CAG, AB, BC, CA, ABC

Tables 6.6 and 6.7 present the success rates (%) of the wavelet- and Fourier-based methods, respectively, as well as the average directional operating time (ms) for forward faults.

According to Tables 6.6 and 6.7, both wavelet- and Fourier-based directional protections provided 100% of success rate to all selected protection units. Although the wavelet trigger being susceptible to low fault inception angle, the scaling coefficients energy is not affected by the fault inception angle. Therefore, the wavelet overcurrent trigger could assure the directional activation in these specific cases with a small delay equivalent to the Fourier-based overcurrent activator.

Table 6.6: The fault inception angle influence (proposed method).

Protection Units	The proposed method performance									
	AG	BG	CG	ABG	BCG	CAG	AB	BC	CA	ABC
67WA (%)	100	-	-	100	-	100	100	-	100	100
67WB (%)	-	100	-	100	100	-	100	100	-	100
67WC (%)	-	-	100	-	100	100	-	100	100	100
Time (ms)	5.0	5.0	5.0	4.1	4.0	4.0	4.1	4.0	4.1	3.6
67PWA (%)	100	100	100	100	-	100	100	-	100	100
67PWB (%)	100	100	100	100	100	-	100	100	-	100
67PWC (%)	100	100	100	-	100	100	-	100	100	100
Time (ms)	5.6	5.6	5.6	7.2	7.2	7.2	7.6	7.6	7.6	8.3
67QWA (%)	100	100	100	100	-	100	100	-	100	100
67QWB (%)	100	100	100	100	100	-	100	100	-	100
67QWC (%)	100	100	100	-	100	100	-	100	100	100
Time (ms)	12.6	12.6	12.6	23.4	23.4	23.4	15.8	15.8	15.8	4.9
67NW (%)	100	100	100	100	100	100	-	-	-	-
Time (ms)	14.5	14.6	14.6	13.9	13.9	13.9	-	-	-	-
Global(%)	100	100	100	100	100	100	100	100	100	100
Time (ms)	5.0	5.0	5.0	4.0	4.1	4.0	4.1	4.0	4.0	3.6

Regarding the directional operating time:

Table 6.7: The fault inception angle influence (conventional method).

Protection	The Fourier method performance									
Units	AG	BG	CG	ABG	BCG	CAG	AB	BC	CA	ABC
67A (%)	100	-	-	100	-	100	100	-	100	100
67B (%)	-	100	-	100	100	-	100	100	-	100
67C (%)	-	-	100	-	100	100	-	100	100	100
Time (ms)	18.9	19.1	18.8	10.1	10.1	10.8	10.3	10.1	10.1	10.6
67P (%)	100	100	100	100	100	100	37.1	37.0	37.1	100
Time (ms)	18.9	19.0	18.8	10.7	10.7	10.8	10.3	10.1	10.1	8.8
67Q (%)	100	100	100	100	100	100	100	100	100	-
Time (ms)	10.8	11.0	11.0	10.2	10.1	10.1	10.2	10.0	10.1	-
67N (%)	100	100	100	100	100	100	-	-	-	-
Time (ms)	11.6	11.3	11.2	11.9	12.1	11.9	-	-	-	-
Global(%)	100	100	100	100	100	100	100	100	100	100
Time (ms)	10.8	11.0	11.0	10.2	10.1	10.1	10.2	10.0	10.1	8.8

- The wavelet-based phase (67WA, 67WB, and 67WC) and positive (67PWA, 67PWB, and 67PWC) units provided faster results than Fourier-based phase (67A, 67B, and 67C) and positive (67P) units, respectively.
- Both wavelet-based negative and zero sequence units (67QWA, 67QWB, 67QWC, and 67NW) were slightly slower than the related conventional units (67Q and 67N).
- The 67NW and 67N units are not available to LL and ABC faults.

Since the trip is an OR combination of all units, the proposed method was the fastest in all types of faults, pointed in the last line of Tables 6.6 and 6.7 (Global time).

6.2.3 The Effect of the Fault Distance

The fault distance affects the directional protection performance because a high line impedance between the fault and relay can slow up the overcurrent activators. All fault types with distance variation to both forward and backward fault locations with fixed fault inception angle and fault resistance were simulated (3220 faults) in order to evaluate the fault distance influence, the fault parameters are presented in Table 6.8.

Table 6.8: Data base parameters to evaluate the fault distance effect.

Parameter	Variation
Fault distance	$20 \leq d_f \leq 180$ km ($\Delta d_f = 1$ km)
Fault inception angle	$\theta_f = 45^\circ$
Fault resistance	$r_f = 1.0\ \Omega$
Fault Position	Forward and reverse
Fault type	AG, BG, CG, ABG, BCG, CAG, AB, BC, CA and ABC

Both methods presented 100% of success rate, even in the critical fault distances far from the relay position (e.g., $d_f = 180$ km). However, the Fourier-based method failed in some units. In addition, the proposed method was the fastest. For instance, Figure 6.3 depicts with more details the success rate and the average of the directional operating time for ABG faults obtained with the wavelet- and Fourier-based methods as well as the directional operating time as a function of the fault distance. The units 67WA and 67PWA were faster than 67A and 67P,

respectively, whereas 67QWA and 67NW were slower than 67Q and 67N, respectively. Since the directionality considers the unit combination, the proposed wavelet-based method was the fastest. The conventional 67P unit failed in few cases (the directional operating time with null value in Figure 6.3(c)) due to the insufficient fault overcurrent to trigger such a unit, whereas the wavelet trigger could activate the wavelet directionality properly.

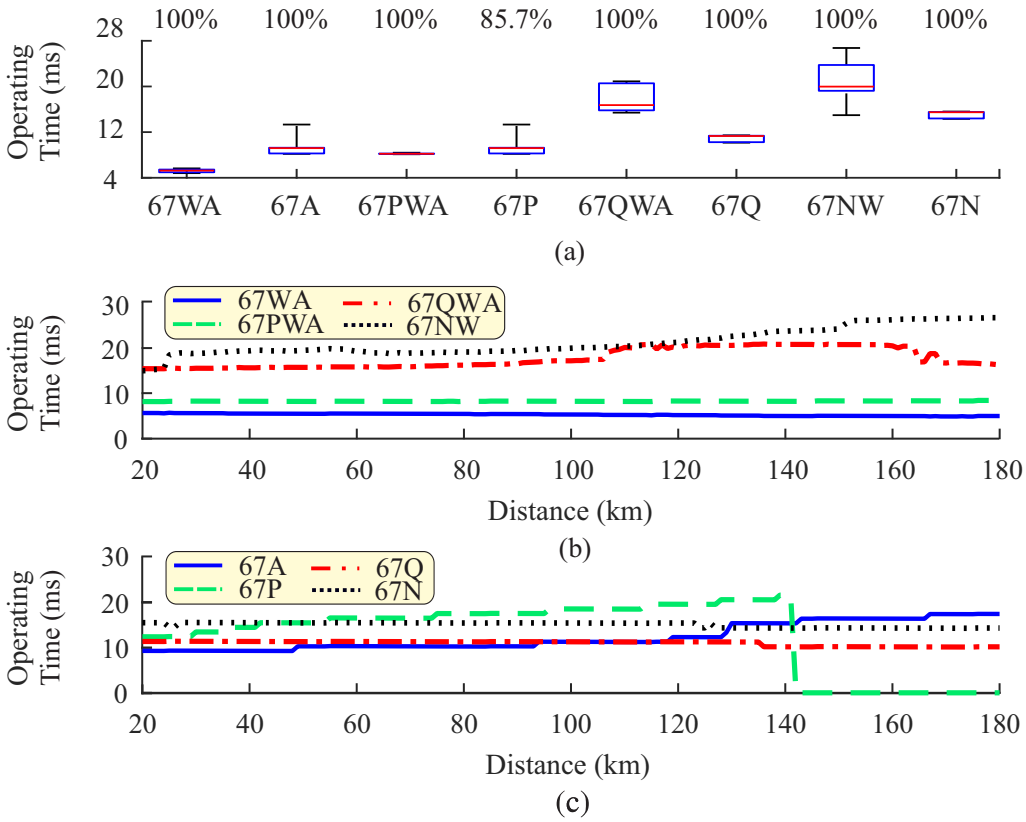

Figure 6.3: Directional operating time of wavelet- and Fourier-based protections under fault distance influence to ABG faults.

In order to evaluated the distance effect, the simulations considered a distance starting from 20 km to 180 km. This range can be higher by increasing the simulation sampling frequency to be closer to the real analogical signal, for instance. However, since faults on buses (the closest and farthest faults were considered) as well as several faults from 20 km of the relay were considered, the performance evaluation of the methods could be properly verified. Figure 6.4 depicts the results to a forward AG fault with $d_f = 1$ km far from the bus B2, with $\theta_f = 45°$ and $r_f = 1\ \Omega$. The simulation sampling frequency was increased by 20 times ($f_s = 307200$ Hz) to achieve a time step small enough to be possible to simulate it and then it was sampling again to $f_s = 307200$ Hz used in the method. In accordance with the previous results the general performance is also present in this case.

6.2.4 The Effect of the Fault Resistance

The highest the fault resistance the lowest the fault current, which means that directional protection units tend to be unsensitized by overcurrent activators and the relay operating time tends to be higher. In order to verify this issue, 2200 faults were simulated (forward and backward faults) considering all fault types, varing the fault resistance and fixing the fault distance

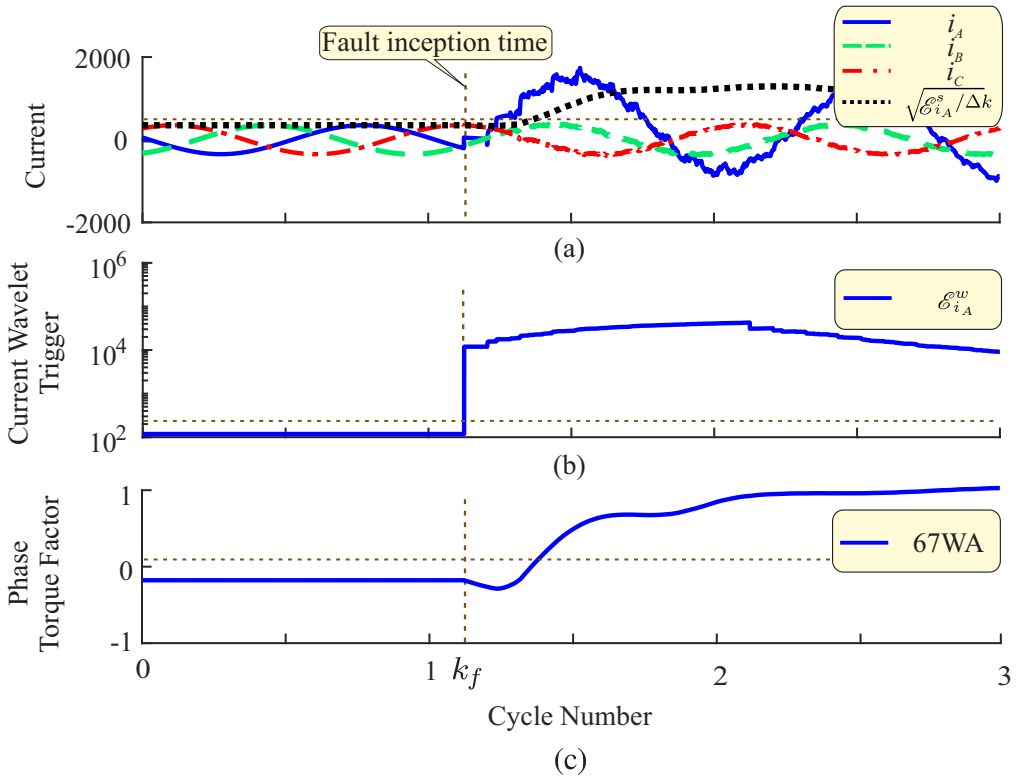

Figure 6.4: Forward AG fault: (a) three-phase currents; (b) wavelet coefficient energies (wavelet trigger); (c) wavelet phase torque factors.

and fault inception, as presented in Table 6.9.

Table 6.9: Data base parameters to evaluate fault resitance effect.

Parameter	Variation
Fault distance	$d_f = 100$ km
Fault inception angle	$\theta_f = 45°$
Fault resistance	$0.001 \leq r_f \leq 100.0\ \Omega$ ($\Delta r_f = 1.0\ \Omega$)
Fault Position	Forward and reverse
Fault type	AG, BG, CG, ABG, BCG, CAG, AB, BC, CA and ABC

The Fourier-based method presented a success rate of 98.37% considering the combination of all units, and a mean directional operating time of 10.2 ms. Regarding the wavelet-based method, a success rate of 100% and a mean directional operating time of 5.15 ms were obtained. The performance by unit was strongly affected by the fault resistance only with the classical method because the proposed method is also activated by additional wavelet activators.

Figure 6.5 depicts the average of the directional operating time for ABG faults obtained with the proposed and Fourier-based methods and the success rate by unit. The directional operating time as a function of the fault resistance is also shown in Figure 6.5. The Fourier-based phase (67A) and positive sequence (67P) units were quite influenced by the fault resistance (e.g., the directional operating time with null value in Figure6.5(c) indicates no directional activation), whereas the sensitive units 67Q and 67N were less affected. Conversely, all wavelet-based units were not affected by the fault resistance.

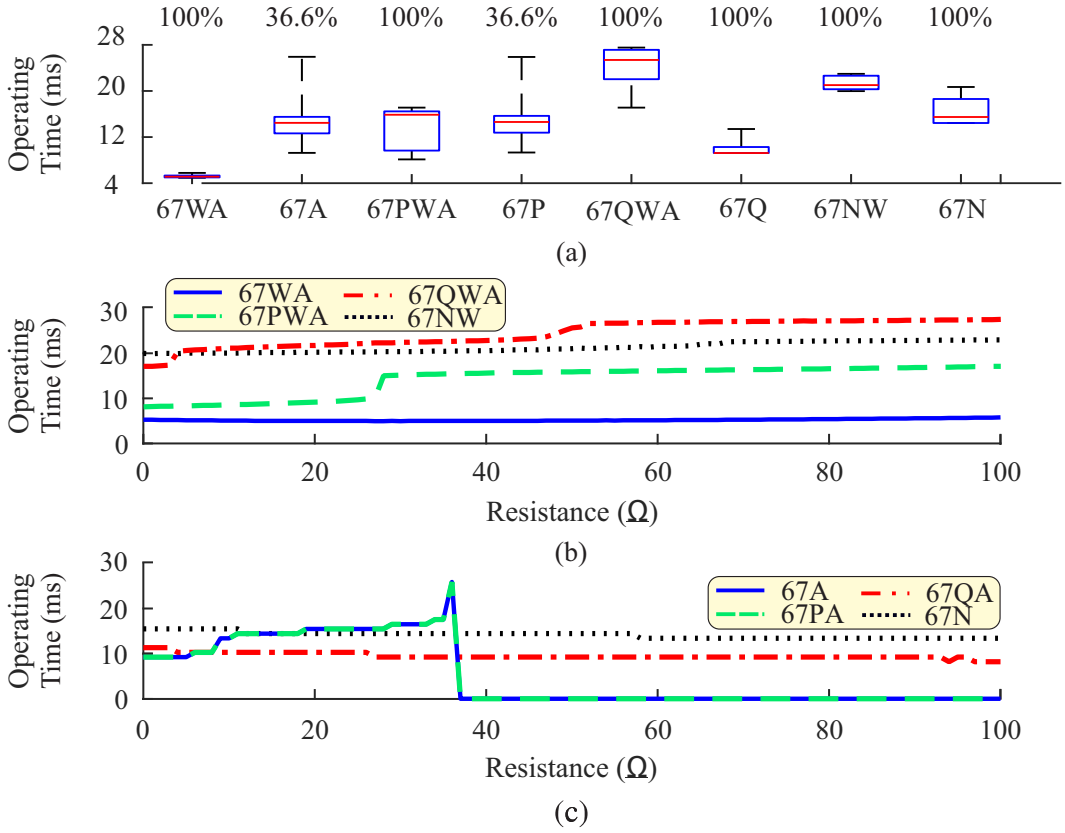

Figure 6.5: Directional operating time of Wavelet- and Fourier-based protections under fault resistance influence to ABG faults.

6.2.5 A Critical Case

The previous evaluations of the influence of fault inception angle, resistance, and distance in the directional protections included critical cases associated to each parameter. However, Figure 6.6 depicts an AG fault with the combination of various critical fault parameters ($\theta_f = 0°$, $r_f = 100\ \Omega$, and $d_f = 180$ km).

An AG fault with fault inception angle near zero degree results in overdamped transients. Therefore, the wavelet activators could not enable the proposed wavelet-based directional protection. Both the conventional overcurrent and the wavelet-based overcurrent activators also could not enable any directional protection unit due to high values of fault resistance and distance (no overcurrents). Therefore, neither conventional nor wavelet-based directional protections could be activated in this critical fault.

Despite of any directional unit be enabled by overcurrent activators, the sensible negative- and zero-sequence directional units could properly identify the fault directionality (both conventional and wavelet-based units) such as shown in Figures 6.6(b) and (c). The other directional units did not provide the fault direction (neither forward nor backward), and no false trip was issued. Therefore, the directional protection is reliable even in critical situations for the overcurrent protection.

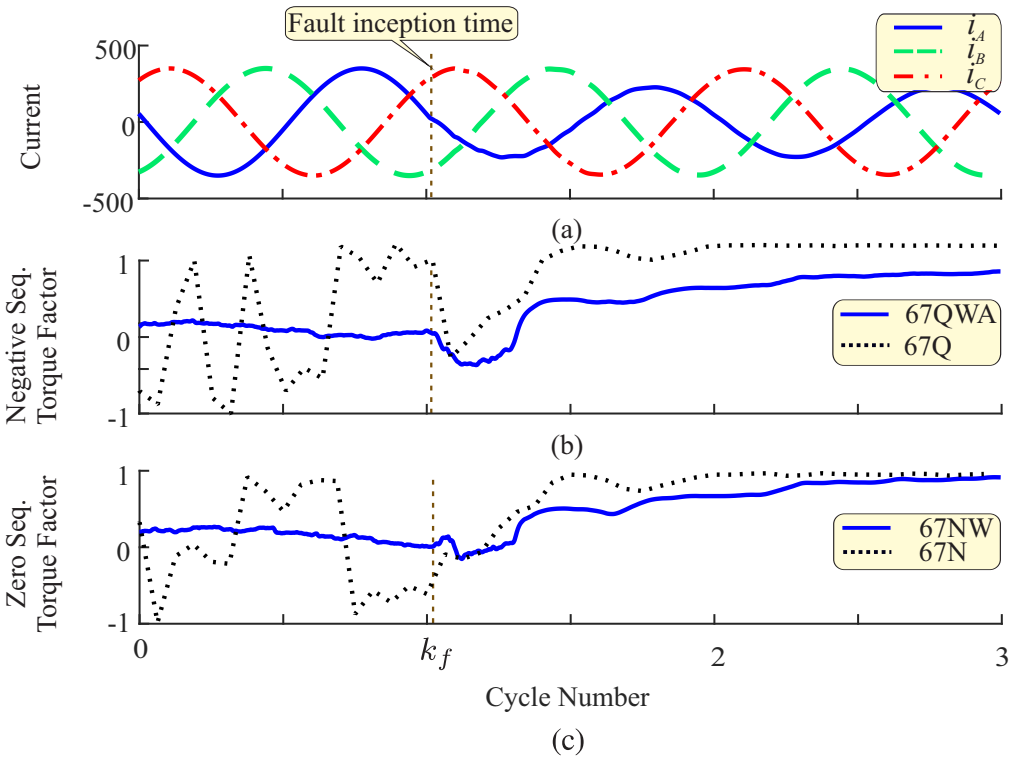

Figure 6.6: AG forward fault: (a) phase currents; (b) Fourier and wavelet-based negative sequence torque factor; (c) Fourier and wavelet-based zero sequence torque factor.

6.2.6 The Effect of the Noise

The wavelet-activators evaluate high-frequency components of voltages and currents, and may face problems to enable the directional protection in the case of overdamped fault-induced transients in signals with very-low SNR. Conversely, the proposed overcurrent activators and torque factors are computed by using low-frequencies extracted through the scaling coefficients which are not expected to be affected by the SNR.

The noise effects in the proposed method are illustrated considering a forward BG fault with $d_f = 57$ km, $\theta_f = 48°$, and $r_f = 56\ \Omega$ with two extreme noise levels: SNR=20 and 60 dB. The results are presented in Figure 6.7. In this case, the fault-induced transients were not severe ($r_f = 56\ \Omega$). Therefore, the wavelet-based activators were affected by the noise, and did not activate the directional elements when the SNR was 20 dB (Figure 6.7(a)). Conversely, the wavelet-based overcurrent activator was not affected by the noise, activating the directional protection functions (Figure 6.7(b)). In addition, the identification of the fault directionality was not affected by the noise too (Figure 6.7(c)). Nevertheless, the replacement of the RT-SWT by the RT-BSWT can reduce the influence of the noise in the wavelet activator.

6.2.7 Negative Sequence Unit in Three-Phase Faults

It is well-known that the conventional negative sequence unit 67Q is not used to evaluate balanced faults. Conversely, according to Table 6.6, the proposed 67QW unit could properly detect the directionality and 100% of success rate was obtained in three-phase faults. In addition, the 67QW unit could be faster than most of the protection units in these faults.

When a three-phase fault is detected, the proposed 67QW unit (67QWA, 67QWB, and

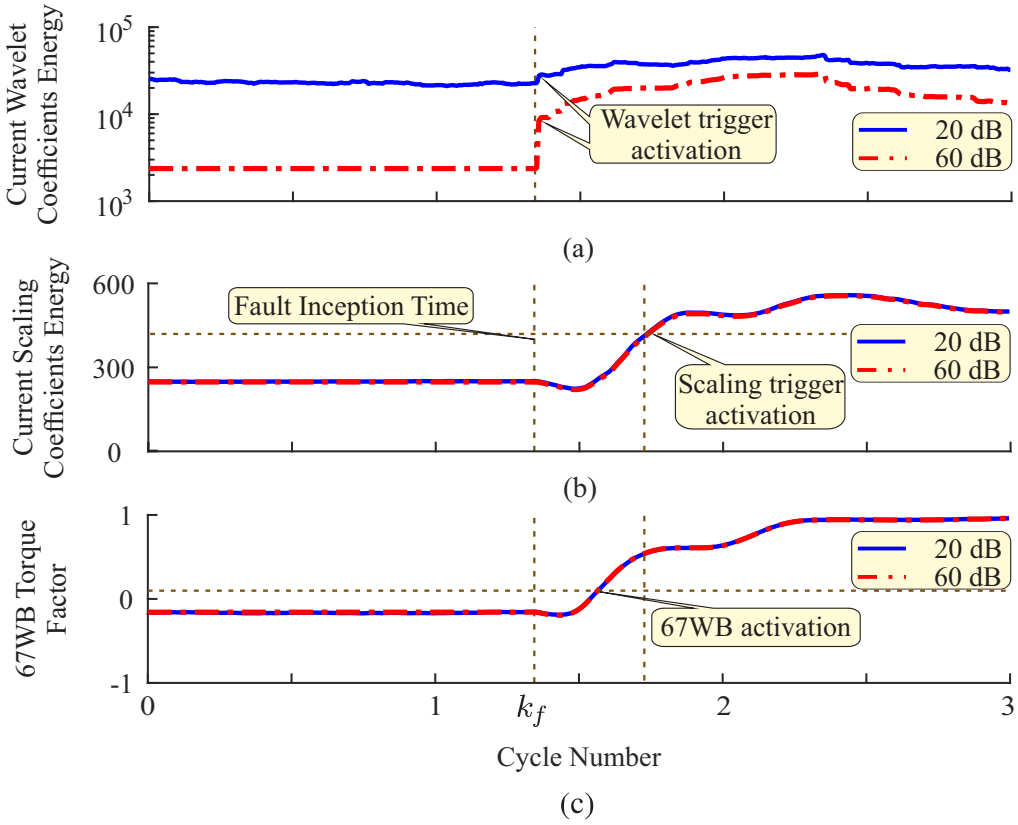

Figure 6.7: Noise effects: (a) wavelet coefficient energy of phase-B current (wavelet activator); (b) normalized scaling coefficient energy of phase-B current (wavelet-based overcurrent activator); (b) wavelet-based phase-B torque factor (67WB).

67QWC) evaluates whether at least two of three torque factors present magnitude higher than the threshold in order to detect a forward fault. Only the first cycle is evaluated by the 67QW unit in three-phase faults. For instance, Figure 6.8 depicts the scaling torque factor to ABC forward and reverse faults with d_f = 100 km, θ_f = 80°, and r_f = 1.0 Ω. As expected, only the forward fault was detected through the 67WQ unit during the first cycle from the fault, whereas the conventional 67Q unit could not identify the forward fault.

6.2.8 Hard Voltage Sags in Three-Phase Faults

A classical issue to the directionality is a three-phase fault with voltage sags close to zero. This situation leads to a unreliable voltage reference for the protection logic and hence the directionality can not be accurate. Conversely, the proposed 67QW unit can still be effective in these cases. For instance, Figure 6.9 depicts the voltage sag caused by a severe reverse ABC fault with $\theta_f = 0°$, $d_f = 0$ km and $r_f = 0.09$ Ω as well as the scaling coefficient energy of phase voltages ($\mathcal{E}^s_{v_A}$, $\mathcal{E}^s_{v_B}$, and $\mathcal{E}^s_{v_C}$) and the 67QW units. The 67QW units properly indicated a reverse fault in Figure 6.9 (c) (at least two units under the threshold during the first cycle of fault).

The energies $\mathcal{E}^s_{v_A}$, $\mathcal{E}^s_{v_B}$, and $\mathcal{E}^s_{v_C}$ can be used for voltage sag detection (COSTA; DRIESEN, 2013) [Figure 6.9 (b)]. Therefore, if a three-phase fault is detected the 67QW units are enabled during one cycle as aforementioned. In addition, if a hard voltage sag is detected through $\mathcal{E}^s_{v_A}$, $\mathcal{E}^s_{v_B}$, and $\mathcal{E}^s_{v_C}$, other units (67W, 67PW, and 67NW) are blocked to assure the correct directionality.

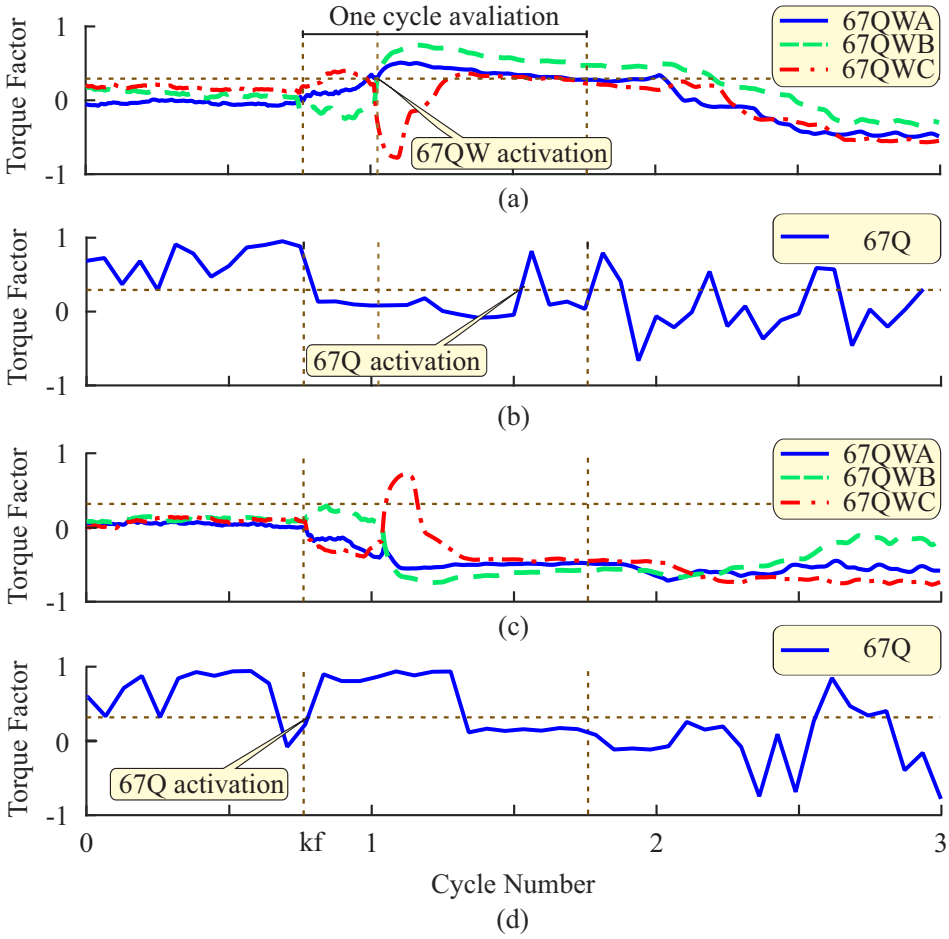

Figure 6.8: ABC fault: (a) 67QW units to a forward fault; (a) 67Q units to a forward fault; (a) 67QW units to a reverse fault; (b) 67Q unit to a reverse fault.

In order to evaluate the proposed wavelet-based directional protection under severe voltage sags, 4000 three-phase faults (forward and reverse) were simulated with $\theta_f = 0°$, $d_f = 0$ km and $0 \leq r_f \leq 100\ \Omega$. As expected, only the proposed 67QW provided 100% of success rate with mean directional operating time of 4.8 ms. Conversely, Fourier-based units (67 and 67P) and other wavelet-based units (67W and 67PW) offered false trips.

Memory Strategy

The Fourier-based method solves the voltage reference problem by storing some voltage cycles to be used as reference when the voltage collapses under a specific threshold (ROBERTS; HOU, 1998). In the same fashion, the memory strategy can also be used by the wavelet-based method. Therefore, considering the memory strategy the Fourier- and wavelet-based methods (67, 67P, 67W, and 67PW) presented both 100% of success rate with mean operating time of 7.3 and 7.6 ms, respectively. However, as a novelty, the proposed method can identify this fault types without implement this strategy and provide a mean directional operating time of 4.8 ms as aforementioned.

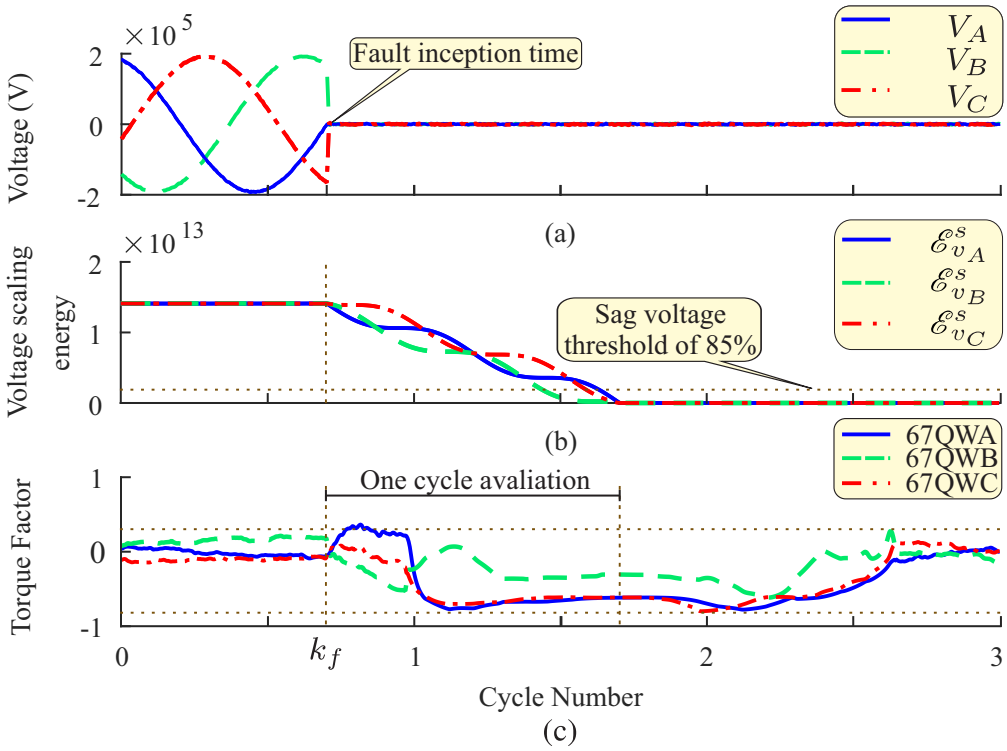

Figure 6.9: ABC reverse fault: (a) ABC voltages; (b) ABC phase voltage scaling energy; (c) torque factor to the proposed method.

6.2.9 Computational Burden

The wavelet-based directional protection was implemented in a floating-point Digital Signal Processor (DSP) TMS230F28335 in order to verify its applicability in a real protection application. The computational burden to all units, per sampling, was about 54.2 μs $<$ 65.1 μs $(1/f_s)$, which prove that the proposed method is feasible using such sampling frequency. The Fourier-based method was also implemented in the same DSP, using the recursive DFT, which spent 62.6 μs, per sampling, to process all the calculus.

6.2.10 Capacitor Switching Effect

Apart from faults, the proposed wavelet-based activators can be sensitized with transients induced by switching events such as capacitor switching. However, the proposed wavelet-based directional elements are in accordance with the conventional directional elements, and may be robust under non-fault situations. For instance, Figure 6.10 presents the performance of both the proposed and Fourier-based methods when a capacitor bank of 50 MVar is switched with inception angle of 30° at the remote bus B1 (Figure 8.1).

A capacitor switching usually produces hard voltage and current transients at the switching time, which are damped in few cycles (Figure 6.10). Therefore, as expected, the wavelet-based activators detected this switching and enabled the proposed wavelet-based directional elements (Figure 6.10(b)). This is not an issue because the wavelet-based directional functions are in accordance with the conventional protection which were designed to present a relevant torque during fault situations. For instance, the wavelet-based positive sequence torque factors in Figure 6.10(c) did not present values higher than forward thresholds, and no directional trip

was issued.

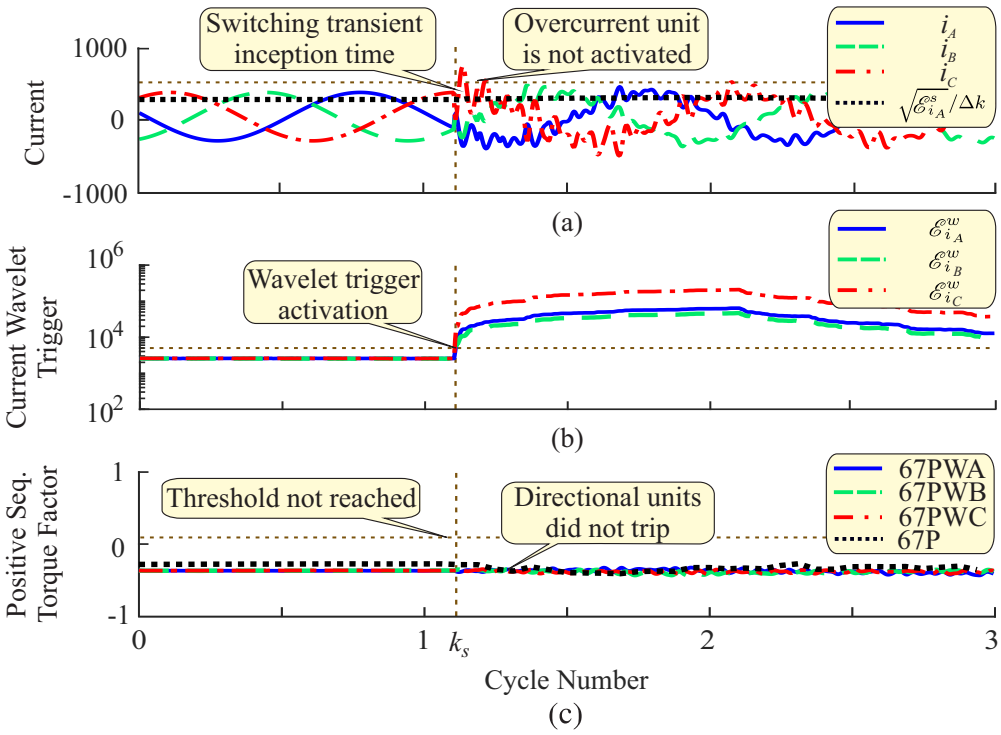

Figure 6.10: Forward capacitor switching: (a) three-phase currents; (b) wavelet coefficient energies of the phase-A current (wavelet trigger); (c) wavelet and Fourier-based positive sequence torque factors.

Considering the worst case in which the directional protection issued a trigger, which is not expected for this type of switching, the final trip would not be issued because the overcurrent function would not trigger. For instance, the current magnitudes are not enough to sensitize the overcurrent protection in Figure 6.10(a). The same performance is expected to other switching transient events. Regarding a lightning, if the arcing result in a fault the directional overcurrent functions will probably trip.

6.2.11 Fault Classifier

By evaluating the proposed directional protection in the transmission system, the faster time achieved by this protection was around five milliseconds. Therefore, a fault classifier was required in order to support the proposed method. A methodology based on wavelet and Clarke transform was developed and detailed in the next chapter. The proposed fault classifier is enough to support the proposed directional protection once its average time is around 2.1 milliseconds.

6.2.12 Distribution System with Distributed Generation

Distribution systems with distributed generation (DG) are challenging scenarios for the overcurrent directional protection due to the fault current level changes and complex power flow. The challenge is higher when this scenario is combined with high resistance faults. The IEEE 30 bus test system with a distribution system at 33 kV and a sub-transmission system at

132 kV (COSTA; MONTI; PAIVA, 2017) was simulated in the Matlab Simulink. Three doubly-fed induction generator (DFIG) (ABU-RUB; MALINOWSKI; AL-HADDAD, 2014) with 4.0 MVA were included as DG in order to evaluate the performance of the proposed and conventional methods in some case studies. The additional details about the 30 bus system and the DFIG used are described in the Appendix A.

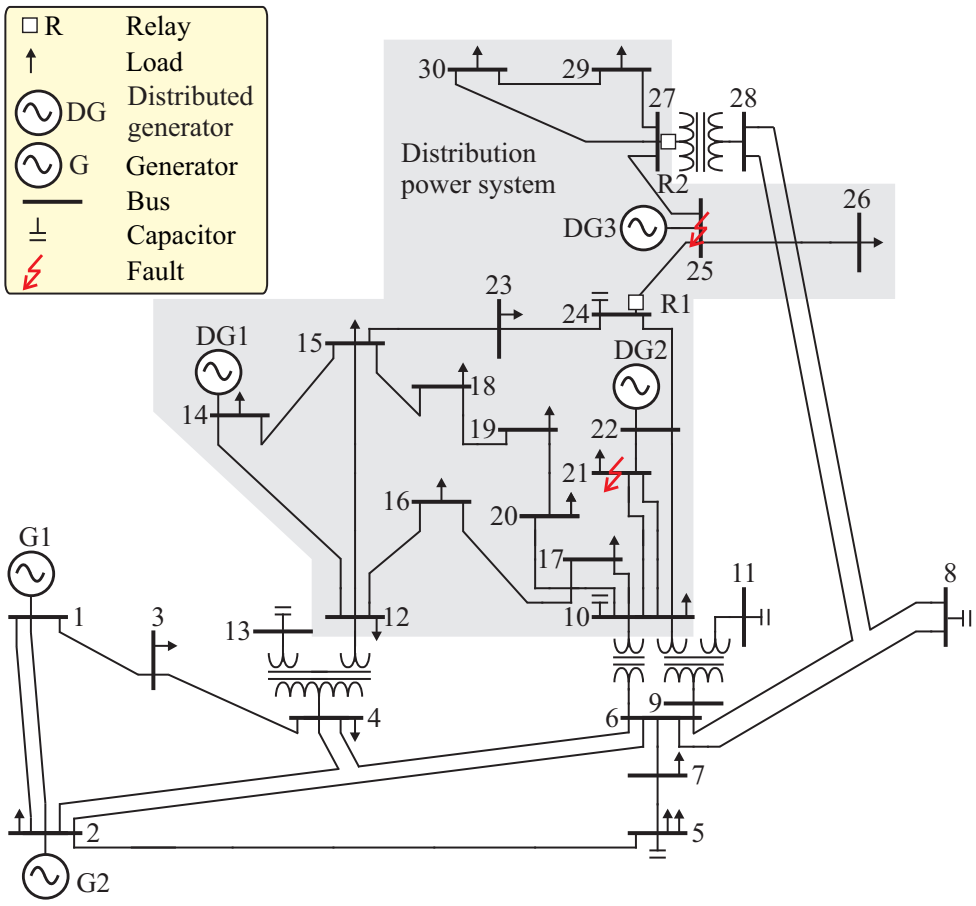

Figure 6.11: IEEE 30 bus test system with distributed generation.

AG faults with $r_f = 1$ and 100 Ω (low and high resistance faults, respectively) and $\theta_f = 90°$ were simulated at the bus 25 (d_f = 6.11 km) with the protected relay located at the bus 24 (forward fault). Some results to the faults with $r_f = 1$ and 100 Ω are shown in Figures 6.12 and 6.13, respectively.

Regarding the fault with $r_f = 1$ Ω, the overcurrent functions properly enabled the related directional protection units in both wavelet- and Fourier-based methods, and the fault direction could be identified successfully in this case study by all units. For instance, the zero-sequence torque factors shown in Figure 6.12(c) indicated the forward fault.

Regarding the distribution system with distributed generation combined to high-resistance fault, the fault did not present a relevant overcurrent to activate the directional units. Therefore, no directional unit was activated by the overcurrent triggering criteria in both proposed and conventional directional protections. Nevertheless, the wavelet triggers could activate the proposed directional units (Figure 6.13(b)), and the directional protection trigger was issued by the proposed method, such as the wavelet-based zero-sequence torque factor shown in Figure 6.13(c) which could properly indicate the fault direction.

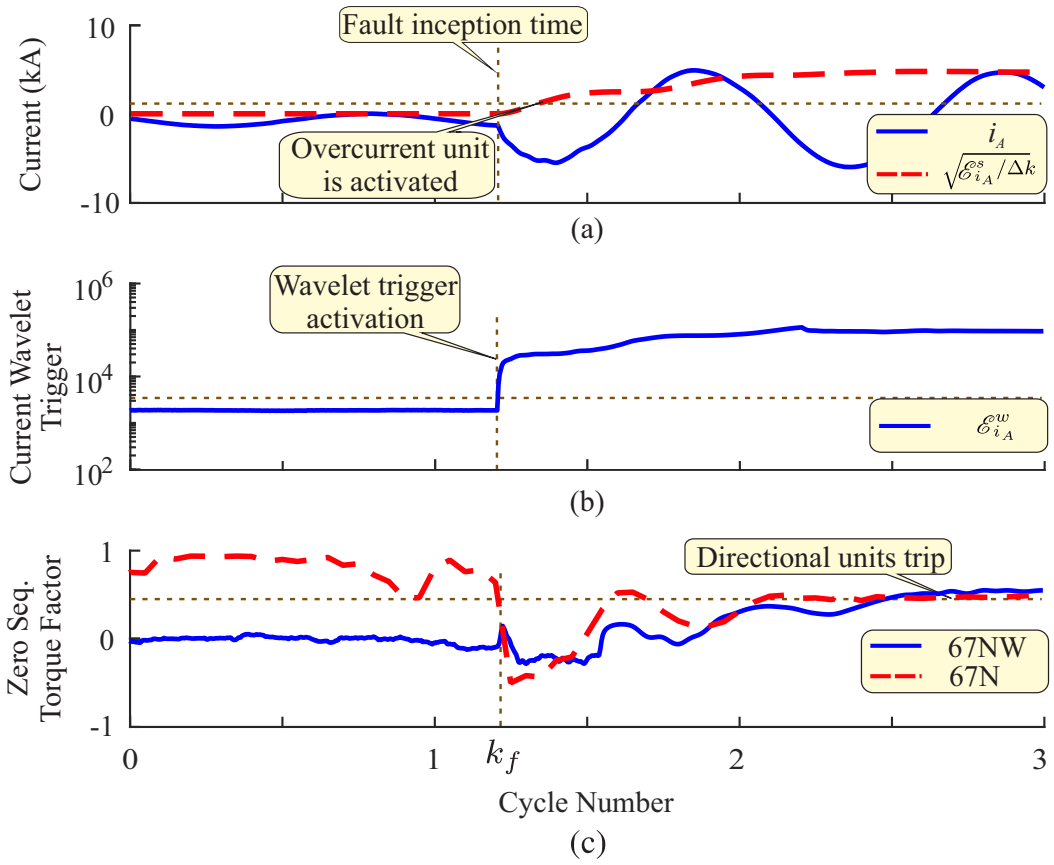

Figure 6.12: AG fault in the IEEE 30 bus test system ($r_f = 1\ \Omega$): (a) phase-A current and the related normalized scaling coefficient energy (overcurrent trigger); (b) wavelet coefficient energy of i_A (wavelet trigger); (c) wavelet and Fourier zero-sequence torque factors.

The final trip is usually a composition of the directional protection trigger and the overcurrent protection trigger in this kind of power system. Only the proposed directional protection issued a trip in the case of $r_f = 100\ \Omega$, as aforementioned. However, the overcurrent trip would not be possible in this example due to the low fault overcurrent. Therefore, improvements in the overcurrent protection such as adaptive thresholds or the proposal of more sensitized protection functions to support the directional protection would be possible solutions in order to deal with the protection of distribution system with DG. However, this is out of scope of this thesis, which focuses only the directional protection.

In order to deep evaluate the proposed method in distribution systems with DGs, seven DGs were added into the system presented in Figure 6.11, at buses 19, 16, 15, 30, 29, 23 and 26, and the measured points were maintained at buses 24 and 27. Faults were performed at buses 21 and 25 with $r_f = 1\ \Omega$ and $r_f = 100\ \Omega$ to AG fault type.

Figures 6.14 and 6.15 present the results to faults with $r_f = 1\ \Omega$ and $r_f = 1\ \Omega$, respectively. The currents seen by the relay are presented and two directional units are illustrated to both forward and backward faults. According to Figures 6.14(c)-(f), the directionality worked properly to the phase and negative sequence units. Although the other units were not illustrated, they worked properly as well. However, with a higher fault resistance $r_f = 100\ \Omega$, the phase unit did not recognize the power flow modification (Figures 6.15(c) and (d)). The negative sequence (Figure 6.15(f)) and zero sequence units worked correctly recognizing the system directionality. In both presented cases, even a directional protection offering a reliable directionality the units

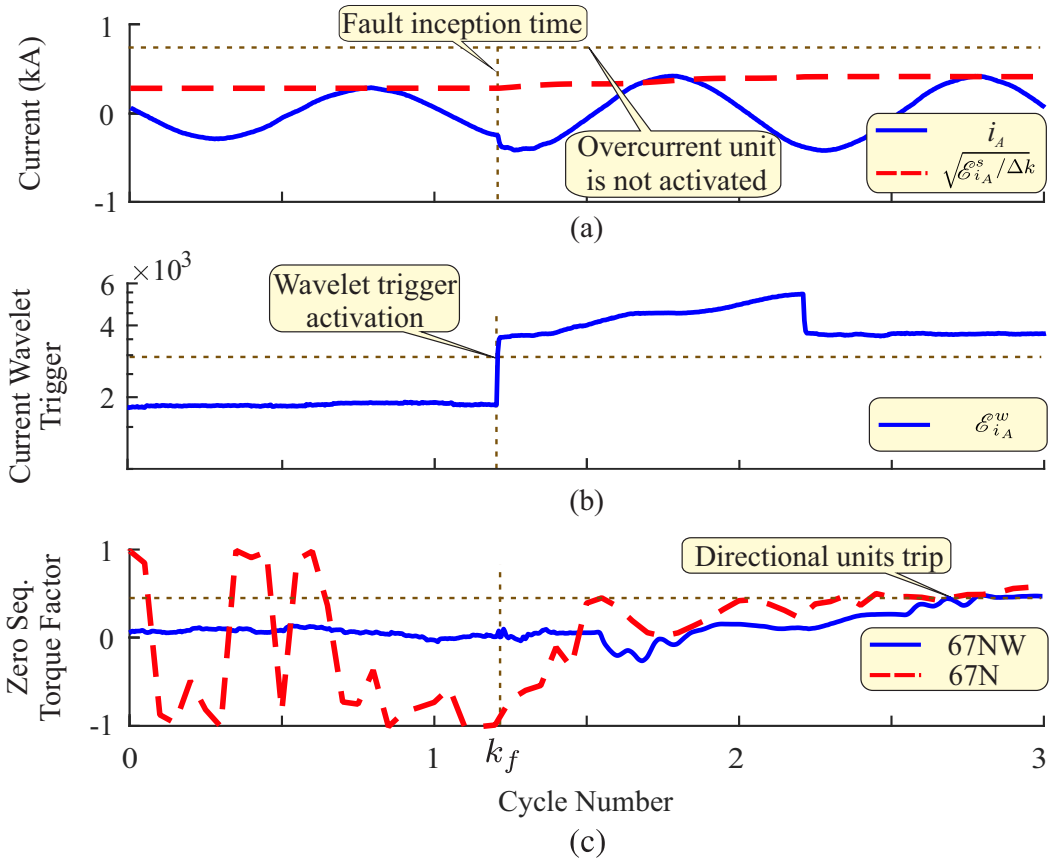

Figure 6.13: AG fault in the IEEE 30 bus test system ($r_f = 100\ \Omega$): (a) phase-A current and the related normalized scaling coefficient energy (overcurrent trigger); (b) wavelet coefficient energy of i_A (wavelet trigger); (c) wavelet and Fourier zero-sequence torque factors.

will not be activated due to the low overcurrent present in the system.

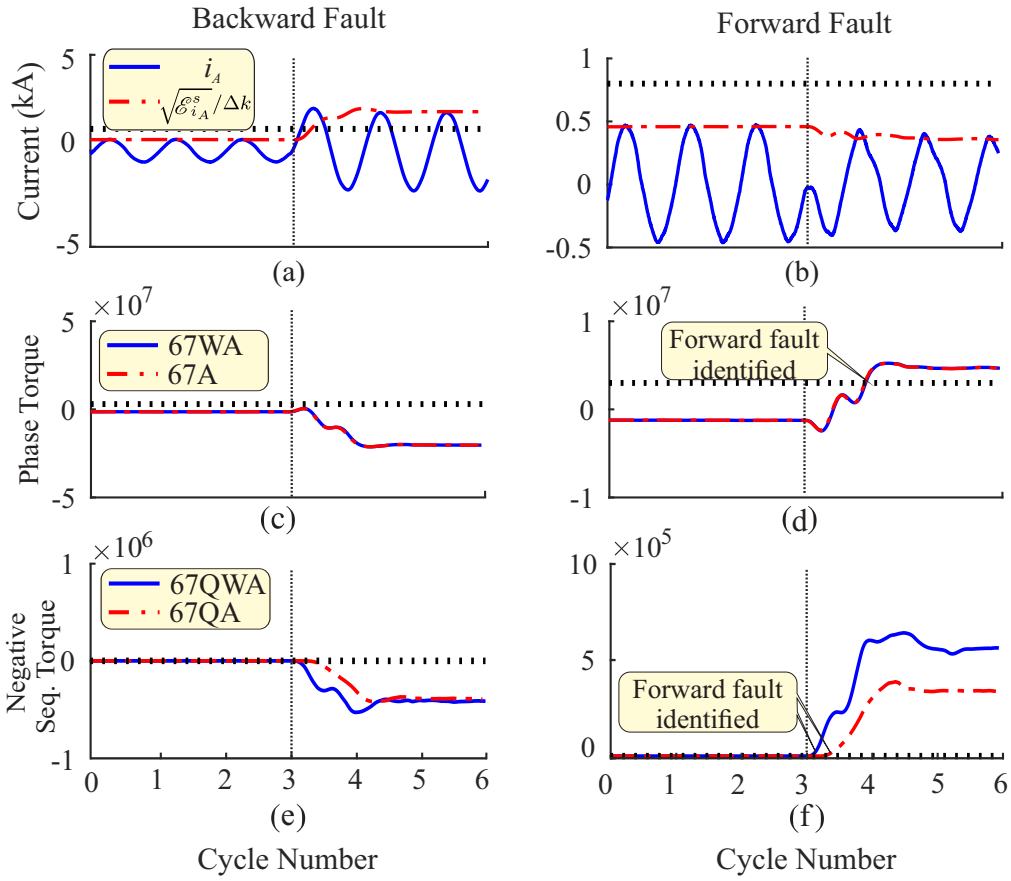

Figure 6.14: AG fault with 10 DFIG and $r_f = 1\Omega$: a) phase A current to backward fault; b) phase A current to forward fault; (c) and (d) Fourier and wavelet-based phase A torque to backward and forward fault, respectively; (e) and (f) Fourier and wavelet-based negative sequence torque to backward and forward fault, respectively

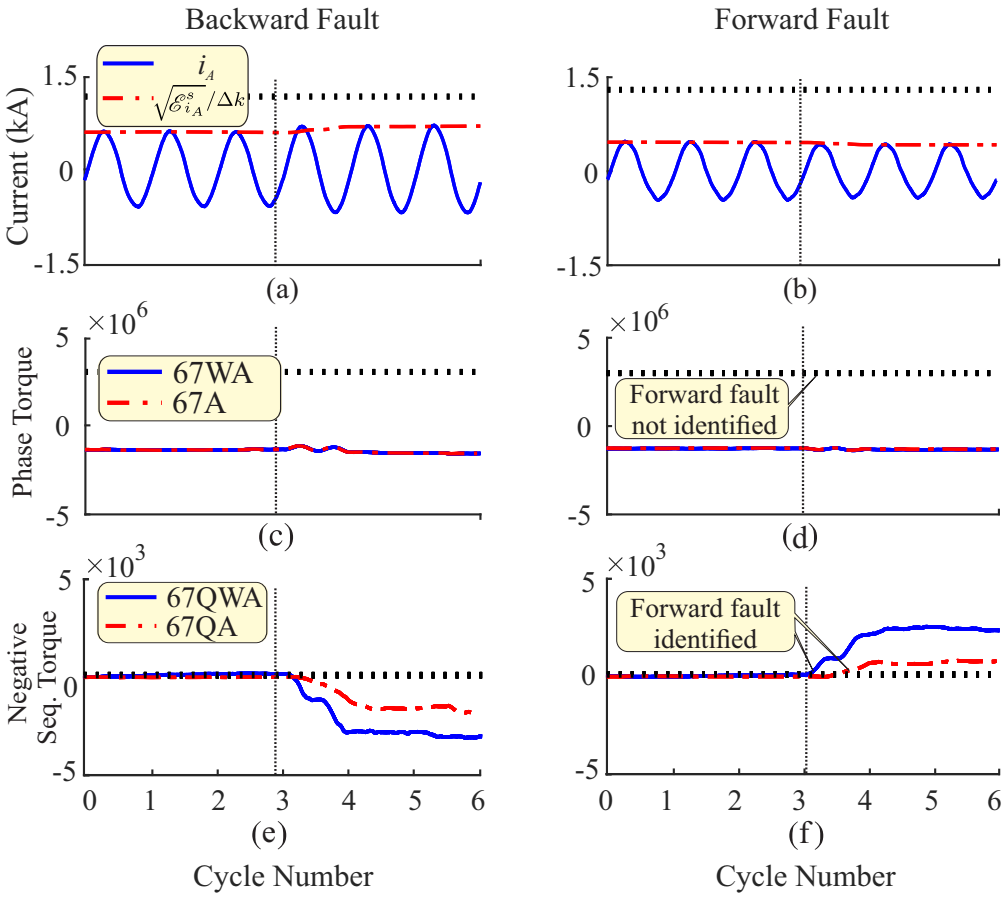

Figure 6.15: AG fault with 10 DFIG and r_f = 1Ω: (a) phase A current to backward fault; (b) phase A current to forward fault; (c) e (d) Fourier and wavelet-based phase A torque to backward and forward fault, respectively; (e) e (f) Fourier and wavelet-based negative sequence torque to backward and forward fault, respectively

6.3 Summary

In this chapter, a wavelet-based version of the classical directional protection was proposed and compared to the classical directional protection based on the Fourier transformer. The proposed directional protection was less influenced by the evaluated fault parameters and provided 100% of success rate with the best operating time to the analyzed faults. In addition, the wavelet-based negative sequence units presented a reliable and fast directionality to ABC faults, even under severe voltage sags. The proposed method achieved good results when applied in a distribution system with distributed generation. Also, the proposed method was implemented in a hardware and presented the lowest computational burden.

Chapter 7

The Proposed Wavelet-Based Fault Classifier Method

In this chapter a transmission line fault classification method based on the real-time BSWT and the Clarke transform is presented. The three phase currents at the local bus are required in order to compute Clarke transformation which is used as the inputs to the RT-BSWT providing the wavelet coefficients from alpha, beta and zero. Therefore, the energy of the wavelet coefficients in the modal domain are calculated and normalized to be compared with fixed thresholds to be effective in any transmission line.

7.1 Clarke-Wavelet Energy Components

By using (3.52) with α- and 0-mode components, the first level Clarke-wavelet coefficient energies, termed as α- and 0-mode energies $\mathscr{E}^{w}_{i_{\alpha A}}, \mathscr{E}^{w}_{i_{\alpha B}}, \mathscr{E}^{w}_{i_{\alpha C}}, \mathscr{E}^{w}_{i_0}$, are given by:

$$\mathscr{E}^{w}_{i_{\alpha A}}(k) = \sum_{l=1}^{L-1} [w_{i_{\alpha A}}(l,k)]^2 + \sum_{n=k-\Delta k+L}^{k} [w_{i_{\alpha A}}(n)]^2, \tag{7.1}$$

$$\mathscr{E}^{w}_{i_{\alpha B}} = \sum_{l=1}^{L-1} [w_{i_{\alpha B}}(l,k)]^2 + \sum_{n=k-\Delta k+L}^{k} [w_{i_{\alpha B}}(n)]^2, \tag{7.2}$$

$$\mathscr{E}^{w}_{i_{\alpha C}}(k) = \sum_{l=1}^{L-1} [w_{i_{\alpha C}}(l,k)]^2 + \sum_{n=k-\Delta k+L}^{k} [w^2_{i_{\alpha C}}(n)]^2 \tag{7.3}$$

and

$$\mathscr{E}^{w}_{i_0}(k) = \sum_{l=1}^{L-1} [w_{i_0}(l,k)]^2 + \sum_{n=k-\Delta k+L}^{k} [w_{i_0}(n)]^2. \tag{7.4}$$

where $w_{i_{\alpha A}}, w_{i_{\alpha B}}, w_{i_{\alpha C}}$ and $^{w}_{i_0}$ are the wavelet coefficients to α-mode with A, B, C references and 0-mode, respectively. An equivalent approach could be done by using only β components.

The total α-mode energy, termed as base energy, per sampling time, is given by:

$$\mathscr{E}^{w}_{base}(k) = \mathscr{E}^{w}_{i_{\alpha_A}}(k) + \mathscr{E}^{w}_{i_{\alpha_B}}(k) + \mathscr{E}^{w}_{i_{\alpha_C}}(k). \tag{7.5}$$

Therefore, normalized alpha- and zero-energies are given by:

$$\mathscr{E}^{\alpha}_{A}(k) = \mathscr{E}^{w}_{i_{\alpha_A}}(k) / \mathscr{E}^{w}_{base}(k), \tag{7.6}$$

$$\mathscr{E}^{\alpha}_{B}(k) = \mathscr{E}^{w}_{i_{\alpha_B}}(k) / \mathscr{E}^{w}_{base}(k), \tag{7.7}$$

$$\mathscr{E}_C^{\alpha}(k) = \mathscr{E}_{i_{\alpha_C}}^{w}(k)/\mathscr{E}_{base}^{w}(k) \tag{7.8}$$

and

$$\mathscr{E}_A^{0}(k) = \mathscr{E}_{i_0}^{w}(k)/\mathscr{E}_{base}^{w}(k), \tag{7.9}$$

resulting in:

$$\mathscr{E}_A^{\alpha}(k) + \mathscr{E}_B^{\alpha}(k) + \mathscr{E}_C^{\alpha}(k) = 1, \tag{7.10}$$

which simplifies the proposed algorithm and enables it to be used in any system topology.

7.2 The Fault Inception Time Detection

The detection of the fault inception time is out of scope of this thesis, and it is accomplished in accordance with (COSTA, 2014b) by using the RT-SBWT wavelet coefficient energy of phase and zero-sequence currents. In summary, the fault inception time is detected when $\mathscr{E}_{i_A}^{w}$, $\mathscr{E}_{i_B}^{w}$, $\mathscr{E}_{i_C}^{w}$, or $\mathscr{E}_{i_0}^{w}$ exceed a threshold. For instance, a BCG fault performed at d_f = 150 km with $\theta_f = 120^o$ can be seen in Figure 7.1. The fault causes an increase of the currents in 7.1(a) where is highlighted the exact time when the fault occurs and in 7.1(b) the RT-BSWT was used to detect the fault immediately. In the presented case the currents from the three phases increased beyond the threshold and the fault was detected. Therefore, the fault detector can be seen as the wavelet directional trigger.

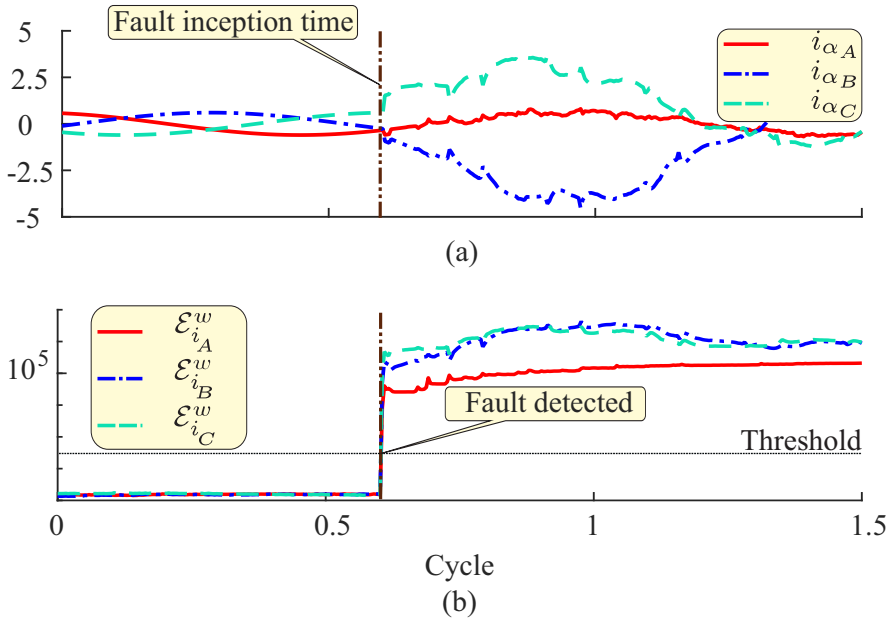

Figure 7.1: BCG fault: (a) phase currents; (b) boundary wavelet coefficient energy of phase currents.

7.3 Energy Diagram for Fault Classification

Figure 7.2 depicts 2D and 3D Cartesian plane representations of normalized energies obtained for all types of faults. Details regarding these faults will be further provided in section

8.1. The graphical representation of the normalized energies $\mathscr{E}_A^{\alpha}$, $\mathscr{E}_B^{\alpha}$, $\mathscr{E}_C^{\alpha}$, and $\mathscr{E}^0$ is very helpful in developing the proposed method and evaluate its performance.

In Figure 7.2(a), the normalized α-mode energies $\mathscr{E}_A^{\alpha}$, $\mathscr{E}_B^{\alpha}$, and $\mathscr{E}_C^{\alpha}$ are considered as a perpendicular projection of an energy point $\mathscr{E}^{\alpha}$ in the 3D Cartesian plane, where $\mathscr{E}^{\alpha}$=$\{\mathscr{E}_A^{\alpha}, \mathscr{E}_B^{\alpha}, \mathscr{E}_C^{\alpha}\}$. Therefore, $\mathscr{E}_A^{\alpha}$, $\mathscr{E}_B^{\alpha}$, and $\mathscr{E}_C^{\alpha}$ are energy coordinates in the energy axes α_A, α_B, and α_C, respectively. According to the normalization process in (7.6), all α-mode energy point possibilities are inside triangular planes: a main triangle ABCA composed by sub-triangles ABGA, BCGB, and CAGC. Moreover, α-mode energy points $\mathscr{E}^{\alpha}$ tend to be located in specific regions of triangular planes in accordance with the type of fault. For instance, in Figure 7.2(a) all α-mode energy points of ABG faults are inside the sub-triangle ABGA under an elliptic path, whereas α-mode energy points of AG faults are concentrated around a single point between the sub-triangles ABGA and CAGC. However, there is a superposition of α-mode energy points in some faults: e.g., energy points of some ABC faults and all AB faults are also placed on the sub-triangle ABGA. Nevertheless, the normalized 0-mode energy $\mathscr{E}^0$, which is also considered in the proposed fault classification method, was not yet considered in Figure 7.2(a), leading to a limitation of this illustration in identifying the fault features.

As all possible α-mode energy points remain on the plane ABCA (Figure 7.2(a)), an equivalent 2D plot can be obtained from the 3D plot by using translation and rotation matrices (MURRAY, 2017). Firstly, a translation of P = -1/3 is accomplished to position the main triangle center to the coordinates (0,0,0). Then, a rotation of $\theta = 45^{\circ}$ around the axis α_C is performed in order to bring the coordinates (0,1,0) to (1,1,0) as follows:

$$\begin{bmatrix} \mathscr{E}_{A1}^{\alpha} \\ \mathscr{E}_{B1}^{\alpha} \\ \mathscr{E}_{C1}^{\alpha} \end{bmatrix} = \begin{bmatrix} \cos\theta & -\sin\theta & 0 & P \\ \sin\theta & \cos\theta & 0 & P \\ 0 & 0 & 1 & P \end{bmatrix} \begin{bmatrix} \mathscr{E}_A^{\alpha} \\ \mathscr{E}_B^{\alpha} \\ \mathscr{E}_C^{\alpha} \\ 1 \end{bmatrix}, \tag{7.11}$$

where $\{\mathscr{E}_{A1}^{\alpha}, \mathscr{E}_{B1}^{\alpha}, \mathscr{E}_{C1}^{\alpha}\}$ are the new energy coordinates.

A second rotation of $\phi = \tan^{-1}(\sqrt{2}) = 54.73^{\circ}$ is performed around the new axis y ($\mathscr{E}_{B1}^{\alpha}$) as follows:

$$\begin{bmatrix} \mathscr{E}_x^{\alpha} \\ \mathscr{E}_y^{\alpha} \end{bmatrix} = \begin{bmatrix} \cos\phi & 0 & \sin\phi \\ 0 & 1 & 0 \end{bmatrix} \begin{bmatrix} \mathscr{E}_{A1}^{\alpha} \\ \mathscr{E}_{B1}^{\alpha} \\ \mathscr{E}_{C1}^{\alpha} \end{bmatrix}, \tag{7.12}$$

where $\{\mathscr{E}_x^{\alpha}, \mathscr{E}_y^{\alpha}\}$ is a new energy coordinate in a 2D plane, with $\mathscr{E}_x^{\alpha}$ and $\mathscr{E}_y^{\alpha}$ as perpendicular projections in the axes α_x and α_y, respectively. Therefore, this procedure brings all 3D information in Figure 7.2(a) to a 2D plane shown in Figure 7.2(b) without loss of information.

Since alpha-energy information can be represented in a 2D plane as shown in Figure 7.2(b), the zero-energy information can be added as the third dimension leading to the 3D graphic representation depicted in Figure 7.2(c). The four normalized Clarke-wavelet energies $\mathscr{E}_A^{\alpha}$, $\mathscr{E}_B^{\alpha}$, $\mathscr{E}_C^{\alpha}$, and $\mathscr{E}^0$ are presented by means of the energy coordinates $\mathscr{E}_x^{\alpha}$, $\mathscr{E}_y^{\alpha}$, $\mathscr{E}_0^{\alpha}$. Based on the graphical representation in Figure 7.2(c), the energies $\mathscr{E}_A^{\alpha}$, $\mathscr{E}_B^{\alpha}$, $\mathscr{E}_C^{\alpha}$, and $\mathscr{E}^0$ can be properly used for fault classification by adopting thresholds since the energy points are well-defined for each type of fault as explained in further sections.

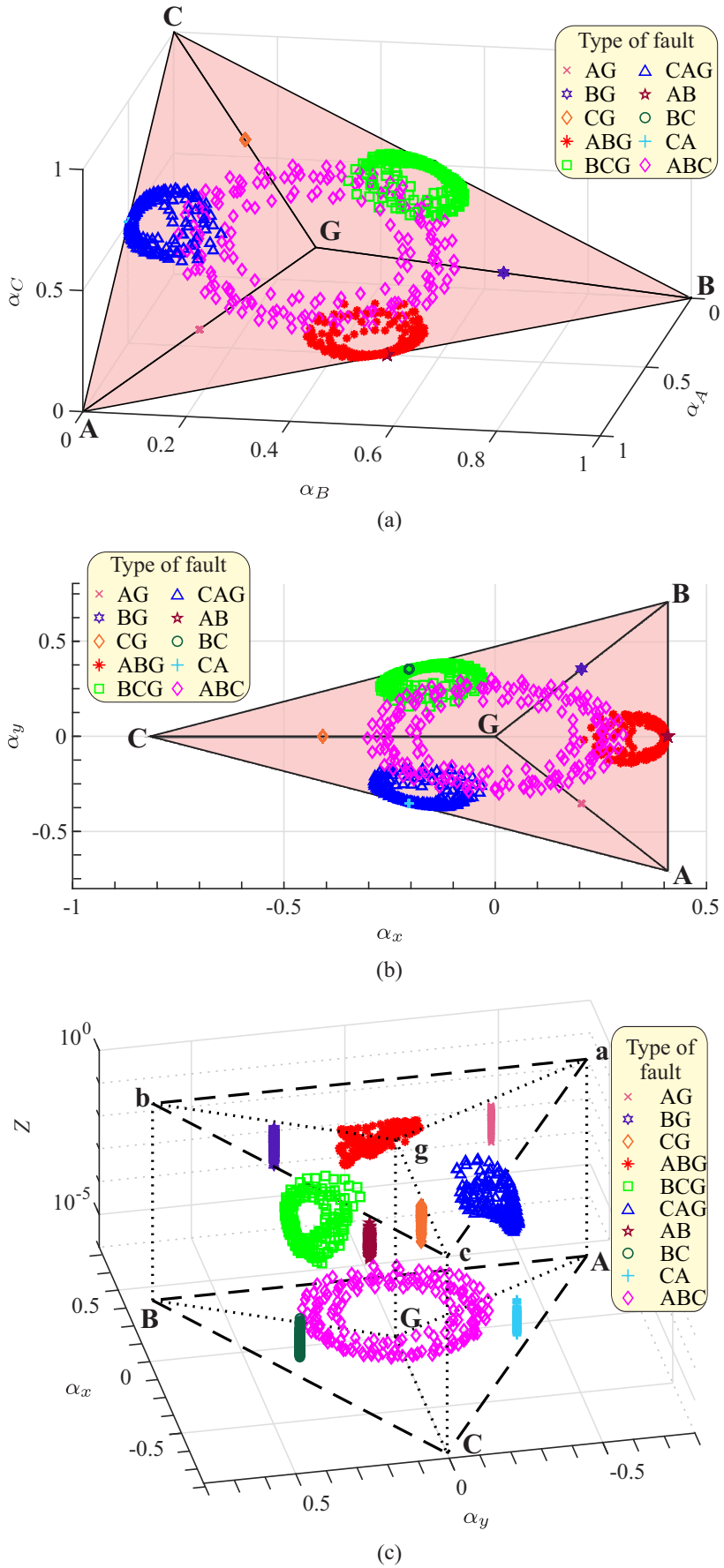

Figure 7.2: The graphic disposition of normalized Clarke energies from several faults: (a) 3D plot of $\mathscr{E}_A^{\alpha}$, $\mathscr{E}_B^{\alpha}$ and $\mathscr{E}_C^{\alpha}$; (b) 2D plot of $\mathscr{E}_x^{\alpha}$ and $\mathscr{E}_y^{\alpha}$; (c) 3D plot of $\mathscr{E}_x^{\alpha}$, $\mathscr{E}_y^{\alpha}$, and $\mathscr{E}_0^{\alpha}$.

7.4 Border Effect Effectiveness

The Clarke-wavelet coefficient energy of currents is sensible to both fault-induced transients and low-frequency-based information due to the border effects of the RT-BSWT. Therefore, the proposed method can classify faults even with dumped transients, which is a key limitation of existing wavelet-based fault classification methods. For instance, Figure 7.3 depicts α-mode energies obtained from the RT-BSWT and the SWT during an ABG fault with the following fault parameters: fault resistance $r_f = 1\ \Omega$, fault distance $d_f = 280$ km, and fault inception angle $\theta_f = 160^\circ$. The classifier based on the SWT would provide a wrong CAG fault classification because $\mathscr{E}^w_{i\alpha_B} < \mathscr{E}^w_{i\alpha_A}$ and $\mathscr{E}^w_{i\alpha_B} < \mathscr{E}^w_{i\alpha_C}$ as shown in Figure 7.3(b). The DWT would face the same issue. Conversely, the proposed method overcomes these drawbacks due to the border effects of the RT-BSWT such as shown in Figure 7.3(c), where $\mathscr{E}^w_{i\alpha_A} > \mathscr{E}^w_{i\alpha_C}$ and $\mathscr{E}^w_{i\alpha_B} > \mathscr{E}^w_{i\alpha_C}$ as expected in a ABG fault.

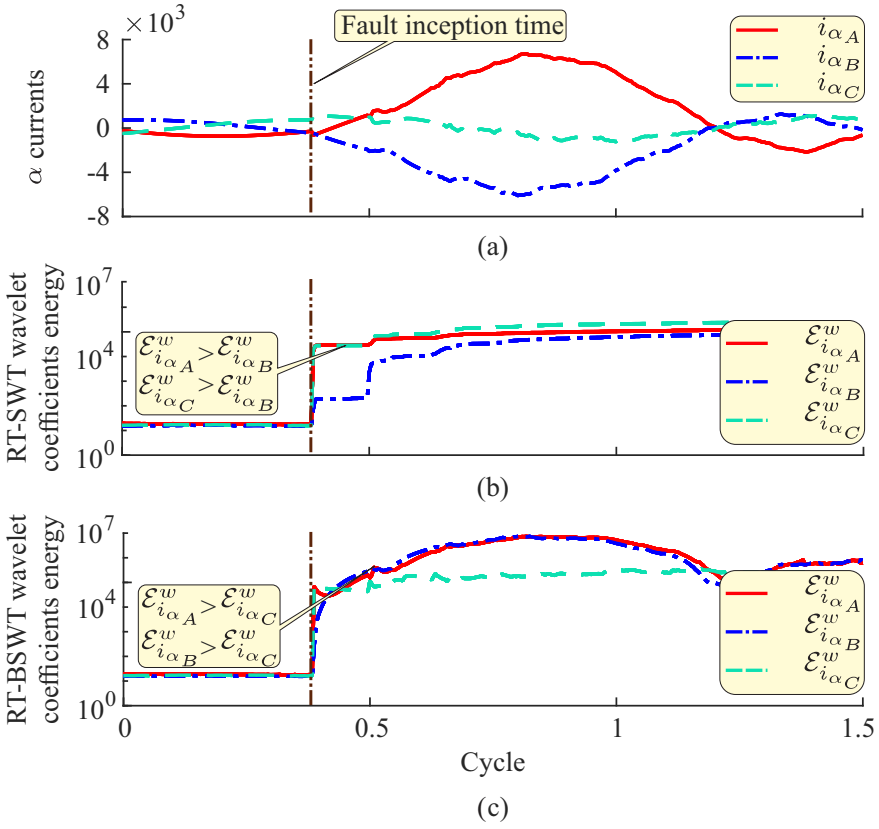

Figure 7.3: ABG fault: (a) α currents; (b) wavelet coefficient energy of the α currents; (c) boundary wavelet coefficient energy of the α currents.

7.5 Ideal Fault Classification Thresholds

The proposed method extends the classical border fault conditions applied to Clarke currents presented in Tables 3.2-3.5 to Clarke-wavelet energies. The Clarke fault boundary conditions are used to find the ideal threshold in terms of Clarke energy.

SLG Faults

The SLG fault boundary conditions follows as presented in Table 3.2. For instance, at the fault point, the fault boundary conditions in AG fault currents are represented by i_{BF}=i_{CF}=0 and $i_{AF}\neq 0$. By using (3.26), SLG faults are characterized in terms of the Clarke transform as follows: $i_{\alpha_{AF}}=\sqrt{2/3}i_{AF}$, $i_{\alpha_{BF}}=-\sqrt{1/6}i_{AF}$, $i_{\alpha_{CF}}=-\sqrt{1/6}i_{AF}$, and $i_{0F}=\sqrt{1/3}i_{AF}$. Therefore, the boundary conditions to AG faults in terms of Clarke energies are given by: $\mathscr{E}_{i_{\alpha AF}}(k)$=(2/3)$\mathscr{E}_{i_{AF}}(k)$, $\mathscr{E}_{i_{\alpha BF}}(k)$=(1/6)$\mathscr{E}_{i_{AF}}(k)$, $\mathscr{E}_{i_{\alpha CF}}(k)$=(1/6)$\mathscr{E}_{i_{AF}}(k)$, and $\mathscr{E}_{i_{0F}}(k)$=(1/3)$\mathscr{E}_{i_{AF}}(k)$. The index F in current and energy variables indicates boundary conditions at the fault point.

By using (7.5), the normalization energy at the AG fault point is as follows:

$$\mathscr{E}_{base}(k)=\frac{2}{3}\mathscr{E}_{i_{AF}}(k)+\frac{1}{6}\mathscr{E}_{i_{AF}}(k)+\frac{1}{6}\mathscr{E}_{i_{AF}}(k)=\mathscr{E}_{i_{AF}}(k). \tag{7.13}$$

Therefore, the normalized α- and 0-mode energy components to AG fault are given by:

$$\mathscr{E}^{\alpha}_{AF}(k)=\frac{2}{3}\mathscr{E}_{i_{AF}}/\mathscr{E}_{base}(k)=2/3, \tag{7.14}$$

$$\mathscr{E}^{\alpha}_{BF}(k)=\frac{1}{6}\mathscr{E}_{i_{AF}}/\mathscr{E}_{base}(k)=1/6, \tag{7.15}$$

$$\mathscr{E}^{\alpha}_{CF}(k)=\frac{1}{6}\mathscr{E}_{i_{AF}}/\mathscr{E}_{base}(k)=1/6, \tag{7.16}$$

and

$$\mathscr{E}^{0}_{F}(k)=\frac{1}{3}\mathscr{E}^{w}_{i_{AF}}/\mathscr{E}_{base}(k)=1/3. \tag{7.17}$$

Following this reasoning, the ideal normalized energies for SLG faults are summarized in Table 7.1.

Table 7.1: Ideal energy threshold to SLG faults.

	$\mathscr{E}^{\alpha}_{AF}$	$\mathscr{E}^{\alpha}_{BF}$	$\mathscr{E}^{\alpha}_{CF}$	$\mathscr{E}^{0}_{F}$
AG	2/3	1/6	1/6	1/3
BG	1/6	2/3	1/6	1/3
CG	1/6	1/6	2/3	1/3

DL Faults

The DL faults follow the fault boundary conditions summarized in Table 3.3. Therefore, the boundary conditions to AB faults in terms of Clarke energies are given by: $\mathscr{E}_{i_{\alpha AF}}(k)=(3/2)\mathscr{E}_{i_{AF}}(k)$, $\mathscr{E}_{i_{\alpha BF}}(k)$=(3/2)$\mathscr{E}_{i_{AF}}(k)$, $\mathscr{E}_{i_{\alpha CF}}(k)$=0$\mathscr{E}_{i_{AF}}(k)$, and $\mathscr{E}_{i_{0F}}(k)$=0$\mathscr{E}_{i_{AF}}(k)$. The normalization energy, the base energy, at the AB fault point is as follows:

$$\mathscr{E}_{base}(k)=\frac{3}{2}\mathscr{E}_{i_{AF}}(k)+\frac{3}{2}\mathscr{E}_{i_{AF}}(k)+0\mathscr{E}_{i_{AF}}(k)=3\mathscr{E}_{i_{AF}}(k). \tag{7.18}$$

Therefore, the normalized α- and 0-mode energy components to AB fault are given by:

$$\mathscr{E}^{\alpha}_{AF}(k) = \frac{3}{2}\mathscr{E}_{i_{AF}}(k)/3\mathscr{E}_{base}(k) = 1/2, \tag{7.19}$$

$$\mathscr{E}^{\alpha}_{BF}(k) = \frac{3}{2}\mathscr{E}_{i_{AF}}(k)/3\mathscr{E}_{base}(k) = 1/2, \tag{7.20}$$

$$\mathscr{E}^{\alpha}_{CF}(k) = 0\mathscr{E}_{i_{AF}}(k)/3\mathscr{E}_{base}(k) = 0, \tag{7.21}$$

and

$$\mathscr{E}^{0}_{F}(k) = 0\mathscr{E}_{i_{AF}}(k)/3\mathscr{E}_{base}(k) = 0. \tag{7.22}$$

The ideal threshold to DL faults are summarized in Table 7.2.

Table 7.2: Ideal energy threshold to DL faults.

	$\mathscr{E}^{\alpha}_{AF}$	$\mathscr{E}^{\alpha}_{BF}$	$\mathscr{E}^{\alpha}_{CF}$	$\mathscr{E}^{0}_{F}$
AB	1/2	1/2	0	0
BC	0	1/2	1/2	0
CA	1/2	0	1/2	0

DLG Fault

The DLG faults follow the fault boundary conditions summarized in Table 3.4. For instance, the $i_{\alpha AF}$ is defined as follows:

$$i_{\alpha AF}(k) = \frac{2i_A(k) - i_B(k)}{\sqrt{6}}. \tag{7.23}$$

In order to find the Clarke spectral energy, this current can be squared as follows:

$${i_{\alpha AF}}^2(k) = \frac{1}{6}(2i_A(k) - i_B(k))^2 = \frac{1}{6}(4{i_A}^2(k) + i^2_B(k) - 4i_A(k)i_B(k)), \tag{7.24}$$

The Clarke energy can be defined for each phase and zero as follows:

$$\mathscr{E}_{i_{\alpha AF}}(k) = \frac{2}{3}\sum_{n=k-\Delta k+1}^{k} i^2_{AF}(n) + \frac{1}{6}\sum_{n=k-\Delta k+1}^{k} i^2_{BF}(n) - \frac{2}{3}\sum_{n=k-\Delta k+1}^{k} i_{AF}(n)i_{BF}(n), \tag{7.25}$$

$$\mathscr{E}_{i_{\alpha AF}}(k) = \frac{1}{6}\sum_{n=k-\Delta k+1}^{k} i^2_{AF}(n) + \frac{2}{3}\sum_{n=k-\Delta k+1}^{k} i^2_{BF}(n) - \frac{2}{3}\sum_{n=k-\Delta k+1}^{k} i_{AF}(n)i_{BF}(n), \tag{7.26}$$

$$\mathscr{E}_{i_{\alpha AF}}(k) = \frac{1}{6}\sum_{n=k-\Delta k+1}^{k} i^2_{AF}(n) + \frac{1}{6}\sum_{n=k-\Delta k+1}^{k} i^2_{BF}(n) + \frac{1}{3}\sum_{n=k-\Delta k+1}^{k} i_{AF}(n)i_{BF}(n) \tag{7.27}$$

and

$$\mathscr{E}_{i_{0F}}(k) = \frac{1}{3}\sum_{n=k-\Delta k+1}^{k} i^2_{AF}(n) + \frac{1}{2}\sum_{n=k-\Delta k+1}^{k} i^2_{BF}(n) + \frac{2}{3}\sum_{n=k-\Delta k+1}^{k} i_{AF}(n)i_{BF}(n), \tag{7.28}$$

where $\sum_{n=k-\Delta k+1}^{k} i_{AF}(n) i_{BF}(n) \approx 0$ in the steady state. Therefore:

$$\mathscr{E}_{i_{\alpha AF}}(k) = \frac{2}{3}\mathscr{E}_{i_{AF}}(k) + \frac{1}{6}\mathscr{E}_{i_{BF}}(k). \tag{7.29}$$

$$\mathscr{E}_{i_{\alpha BF}}(k) = \frac{1}{6}\mathscr{E}_{i_{AF}}(k) + \frac{2}{3}\mathscr{E}_{i_{BF}}(k) \tag{7.30}$$

$$\mathscr{E}_{i_{\alpha CF}}(k) = \frac{1}{6}\mathscr{E}_{i_{AF}}(k) + \frac{1}{6}\mathscr{E}_{i_{BF}}(k) \tag{7.31}$$

and

$$\mathscr{E}_{i_{0F}}(k) = \frac{1}{3}\mathscr{E}_{i_{AF}}(k) + \frac{1}{3}\mathscr{E}_{i_{BF}}(k). \tag{7.32}$$

The normalization energy, the base energy, at the ABG fault point is as follows:

$$\mathscr{E}_{base}(k) = \mathscr{E}_{i_{AF}}(k) + \mathscr{E}_{i_{BF}}(k) \tag{7.33}$$

Therefore, the normalized α- and 0-mode energy components to ABG fault are given by:

$$\begin{aligned}\mathscr{E}^{\alpha}_{AF}(k) = \frac{\mathscr{E}_{i_{\alpha AF}}(k)}{\mathscr{E}_{base}(k)} = \frac{1}{6}\left(\frac{4\mathscr{E}_{i_{AF}}(k) + \mathscr{E}_{i_{BF}}(k)}{\mathscr{E}_{i_{AF}}(k) + \mathscr{E}_{i_{BF}}(k)}\right) = \frac{1}{6}\left(1 + 3\left(\frac{\mathscr{E}_{i_{AF}}(k)}{\mathscr{E}_{i_{AF}}(k) + \mathscr{E}_{i_{BF}}(k)}\right)\right) \\ = \frac{1}{6}(1 + 3\upsilon_1),\end{aligned} \tag{7.34}$$

$$\begin{aligned}\mathscr{E}^{\alpha}_{BF}(k) = \frac{\mathscr{E}_{i_{\alpha BF}}(k)}{\mathscr{E}_{base}(k)} = \frac{1}{6}\left(\frac{\mathscr{E}_{i_{AF}}(k) + 4\mathscr{E}_{i_{BF}}(k)}{\mathscr{E}_{i_{AF}}(k) + \mathscr{E}_{i_{BF}}(k)}\right) = \frac{1}{6}\left(1 + 3\left(\frac{\mathscr{E}_{i_{BF}}(k)}{\mathscr{E}_{i_{AF}}(k) + \mathscr{E}_{i_{BF}}(k)}\right)\right) \\ = \frac{1}{6}(1 + 3\upsilon_2),\end{aligned} \tag{7.35}$$

$$\mathscr{E}^{\alpha}_{CF}(k) = \frac{\mathscr{E}_{i_{\alpha CF}}(k)}{\mathscr{E}_{base}(k)} = \frac{1}{6}\left(\frac{\mathscr{E}_{i_{AF}}(k) + \mathscr{E}_{i_{BF}}(k)}{\mathscr{E}_{i_{AF}}(k) + \mathscr{E}_{i_{BF}}(k)}\right) = \frac{1}{6}, \tag{7.36}$$

and

$$\mathscr{E}^{0}_{F}(k) = \frac{\mathscr{E}_{i_{0F}}(k)}{\mathscr{E}^{(}_{base}k)} = \frac{1}{3}\left(\frac{\mathscr{E}_{i_{AF}}(k) + \mathscr{E}_{i_{BF}}(k)}{\mathscr{E}_{i_{AF}}(k) + \mathscr{E}_{i_{BF}}(k)}\right) = \frac{1}{3}, \tag{7.37}$$

where $\upsilon_1 \geq 0$ and $\upsilon_2 \geq 0$. By using (7.33), υ_1 and υ_2 can be limited as follows:

$$\upsilon_1 = \frac{\mathscr{E}_{i_{AF}}(k)}{\mathscr{E}_{i_{AF}}(k) + \mathscr{E}_{i_{BF}}(k)} = \frac{\mathscr{E}_{i_{AF}}(k)}{\mathscr{E}_{base}(k)} \leq 1 \tag{7.38}$$

and

$$\upsilon_2 = \frac{\mathscr{E}_{i_{BF}}(k)}{\mathscr{E}_{i_{AF}}(k) + \mathscr{E}_{i_{BF}}(k)} = \frac{\mathscr{E}_{i_{AF}}(k)}{\mathscr{E}^{w}_{base}(k)} \leq 1. \tag{7.39}$$

which means $0 \leq \upsilon_1 \leq 1$ and $0 \leq \upsilon_2 \leq 1$.

These evaluations leads to define a range of possible values to $\mathscr{E}^{\alpha}_{AF}(k)$ and $\mathscr{E}^{\alpha}_{BF}(k)$. Reorganizing (7.34) and (7.35), υ_1 and υ_2 can be written as as follows:

$$\upsilon_1 = \frac{1}{3}(6\mathscr{E}^{\alpha}_{AF}(k) - 1) => \begin{cases}\mathscr{E}^{\alpha}_{AF}(k) \geq 1/3 \\ \mathscr{E}^{\alpha}_{AF}(k) \leq 2/3\end{cases} \tag{7.40}$$

and

$$\upsilon_2 = \frac{1}{3}(6\mathscr{E}^{\alpha}_{BF}(k) - 1) => \begin{cases} \mathscr{E}^{\alpha}_{BF}(k) \geq 1/3 \\ \mathscr{E}^{\alpha}_{BF}(k) \leq 2/3. \end{cases} \tag{7.41}$$

Following this reasoning, the ideal normalized energies for DLG faults are summarized in Table 7.3.

Table 7.3: Ideal energy threshold to DLG faults.

	$\mathscr{E}^{\alpha}_{AF}$	$\mathscr{E}^{\alpha}_{BF}$	$\mathscr{E}^{\alpha}_{CF}$	$\mathscr{E}^{0}_{F}$
ABG	[1/6 2/3]	[1/6 2/3]	1/6	1/3
BCG	1/6	[1/6 2/3]	[1/6 2/3]	1/3
CAG	[1/6 2/3]	1/6	[1/6 2/3]	1/3

LLL Fault

The DLL faults follow the fault boundary conditions summarized in Table 3.5. For instance, the $i_{\alpha AF}$ currents was defined as follows:

$$i_{\alpha AF}(k) = \frac{2i_A(k) - i_B(k) - i_C}{\sqrt{6}}. \tag{7.42}$$

Then, this current can be squared as follows:

$$\begin{aligned} {i_{\alpha AF}}^2(k) &= \frac{1}{6}(2i_A(k) - i_B(k) - i_C(k))^2 \\ = \frac{1}{6}({i_A}^2(k) + i_B^2(k) + i_C^2(k) - 4i_A(k)i_B(k) - 4i_A(k)i_C(k) + 2i_B(k)i_C(k)), \end{aligned} \tag{7.43}$$

After the spectral energy being computed through the wavelet transfom, the Clarke energy are given by:

$$\mathscr{E}_{i_{\alpha AF}}(k) = \frac{2}{3}\mathscr{E}_{i_{AF}}(k) + \frac{1}{6}\mathscr{E}_{i_{BF}}(k)\frac{1}{6}\mathscr{E}_{i_{CF}}(k) \tag{7.44}$$

$$\mathscr{E}_{i_{\alpha BF}}(k) = \frac{1}{6}\mathscr{E}_{i_{AF}}(k) + \frac{2}{3}\mathscr{E}_{i_{BF}}(k) + \frac{1}{6}\mathscr{E}_{i_{CF}}(k) \tag{7.45}$$

$$\mathscr{E}_{i_{\alpha CF}}(k) = \frac{1}{6}\mathscr{E}_{i_{AF}}(k) + \frac{1}{6}\mathscr{E}_{i_{BF}}(k) + \frac{2}{6}\mathscr{E}_{i_{CF}}(k) \tag{7.46}$$

and

$$\mathscr{E}_{i_{0F}}(k) = 0. \tag{7.47}$$

The normalization energy at the ABC fault point is as follows:

$$\mathscr{E}_{base}(k) = \mathscr{E}_{i_{AF}}(k) + \mathscr{E}_{i_{BF}}(k) + \mathscr{E}_{i_{CF}}(k) \tag{7.48}$$

Therefore, the normalized α- and 0-mode energy components to ABG fault are given by:

$$\mathscr{E}^{\alpha}_{AF}(k) = \frac{\mathscr{E}_{i_{\alpha AF}}(k)}{\mathscr{E}_{base}(k)} = \frac{1}{6}\left(\frac{4\mathscr{E}_{i_{AF}}(k) + \mathscr{E}_{i_{BF}}(k) + \mathscr{E}_{i_{CF}}(k)}{\mathscr{E}_{i_{AF}}(k) + \mathscr{E}_{i_{BF}}(k) + \mathscr{E}_{i_{CF}}(k)}\right) => \begin{cases} \mathscr{E}^{\alpha}_{AF}(k) \geq 1/3 \\ \mathscr{E}^{\alpha}_{AF}(k) \leq 2/3, \end{cases} \tag{7.49}$$

$$\mathscr{E}^{\alpha}_{BF}(k) = \frac{\mathscr{E}_{i_{\alpha BF}}(k)}{\mathscr{E}_{base}(k)} = \frac{1}{6}\left(\frac{\mathscr{E}_{i_{AF}}(k) + 4\mathscr{E}_{i_{BF}}(k) + \mathscr{E}_{i_{CF}}(k)}{\mathscr{E}_{i_{AF}}(k) + \mathscr{E}_{i_{BF}}(k) + \mathscr{E}_{i_{CF}}(k)}\right) => \begin{cases} \mathscr{E}^{\alpha}_{BF}(k) \geq 1/3 \\ \mathscr{E}^{\alpha}_{BF}(k) \leq 2/3, \end{cases} \tag{7.50}$$

$$\mathscr{E}^{\alpha}_{CF}(k) = \frac{\mathscr{E}_{i_{\alpha CF}}(k)}{\mathscr{E}_{base}(k)} = \frac{1}{6}\left(\frac{\mathscr{E}_{i_F}(k) + \mathscr{E}_{i_{BF}}(k) + 4\mathscr{E}_{i_{CF}}(k)}{\mathscr{E}_{i_{AF}}(k) + \mathscr{E}_{i_{BF}}(k) + \mathscr{E}_{i_{CF}}(k)}\right) => \begin{cases} \mathscr{E}^{\alpha}_{CF}(k) \geq 1/3 \\ \mathscr{E}^{\alpha}_{CF}(k) \leq 2/3 \end{cases} \tag{7.51}$$

and

$$\mathscr{E}^{0}_{F}(k) = 0. \tag{7.52}$$

The LLL faults follow the fault boundary conditions summarized in Table 3.5. Therefore, the boundary conditions to LLL, follwing the same reasoning is summarized at Table 7.4.

Table 7.4: Ideal energy threshold to LLL faults.

	$\mathscr{E}^{\alpha}_{AF}$	$\mathscr{E}^{\alpha}_{BF}$	$\mathscr{E}^{\alpha}_{CF}$	$\mathscr{E}^{0}_{F}$
ABC	[1/6 2/3]	[1/6 2/3]	[1/6 2/3]	0

The reasoning presented in this section to the spectral energy can be extended to the wavelet energy from RT-BSWT once this energy is influenced by high and low frequency. Therefore, all threshold defined in this section is going to be considered as ideal valid threshold for the next sections.

7.6 Identification of Earth Faults

According to Tables 7.1 and 7.3, SLG and DLG faults can be readily distinguished from LL and LLL faults by means of the normalized zero-energy component, which presents an ideal value of 1/3 in SLG and DLG faults or zero in LL and LLL. However, besides noise, a real power system presents other uncertainties such as current unbalances. Therefore, the zero-energy threshold is redefined as follows:

$$\varepsilon_0(k) = \eta_0 \overline{\mathscr{E}^0} / \mathscr{E}^{w}_{base}(k), \tag{7.53}$$

where $\overline{\mathscr{E}^0}$ is the average of $\mathscr{E}^0$ during one-cycle of the steady-state; η_0 is a multiplicative factor to enhance the reliability of the defined threshold. ε_0 is a variable because $\mathscr{E}^{w}_{base}$ changes with time, and it can properly distinguish fault-induced transients from noise and unbalance effects of the system. In addition, this threshold based on steady-state noise becomes flexible to be applied to any transmission line. In a real application, ε_0 can be periodically updated to offer a realistic value from the unbalance and noise present in the system.

7.7 Identification of Faulted Phases

After the identification of SLG and DLG faults with the 0-mode energy threshold ε_0, the normalized alpha-energy components $\mathscr{E}^{\alpha}_{A}$, $\mathscr{E}^{\alpha}_{B}$, and $\mathscr{E}^{\alpha}_{C}$ properly distinguish SLG and DLG faults with alpha-energy values in Tables 7.1 and 7.3. For instance, $\mathscr{E}^{\alpha}_{A}$, $\mathscr{E}^{\alpha}_{B}$, and $\mathscr{E}^{\alpha}_{C}$ of AG faults in Figure 7.2(a) are around the ideal alpha-energy values of 2/3, 1/6, and 1/6, respectively, whereas in ABG fault $\mathscr{E}^{\alpha}_{C}$ presented a fixed value at 1/6 and $\mathscr{E}^{\alpha}_{A}$ and $\mathscr{E}^{\alpha}_{B}$ are limited to a range [1/6 2/3] in accordance with Table 7.1 and 7.3. Considering that $\mathscr{E}^{\alpha}_{A} + \mathscr{E}^{\alpha}_{B} + \mathscr{E}^{\alpha}_{C} = 1$ according to the adopted normalization, and given that the magnitude of fault-induced transients changes as a

sinusoidal function of the fault inception angle (COSTA; SOUZA; BRITO, 2012a), then the energy points of ABG faults describe an elliptical path around $\mathscr{E}_C^{\alpha} = 1/6$ as shown in Figure 7.2(a), never crossing energy points of SLG and other DLG faults.

After the identification of LL and LLL faults with the 0-mode energy threshold ε_0, the normalized α-mode energy components $\mathscr{E}_A^{\alpha}$, $\mathscr{E}_B^{\alpha}$, and $\mathscr{E}_C^{\alpha}$ also properly distinguish LL and LLL faults with alpha-energy values in Tables 7.2 and 7.4. For instance, $\mathscr{E}_A^{\alpha}$, $\mathscr{E}_B^{\alpha}$, and $\mathscr{E}_C^{\alpha}$ of AB faults in Figure 7.2(a) are around the ideal alpha-energy values of 1/2, 1/2, and 0, respectively, whereas in ABG fault normalized alpha-energies are limited in a range [1/6 2/3] in accordance with Tables 7.2 and 7.3, respectively. Considering that $\mathscr{E}_A^{\alpha} + \mathscr{E}_B^{\alpha} + \mathscr{E}_C^{\alpha} = 1$ and given that the magnitude of fault-induced transients changes as a sinusoidal function of the fault inception angle (COSTA; SOUZA; BRITO, 2012a), the energy points of ABC faults are expected to describe the path of a circle around the central point of the main triangle as shown in Figure 7.2(a).

Based on the ideal values in Tables 7.1 - 7.4, the following thresholds are suggested for the fault classification and phase selection:

$$\varepsilon_{\alpha 1} = (2/3)\rho, \tag{7.54}$$

$$\varepsilon_{\alpha 2} = (1/6)\rho, \tag{7.55}$$

and

$$\varepsilon_{\alpha 3} = (1/2)\rho, \tag{7.56}$$

where $0 < \rho < 1$ is a factor of flexibility in order to apply these thresholds within real power systems, where normally noise is present.

7.8 The Fault Classification Algorithm

Figure 7.4 depicts the flowchart of the proposed method, which is performed at each sampling time interval. The time-domain currents are obtained from current transformers followed by low-pass filters to avoid anti-aliasing effect and by an analog-to-digital conversion process. The RT-BSWT computes the wavelet coefficients from the three-phase currents, then the Clarke transform extracts α- and 0-mode components from wavelet coefficients. Thereafter, the Clarke-wavelet coefficient energies are computed, followed by their normalization. The thresholds ε_{α_1}, ε_{α_2}, and ε_{α_3} are fixed values, whereas ε_0 is computed at each sampling time interval. The FA, FB, FC, and FG variables refer to faults involving the phases A, B, C, and G, respectively.

According to Figure 7.4, after the detection of fault-induced transients, the proposed method verifies if the fault has the zero component. Therefore, if $\mathscr{E}^0(k) > \varepsilon_0(k)$ is true, the method identifies SLG and DLG faults as follows: 1) if two α-mode energies are higher than $\varepsilon_{\alpha 1}$ and the third α-mode energy is higher than $\varepsilon_{\alpha 2}$, then it is an SLG fault with the faulted phase indicated by this third alpha-energy; 2) if an SLG fault is not detected, then it is a DLG fault, where the two highest α-mode energies indicate the faulted phase. Conversely, if $\mathscr{E}^0(k) \leq \varepsilon_0(k)$ is true, the method identifies LL and LLL faults as follows: 1) if two α-mode energies are higher than $\varepsilon_{\alpha 3}$ and the third α-mode energy is lower than ε_0, then it is an LL fault with the faulted phases indicated with the two highest α-mode energies; 2) otherwise, it is an LLL fault.

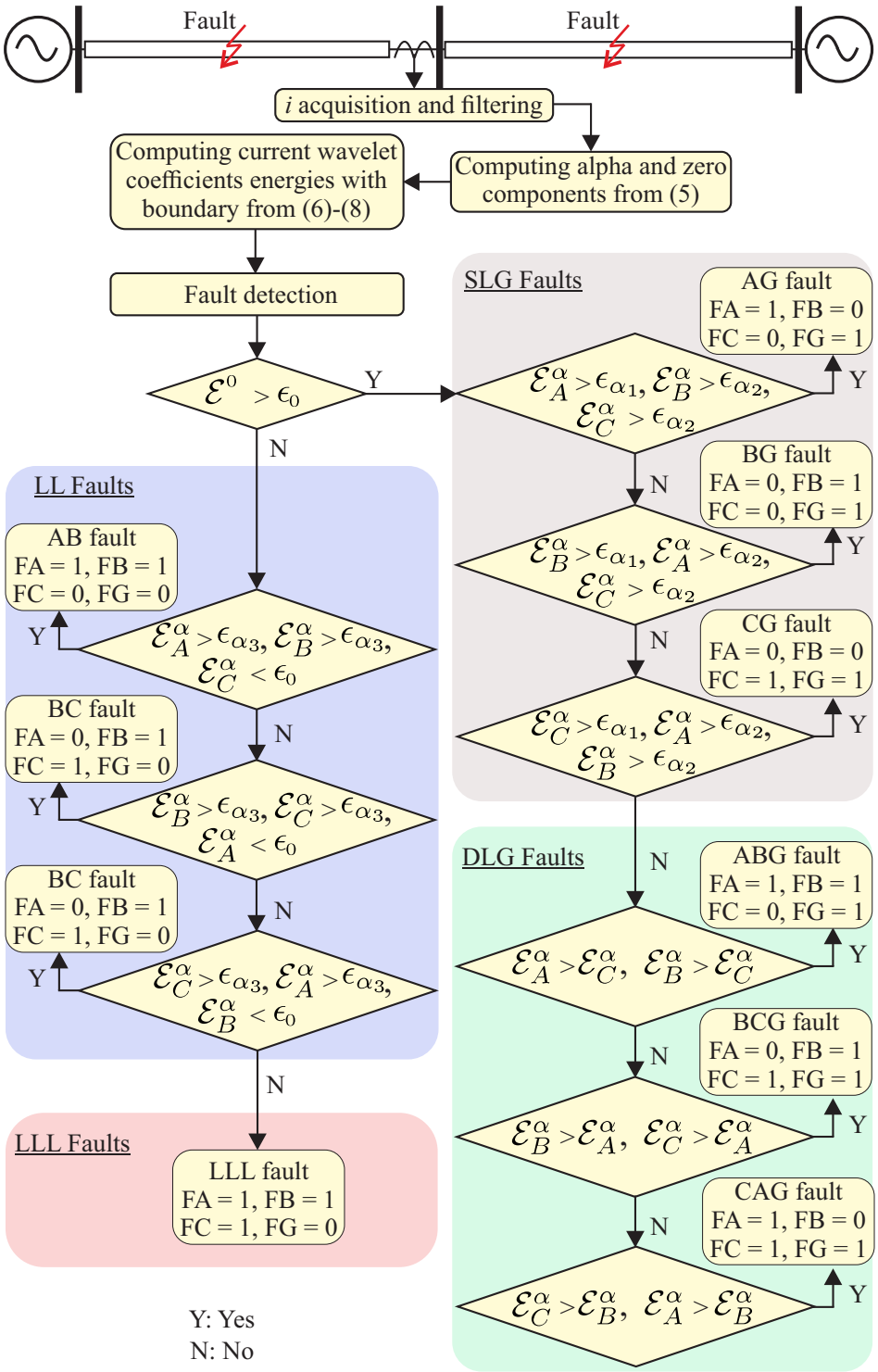

Figure 7.4: Flowchart of the proposed classification method.

7.9 Classification of Evolving Faults

As aforementioned, the fault is detected based on the fault detection method proposed in (COSTA, 2014a), which detects also transients induced by an evolving fault. Therefore, when the first stage of the fault (F1) is detected, the proposed method classifies the fault according to Fig. 7.4. Thereafter, if an evolving fault (stage F2) is detected, the same fault classification algorithm shown in Figure 7.4 is used. However, the classification of the evolving fault is an OR operation between the related flags FA, FB, FC, and FG of each fault stage as shown in Fig. 7.5.

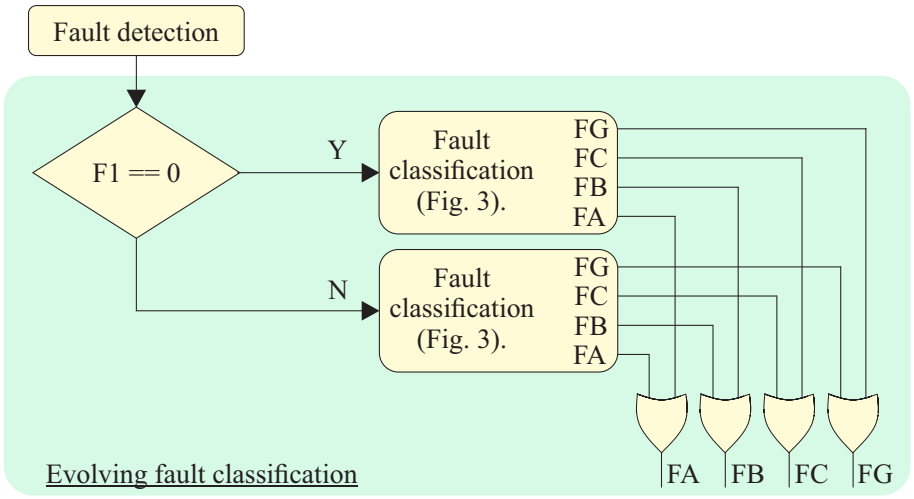

Figure 7.5: Logic flow to evolving fault classification

7.10 Summary

A fault classifier based on RT-BSWT and Clarke transfom were presented. The use of the mathematical tools and the thresholds were justified. In addition, the proposed method was summarized with the details about the respective thresholds and extend to evolving fault conditions.

Chapter 8

Performance Assessment of the Proposed Fault Classifier

In this chapter, the proposed fault classifier method is extensively evaluated under different fault and power system conditions such as fault inception angle, fault distance, fault resistance, series-compensated lines, system loading, source strength as well as evolving faults in order to prove its efficiency. The main results were performance at a 500-kV power system and some minor evaluations were made at a 230-kV power system.

8.1 Performance Assessment

The proposed method was evaluated considering a 500-kV power system depicted in Figure 8.1 with parameters based on an actual system (COSTA; SOUZA; BRITO, 2010). Each transmission line has a length of 300 km and was modeled with distributed and frequency-constant parameters in Simulink/Matlab. The power system fundamental frequency is f = 60 Hz, the simulation frequency was 153600 Hz and the sampling frequency is f_s = 15360 Hz. A 60-dB SNR (signal-to-noise ratio) was added to the currents and a second order Butterworth filter defined, in (6.1), was used to avoid anti-aliasing effect. Faults were simulated on the line TL1, and currents were measured at the terminal connected to the bus B2.

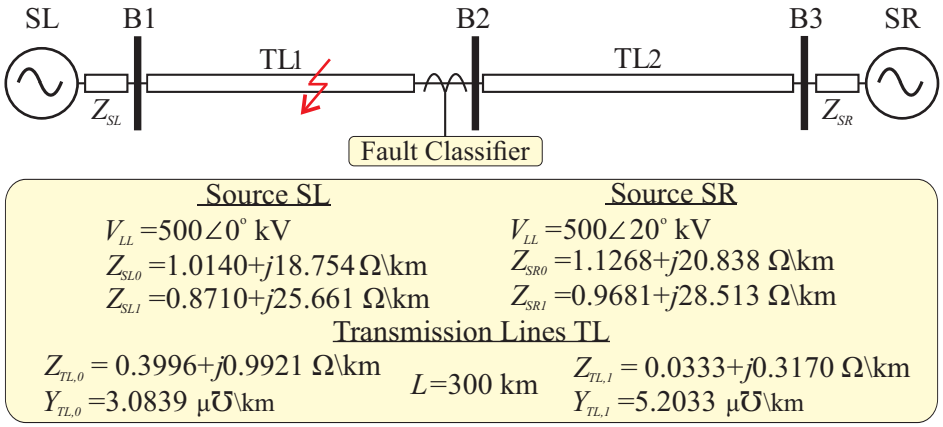

Figure 8.1: Single-line diagram for the tested three-phase 500- kV power system.

The ground-related thresholds of (7.53) and (7.54) were set to $\rho = 0.98$ and $\eta_0 = 3.0$, empirically. The Daubechies mother wavelet with four coefficients (db4) was selected because

it is the most used and effective mother wavelet in power system applications (MALATHI; MARIMUTHU; BASKAR, 2010).

8.1.1 General Performance

A total of 36200 faults was simulated to evaluate the proposed fault classification method considering the influence of the fault inception angle (θ_f), fault distance (d_f), fault resistance (R_f), series compensation of the line (SC), power system loading angle (δ), and the strength of the source SL (signal-to-interference ratio - SIR) (SIR_L) according to Table 8.1.

The fault detection, taken as trigger to initiate the proposed fault classification method, is obtained by means of the detection method based on phase- and zero-energies as proposed in (COSTA, 2014a). With this method the fault detection time was accurately obtained in all cases even in faults with damped fault-induced transients. Since the fault detection method is not the focus of this thesis, only the performance of the fault classification method is addressed in the remainder of this chapter.

Considering all the 36200 faults in Table 8.1, the speed of the classification is summarized in Figure 8.2(a), where the fault classification attained a success rate of 100% within 2.1 ms (32 sampling times or $\Delta k/8$ cycle). Good classification rates were also obtained in times smaller than 2.1 ms. For instance, Figure 8.3 presents the confusion matrix of the proposed fault classification at 1.0 ms (16 samples), where a quite remarkable accuracy of 98.1% was obtained.

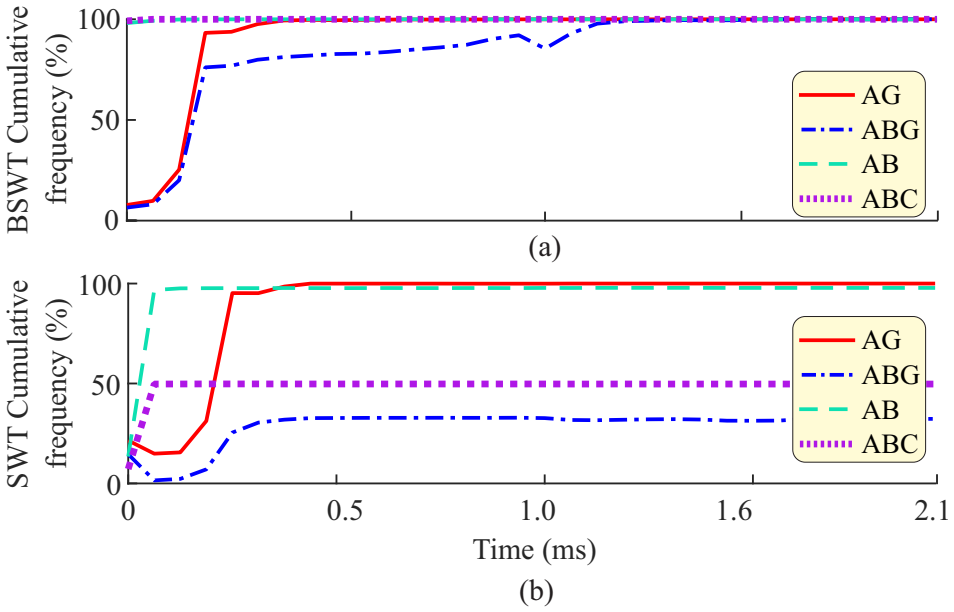

Figure 8.2: Success rate as function of sampling time: a) proposed method; b) method in (COSTA; SOUZA; BRITO, 2012b).

According to Figure 8.3, for SLG, LL and LLL faults, a success rate close to 100% was achieved in 1.0 ms . For instance, 99.93% of SLG faults, the most common fault in the power system (GRAINGER; JR., 1994), were properly classified at 1.0 ms. Therefore, the proposed method can offer a reliable and fast fault classification, which can support fast protections schemes. For instance, directional protection schemes usually need a fault classification or fault type selection (LEAL; COSTA; CAMPOS, 2019). Those based on time domain principles are designed to operate between 2 and 4 ms (SCHWEITZER; KASZTENNY; MYNAM, 2016).

Table 8.1: Cases used for the performance evaluation.

Evaluated parameter		Default parameters							Number
Description	Values	Type	θ_f	d_f	r_f	SC	δ	SIR_L	of faults
Fault inception angle	θ_f={0,1,2,...,180}°	✓	✓	✓	✓	✓	✓	✓	1810
Fault distance	d_f={0,20,150,280,300} km	✓	✓		✓	✓	✓	✓	9050
Ground fault resistance	r_f={1,50,100,300} Ω	SLG+DLG	✓	✓		✓	✓	✓	4344
Phase fault resistance	r_f={1,50,100,300} Ω	LL+LLL	✓	✓		✓	✓	✓	2896
Line series compensation	CS={30,50,70}%	✓	✓	✓	✓		✓	✓	5430
Power system loading angle	δ={±5,±15,±35}%	✓	✓	✓	✓	✓		✓	10860
Source strength	SIR_L={0.1,5,10}	✓	✓	✓	✓	✓	✓		5430

Default parameters given by ✓: θ_f={0,1,2,...,180}°; d_f=150 km; r_f=1 Ω; CS=0%; δ=20%; SIR_L=26.22; Type=SLG(AG,BG,CG), LL(AB,BC,CA), DLG(ABG,BCG,CAG), and LLL(ABC) faults.

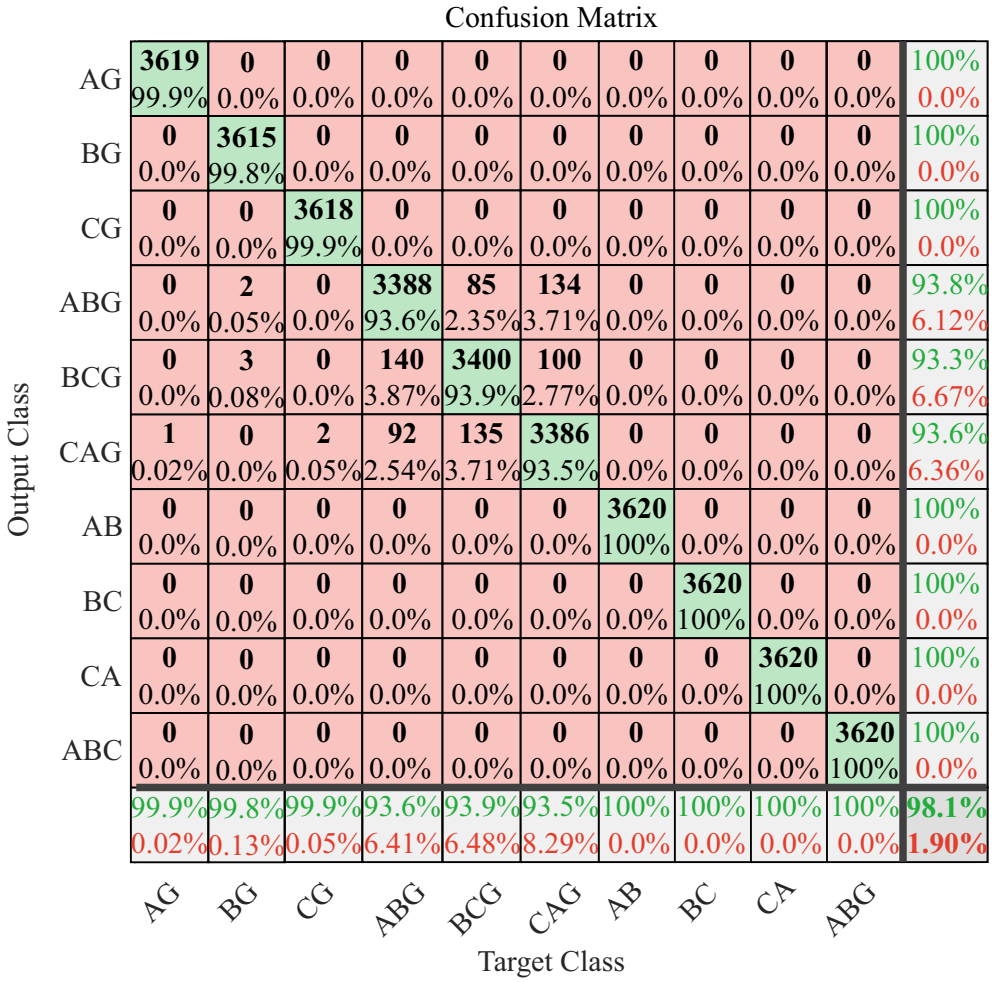

Figure 8.3: Confusion matrix at sample 16 ($\Delta k/16$).

8.1.2 Comparison with a SWT-based Fault Classification Method

The performance of the proposed method was compared to the existing fault classification method proposed in (COSTA; SOUZA; BRITO, 2012b), which uses the RT-SWT wavelet coefficient energy of the local currents instead of the RT-BSWT with the Clark transform as proposed in this paper. Therefore, the method in (COSTA; SOUZA; BRITO, 2012b) is exclusively designed to operate based only in the fault-induced transients, whereas the proposed method is based on both fault-induced transients and information from the wavelet border effects. The recommended mother wavelet for the existing classification method is also the db(4).

The method in (COSTA; SOUZA; BRITO, 2012b) was designed to verify in each sample the fault classification during half cycle, after that the real fault classification was provided by means of the most-frequent classification during, whereas the proposed method provided an accurate fault classification in 2.1 ms with no need of the classification in previous sampling times. Figure 8.2(b) presents the cumulative frequency of the classification method in (COSTA; SOUZA; BRITO, 2012b) considering all AG, AB, ABG, and ABC faults in Table 8.1.

The existing method achieved a fast and high accuracy fault classification for AG and AB faults, whereas the fault classification for ABG and ABC faults never reached an accuracy higher than 50% because this method is not sensible to damped transients. Figure 8.12 depicts the confusion matrix at 8.3 ms for the method in (COSTA; SOUZA; BRITO, 2012b), where the

success rate was 76.1%, whereas the proposed method achieved 100% at 2.1 ms as aforementioned.

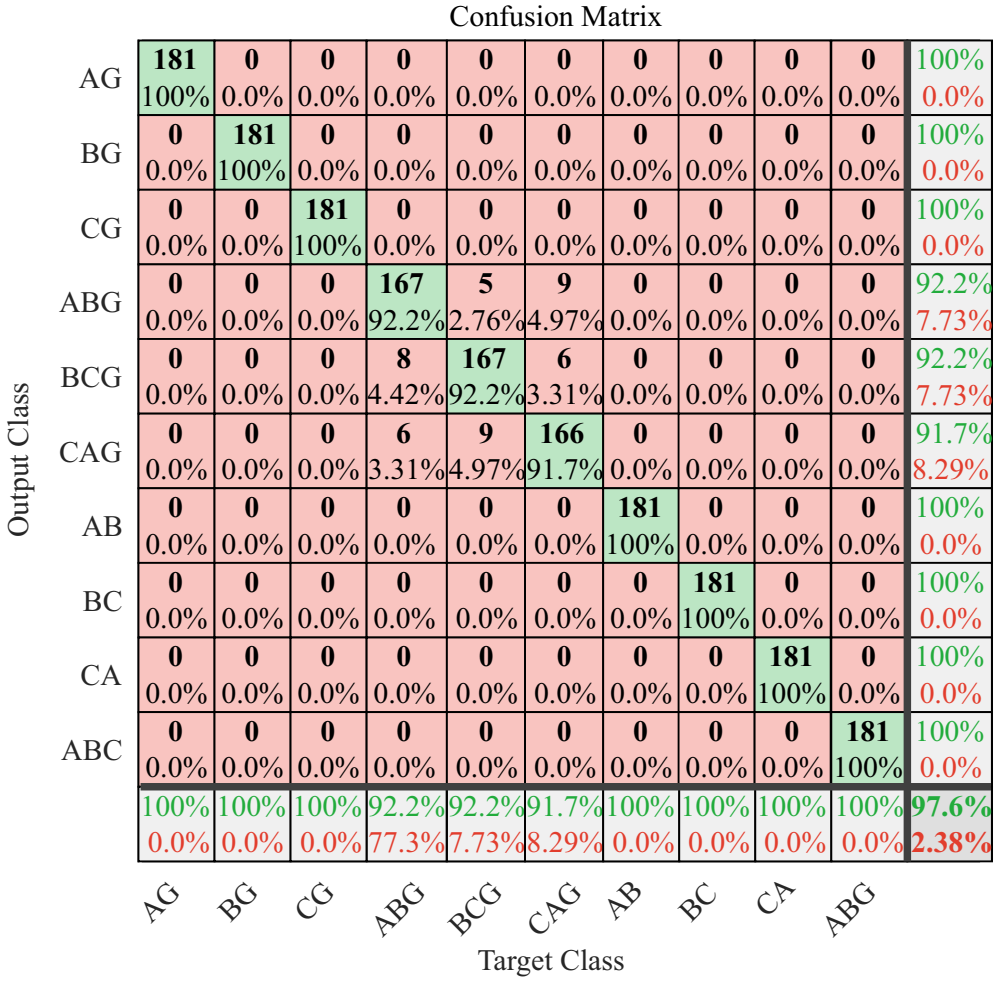

Figure 8.4: Confusion matrix to the fault classifier proposed by (COSTA; SOUZA; BRITO, 2012b).

8.1.3 Mother Wavelet

The performance of wavelet-based methods usually depends on the selected mother wavelet. However, as extensively evaluated in (COSTA, 2014a; MEDEIROS; COSTA; SILVA, 2016; COSTA; DRIESEN, 2013), the fault detection based on the RT-BWT wavelet coefficient energy is scarcely affected by the mother wavelet due to the border distortions, which were designed to provide additional information of the fault. Regarding the fault classification, the same results of 100% of success rate at 2.1 ms were obtained through the db(4) and the db(30). The db(4) mother wavelet is selected because it is one of the most used mother wavelet in fault diagnosis methods and it is the most compact, which lead to a low-computational burden.

8.1.4 Noise Effect

Noise is a relevant parameter to be evaluated since the energy of fault-induced transients can be very low, depending on the fault type and on the inception angle of the fault (COSTA;

SOUZA; BRITO, 2012a). As such, noise can present a challenge to fault detection and hence the fault classification. A total of 5430 fault cases were performed at the middle of the line with fixed fault resistance (r_f = 1 Ω) and varying the fault inception angle θ_f={0,1,2,...,180}°. The proposed method achieved 100% of accuracy under the typical SNR in transmission lines of 60 dB. The SNR of 50 dB and 40 dB were also used and the proposed method presented an accuracy of 97.02% and 75%, respectively.

8.1.5 High Sampling Frequency

The proposed method can properly work at different sampling frequencies. For instance, sampling frequencies of $f_s = 100$ kHz and of $f_s = 15.36$ kHz were used for faults at the middle of the line. All fault cases were correctly classified at 2.1 ms for both cases.

8.1.6 Effect of the Fault Inception Angle

The main challenge faced by fault classification methods based on high-frequency components is the fault inception angle. Based on (COSTA; SOUZA; BRITO, 2012a), by considering only the fault-induced transient information, SLG and LL faults, starting near the faulted voltage-zero crossing, present dumped transients which may lead to an incorrect fault detection and classification. Besides, there are specific fault inception angles in which DLG and LLL faults may be missclassified as LL faults.

Figure 7.2(c) depicts the energy coordinates of the faults used to evaluate the effects of θ_f as described in Table 8.1. Only energy coordinates at 2.1 ms from the fault inception time ($\mathscr{E}_A^{\alpha}(32)$, $\mathscr{E}_B^{\alpha}(32)$, $\mathscr{E}_C^{\alpha}(32)$, and $\mathscr{E}^0(32)$) are depicted in this figures, i.e., each fault is represented by just one energy point. This pattern is going to be followed on the remains effects listed in 8.1.

The energy coordinates $\mathscr{E}_A^{\alpha}$, $\mathscr{E}_B^{\alpha}$, $\mathscr{E}_C^{\alpha}$, and $\mathscr{E}^0$ are composed of high-frequency transient information of the fault as well as additional information due to the border effects. This allows the proposed method to overcome problems associated to the fault inception angle, leading to a success rate of 100%. Indeed, according to Figure 7.2(c), the energy coordinates were properly placed in well-distinct regions in accordance with the fault type regardless of the fault inception angle, where:

- SLG faults are in the middle of each edge at the internal triangles, and at the top of the 3D triangle.
- LL faults are at the bottom, but concentrated at the middle of each edge of the 3D triangle. The zero component is not exactly zero due to the power system unbalance and noise.
- DLG faults are inside each internal triangle in a circular patter according to the fault inception angle value.
- LLL faults are fixed in the bottom of the 3D triangle in a circular pattern according to the fault inception angle value.

8.1.7 The Effect of the Fault Distance

The more distant the fault occurs from the measurement bus, the more damped are the transients. This is a challenge to fault detection and classification. However, according to Figure 8.5, all energy points were placed at the expected positions regardless the distance. Therefore, the proposed fault classifier provided an accuracy of 100% in 2.1 ms for all 5430 fault cases. However, faults near the measured bus were classified at the highest speed, achieving 100% in 1.0 ms to all faults, because the grounding information arrived faster.

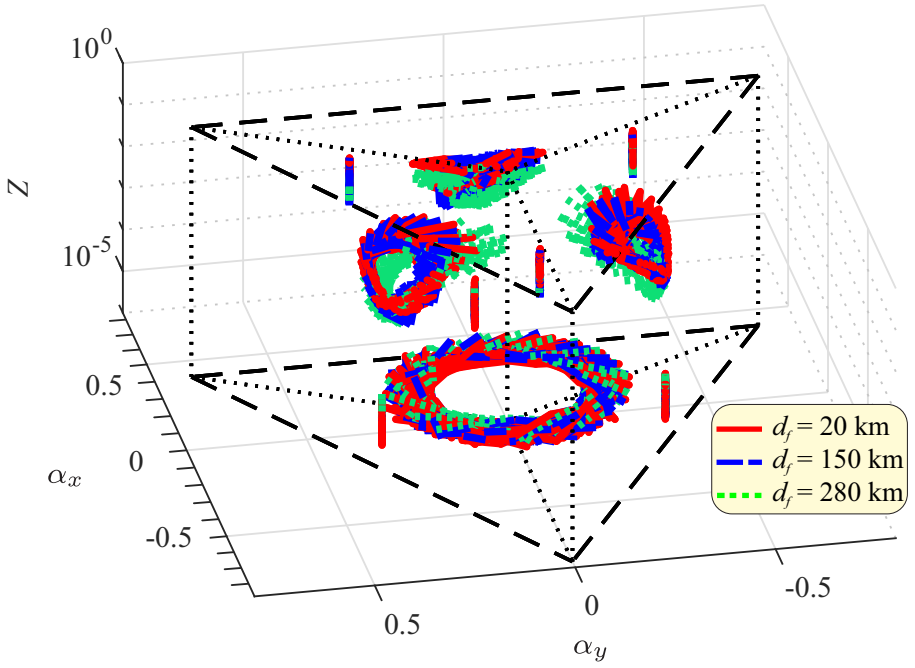

Figure 8.5: The effect of distance.

Additional 1810 faults at the measured bus were simulated in order to evaluate the zone covered by the proposed fault classification range and evaluate whether successive reflections and refractions of traveling waves would be a problem to the proposed method. However, all faults were correctly classified due to the border effects of the RT-BSWT, which also takes into account the current growth leading to a correct classification even if the high-frequency information is compromised. 1810 faults were also performed at the remote bus with 100% accuracy in the fault classification.

8.1.8 The Effect of the Fault Resistance

The higher the fault resistance is, the smaller the overcurrent and travelling wave magnitude of the faulted current are. Nevertheless, the fault resistances to the ground or between phases did not influence the disposition of the alpha and zero components throughout the 3D triangle depicted in Figures 8.6 and 8.7. Therefore, the proposed method was accurate in classifying the fault in 2.1 ms.

8.1.9 The Effect of Series-Compensated Line

Series-compensated lines are widely present in power systems in order to improve the stability margins, reduce the transmission losses, damp sub-synchronous oscillation, and minimize voltage sags during severe disturbances (ANDERSON; ANDERSON, 1999). However, the compensation of lines can cause voltage and current inversions, the steady-state current increases and may contain non-fundamental components. Nonetheless, within 2.1 ms, the proposed method provided a 100% success in series-compensated lines (by using only capacitors in series with the lines). Result are given in Figure 8.8.

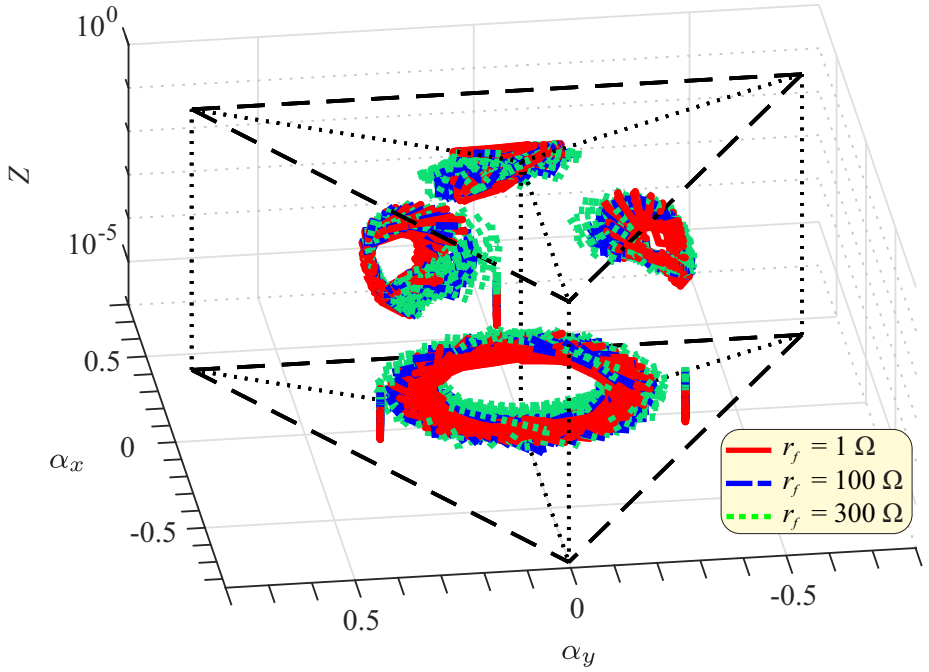

Figure 8.6: The effect of fault resistance between phases to AB, BC, CA, ABG, BCG, and CAG.

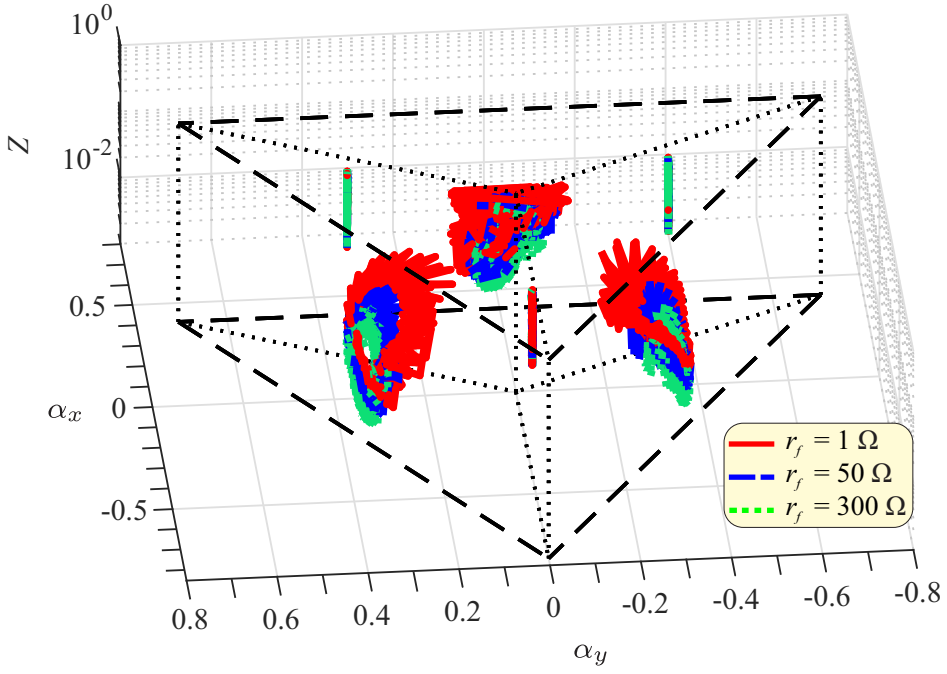

Figure 8.7: The effect of grounding fault resistance to AG, BC, CG, ABG, BCG, and CAG.

8.1.10 The Effect of Power System Loading

The angle difference of between the two sources (δ) defines the power system loading. As shown in Figure 8.9, the proposed method presented a 100% of success rate in the fault

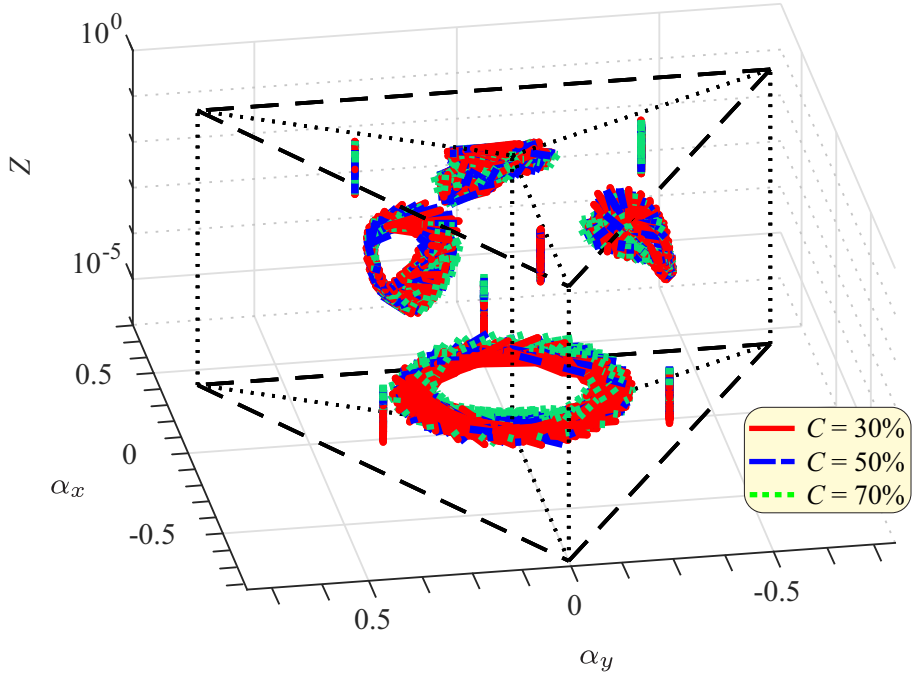

Figure 8.8: The effect of series compensation of line.

classification at 2.1 ms even with changes in the power system loading. However, the fault classification achieved the accuracy of 99.88% at 1 ms.

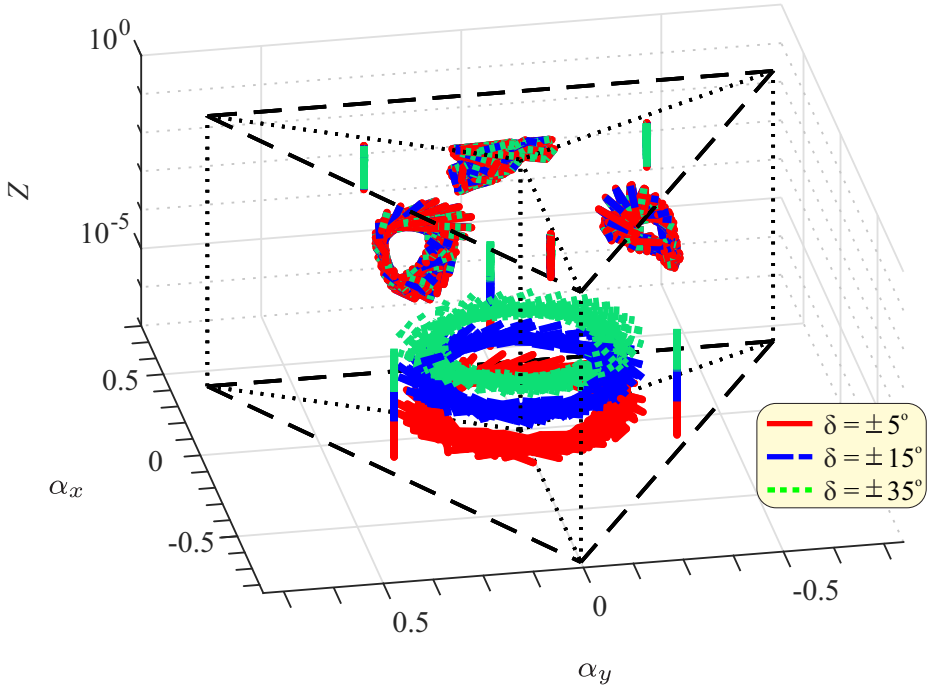

Figure 8.9: The effect of power system loading.

8.1.11 The Effect of Source Strength

The system-to-line impedance ratio (*SIR*) defines the sources strength. SIR_L and SIR_R refer to local and remote sources, respectively. The fault classification offered a 100% success rate at 2.1 ms, as shown in Figure 8.10.

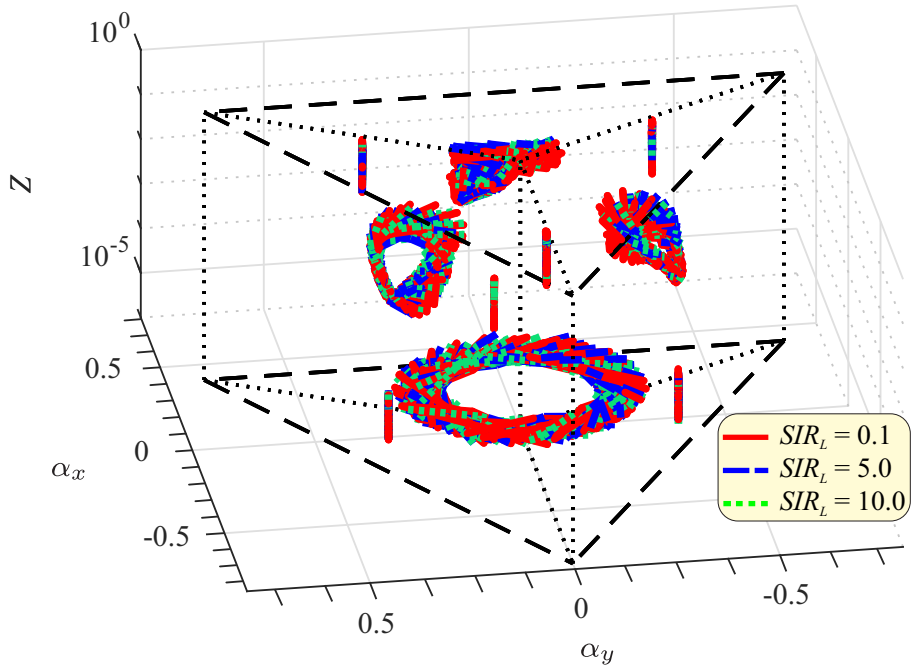

Figure 8.10: The effect of sources strength.

8.1.12 Remote Line

In order evaluate the proposed classifier under faults located in a remote line (TL2), 1810 faults were performed to prove the reliability of the proposed fault classifier to be used as an activator for the proposed directional classifier. As presented in Figure 8.11, the general behavior follows the same pattern decried in the previous chapter. Therefore, all evaluated cases were classified correctly by the classifier.

8.1.13 Evolving Faults

Evolving faults can occur when the system conditions allow for a fault situation to turn into a more challenging one. These events usually occur when the protection system fails or takes too long to operate. Therefore, the fault classification needs to identify correctly the fault type when it changes. Some evolving faults were studied in the 500-kV power system at a fault distance of $d_f = 150$ km, fault resistance of $r_f = 1\ \Omega$, and the fault inception angle varying between $0° \leq \theta_f \leq 180°$ at steps of 10°. The primary faults were AG, AG, BG, BG, CG, CG, AB, BC, and CA. After one cycle, these faults evolved to ABG, CAG, ABG, BCG, BCG, CAG, ABC, ABC and ABC, respectively. A total of 114 evolving faults were evaluated, and the proposed fault classification method provided a success rate of 99.12% in 2.1 ms after the fault evolved, as shown in Figure 8.12.

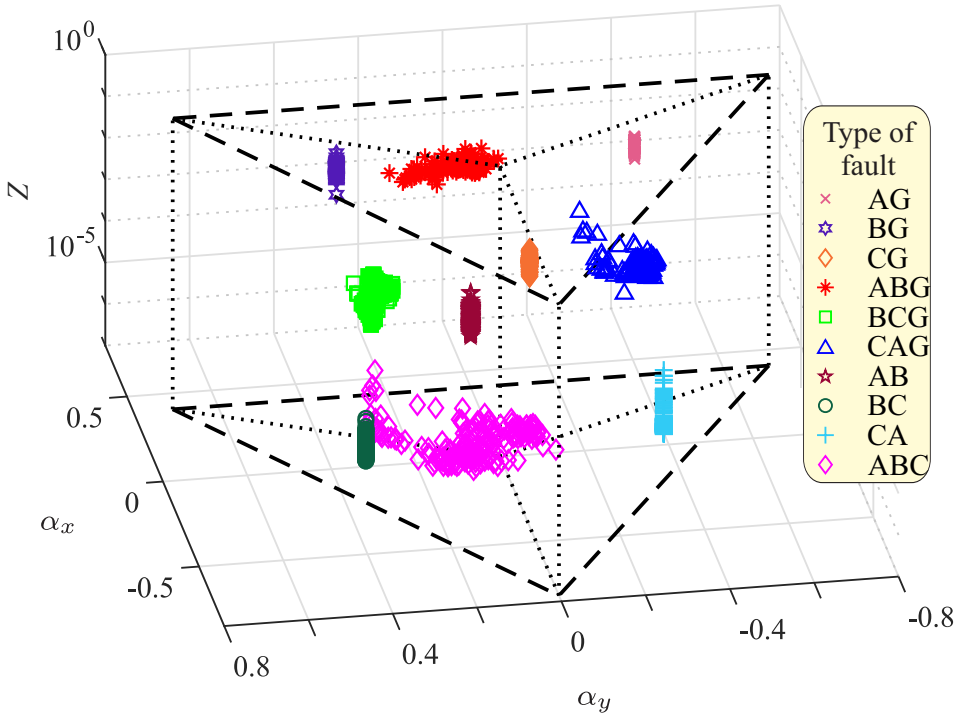

Figure 8.11: Faults performed at remote line.

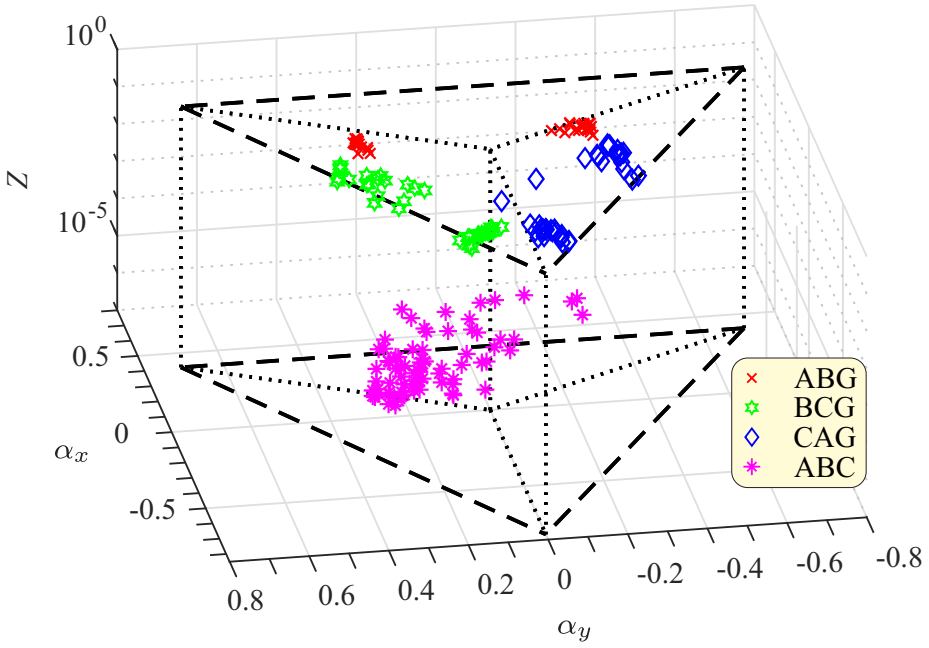

Figure 8.12: The effect of evolving faults.

8.1.14 Alternative Transmission System

In order to demonstrate the robustness of the proposed method, faults were also considered in an alternative transmission system with three lines as presented in Figure 8.13 (França et al.,

2020). The 230 kV alternate system presents lines modeled with frequency-dependency parameters, the lines are 200 km each and the CT and CCVT used is described in (COMMITTEE et al., 2004) and (CARVALHO; FREIRE; DE OLIVEIRA, 2009), respectively. The SIR considered was 0.1 and the power loading angle was -15°, which corresponds to a moderate power system loading. 1800 faults were simulated by using the alternative transients program (ATP) at a sampling frequency of 153600 Hz at TL2. The faults were performed varying the fault inception angle between $1^\circ \geq \theta_f \geq 180^\circ$, the fault resistance was 10 Ω and the fault distance was 100 km from the relay at Bus 2. The fault classifier achieved accuracy of 94.45% at 2.1 ms by using the same threshold previous used, the fault distribution can be seen in Figure 8.14. The misclassifications were among the DLG faults. In fact, the remaining fault types achieve 100% success rate since 1.0 ms, as presented in Figure 8.15(a). The 100% to all fault type are guaranteed in 4.2 seconds, as depicted in Figure 8.15(b). Given this high success rate, confidence is obtained that the proposed method can be used in transmission systems with different parameters without fulfill modifications in the proposed method. In any case the factor of flexibility ρ, and the η_0 may be adjusted for each system in order to accomplished earlier the success rate of 100%.

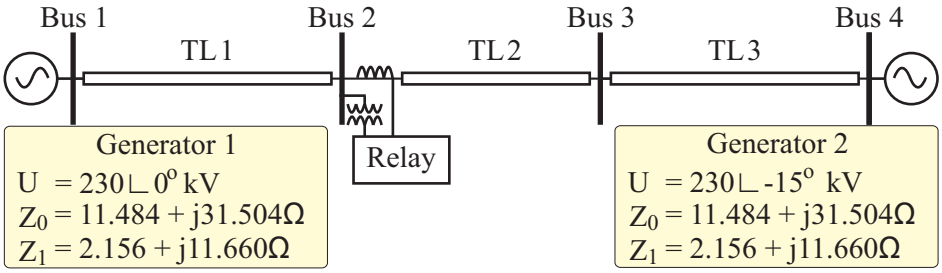

Figure 8.13: Alternated modeled system with distributed parameters.

8.1.15 Study of Case with Actual Data

The proposed fault classifier was evaluated by using three real fault cases depicted in Figure 8.16 from a transmission power system. The faults were correctly classified within the expected time of 2.1 ms. The first sample after the fault being detected and the follows 32 samples were illustrated in Figure 8.17 to each fault. The faults converged to the expected regions on the 3D triangle which lead to the correctly classification.

8.1.16 Computational Efficiency

The wavelet-based fault classifier was implemented in a floating-point digital signal processor (DSP) TMS230F28335 in order to verify its applicability in real-time applications. The overall computational burden to all units was about 6.8 μs, being much less than a sampling period of 65.1 μs = $1/f_s$, as presented in Figure 8.18. This demonstrates the low complexity of the proposed method. It can be well implemented in association with other methods that require a fast fault classification.

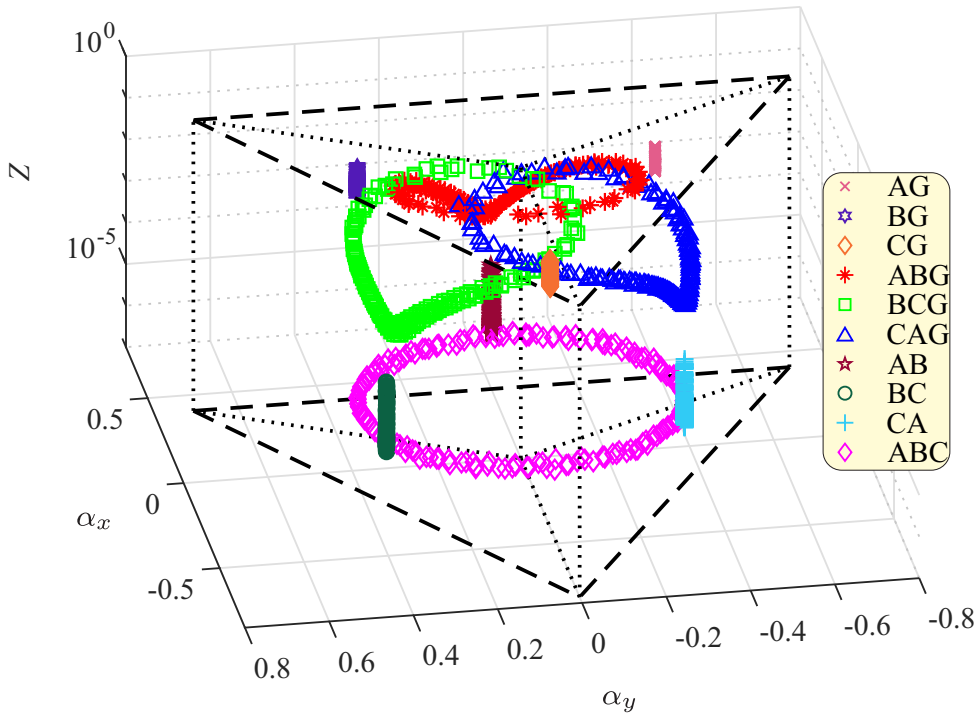

Figure 8.14: Fault distribution at sample 32.

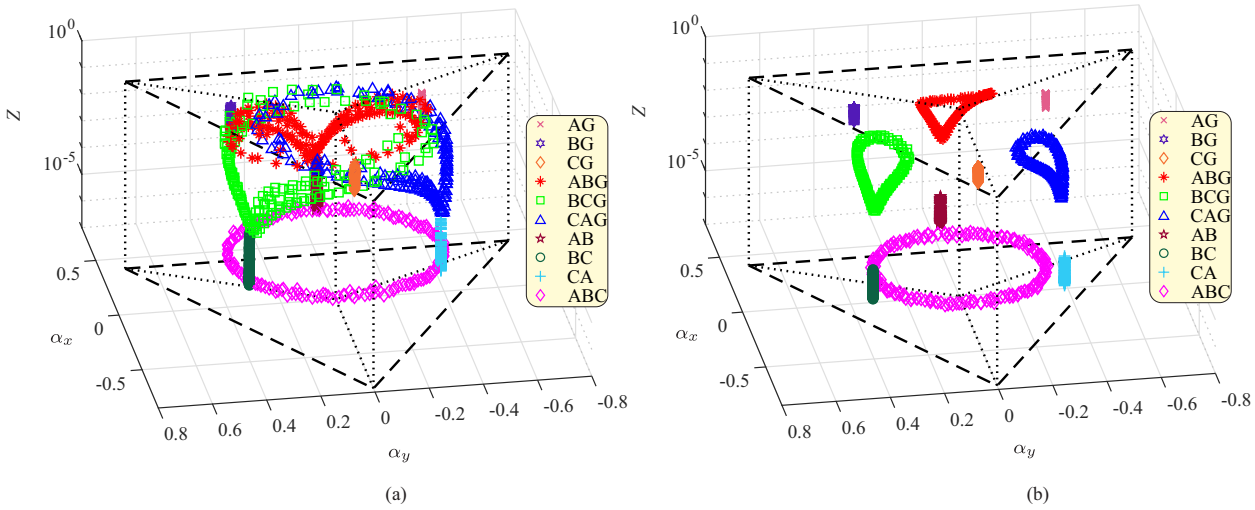

Figure 8.15: Fault distribution: (a) sample 16; (b) sample 64.

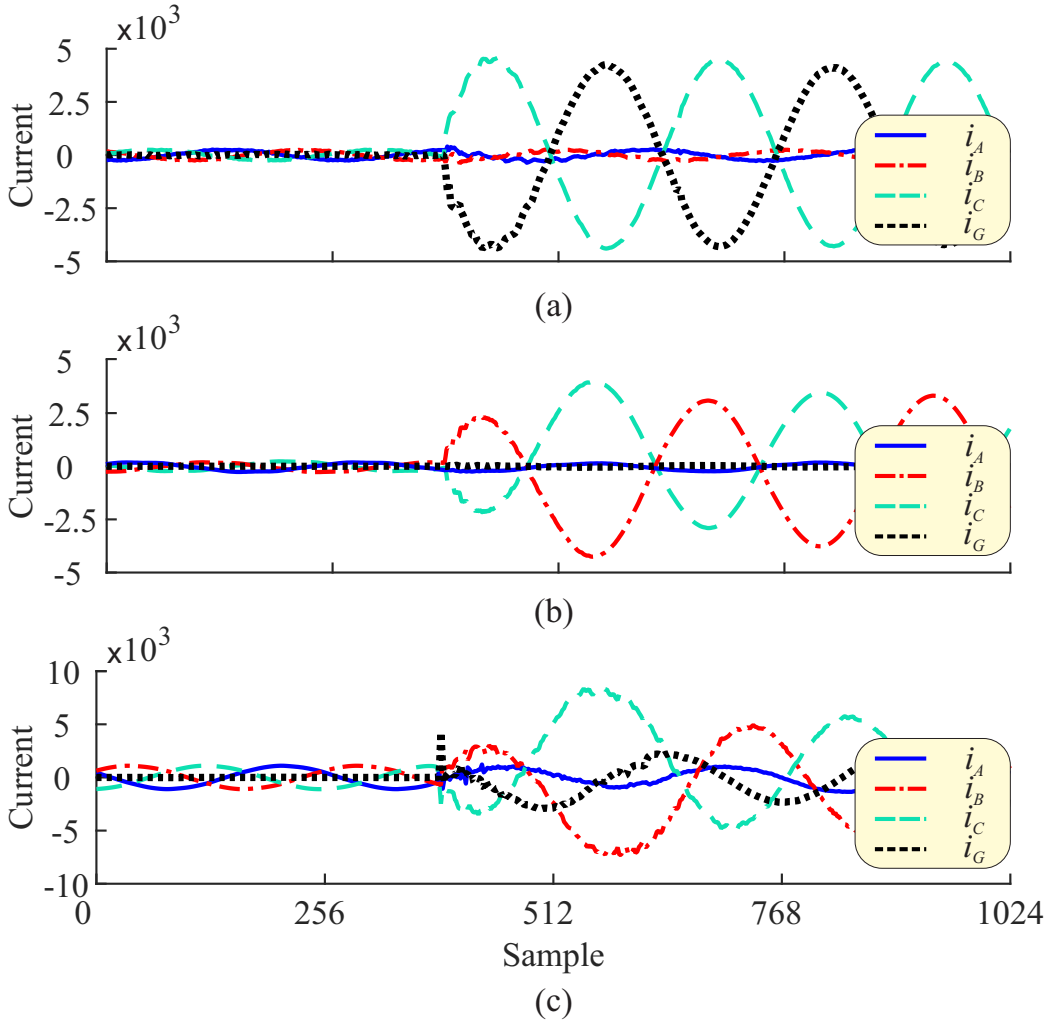

Figure 8.16: Currents from faults occurrence in a real power system: (a) fault CG; (b) fault BC; (c) fault BCG.

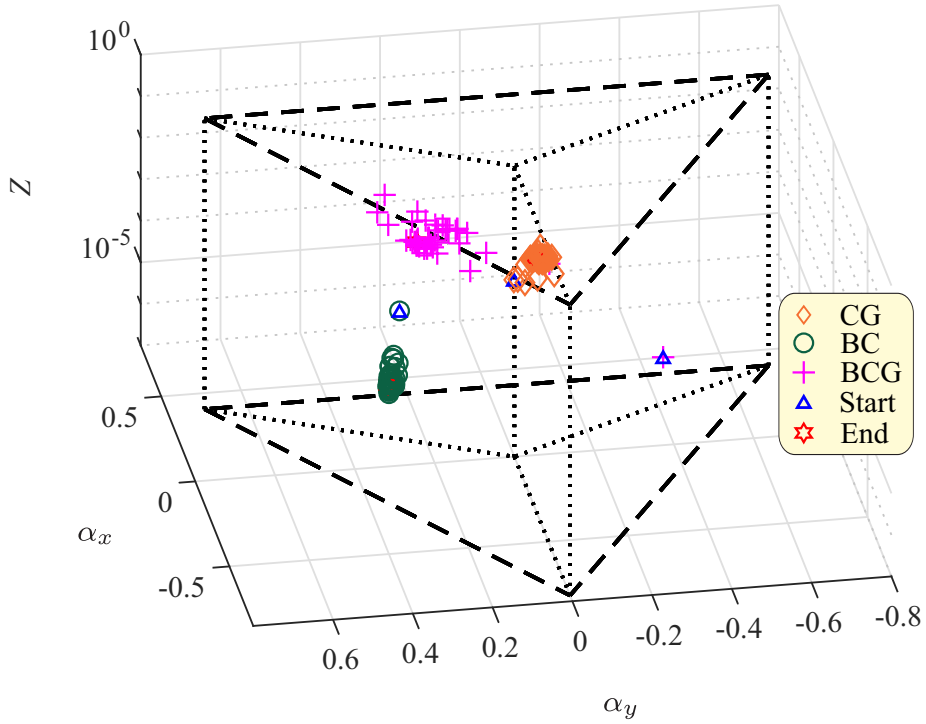

Figure 8.17: Case study of real fault cases.

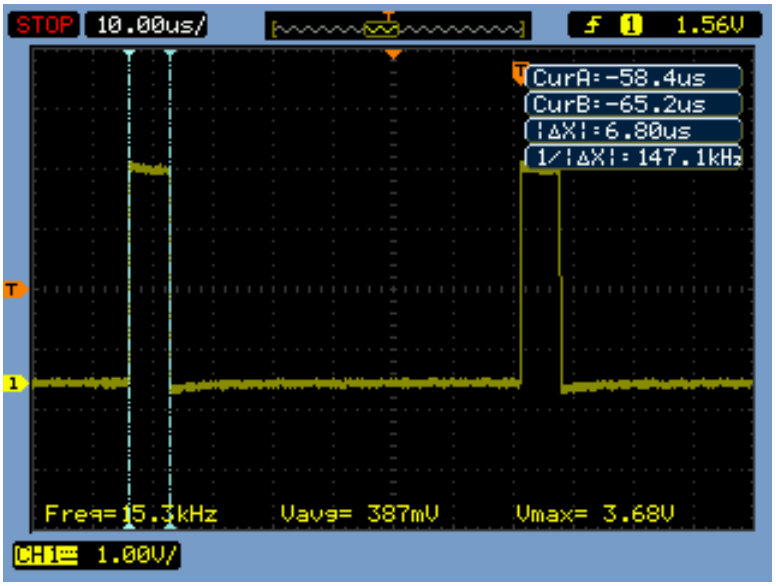

Figure 8.18: Fault classifier computational efficiency.

8.2 Summary

The proposed fault classifier based on wavelet coefficient energies of the real-time stationary wavelet transform with border effects and modal components from the Clarke transform was extensively tested. More than 36.000 faults were simulated considering different conditions to evaluate the proposed method which has proved to be reliable and fast by achieving a success rate of 100% within 2.1 ms to all tested fault cases. An alternated system and real fault cases were used to prove the reliability of the proposed method.

Chapter 9

Conclusions

9.1 General Conclusions

A directional overcurrent protection was developed based on real-time stationary wavelet transform which allowed to recreate the classical directional logic of the phase, positive, negative and zero sequence units. The instantaneous and time-delay overcurrent units were implemented through the scaling coefficients energy. Additional high frequency information provided by the wavelet transform is useful in detecting fault transients and used as activators of proposed directional units. The phase selection necessity was highlighted through the text leading to the development of a fault classifier based on real-time boundary stationary wavelet transform.

A deep evaluation of the directional overcurrent protection was made at 230 kV system of the IEEE for various fault situations, single line-to-ground, double line-to-ground, line-to-line and three-phase faults, to forward and reverse (backward) faults with different fault distance, resistance and inception angles. For all evaluations, the wavelet-based method was compared with the classical method to validate the results. The proposed directional protection was less influenced by the evaluated fault parameters and provided 100% of success rate with the best operating time (by combining all directional units) to all analysed faults. Therefore, the proposed method presented the best performance and the fastest directional operating time.

The best mother wavelet applied to the method was evaluated and good results were found to all mother wavelets analysed. However, longer mother wavelet add delays to detection which lead to suggest the shortest, the mother wavelet Haar, followed by Daubechies with four coefficients, the most commonly used in power systems.

As additional capability, the proposed wavelet-based negative sequence units presented a reliable and fast directionality to ABC faults, even under severe voltage sags, which is not possible with the conventional one. The Fourier-based directional protection solves this problems through memory strategies, for instance. Therefore, memory strategy was implemented in both proposed and conventional methods and the performance and operating time were similar.

Evaluation about the effect of transients in the wavelet activators was also accomplished. Although, transients provided from a capacitor switching or lightning can activate the wavelet trigger, the transients are not enough to sensitize the directional protection. Therefore, the system will not be susceptible to a false trip by adding this new activator.

It was demonstrated that the directional functions (proposed and conventional) are very accurate even in critical faults where the overcurrent protection fails, such as in a distribution system with distributed generation, and in cases of high-resistance faults. Therefore, protections can use the directional information even in critical situations.

The proposed method was implemented in a hardware and presented the lowest computational burden. Therefore, the proposed directional protection has been proved to be practicable for numerical relays.

A real-time fault classification method using the wavelet coefficient energies of the stationary wavelet transform with border effects and modal components from the Clarke transform was proposed, developed and tested. Based on a SWT-based classifier, the proposed method was developed to offer a faster and accurate fault classifier to support the correctly choice of the the proposed directional protection units and to provide a reliable wavelet activator.

More than 36.000 simulated faults were used to evaluate the robustness of the proposed method considering different conditions. The proposed method is simple and robust because it does not require artificial intelligence and the main thresholds are fixed values for any power system, with no need of user settings. The threshold were mathematically computed based on the fault boundary conditions.

Regarding the computational burden, only few operations of addition and multiplication are required. Therefore, considering its fast operation time, its high accuracy, its simplicity, and its low computational burden, the proposed method is ideal to support not only the proposed directional protection but also other fast protections functions or real-time running methods.

The proposed method was extensively assessed in order to prove its reliability under different conditions, such as: fault inception angles, fault distance, fault resistance, close-in faults, remote faults, series-compensation line, power system loading, and source strength. The proposed method was robust enough to be applied to different transmission systems and to classify evolving faults because the main thresholds do not change according to a straightforward logic regardless the power system parameters.

The proposed method presented a reliable and fast fault classification with success rate of 100% within 1.0 ms in single line-to-ground, line-to-line, and three-phase faults and within 2.1 ms in double line-to-ground faults. Moreover, the proposed method was compared to an existing SWT-based method, which was reproduced in this work. The proposed fault classifier was proved to be faster and more reliable than the SWT-based method.

9.2 Future Works

The following topics are addressed as continuity of this thesis:

1. Evaluate the fault classifier by using some artificial intelligence to identify if the fault classifier can be even faster.

2. Extend the proposed directional method to the use of Clarke components to avoid delay inherent to the symmetrical component tool.

3. Investigate if the directionality could be identified by using the high-frequency information from RT-BSWT in order to be used in the context of traveling waves.

4. Evaluate three-phase faults containing zero component, in order to adequate the proposed fault classifier to support them, perhaps by the use of beta components.

5. Evaluate the frequency variation effect to both directional and classifier methods.

6. Investigate if the proposed directional method could be able to properly operate in a system with different contribution of renewable sources.

7. Simplify the proposed fault classifier to a unit selector in order to offer faster fault diagnosis to protection methods demanding only a unit selector.

9.2.1 Publications

The publications referent to this work are present in Table 9.1.

Table 9.1: Publication until now.

Journal/Event	Title	Authors
International Journal of Electrical Power and Energy Systems (IJEPES) - 2019	Improved Traditional Directional Protection by Using the Stationary Wavelet Transform	M. M. Leal, F. B. Costa, J. T. L. S. Campos
3rd Workshop on Communication Networks and Power Systems (WCNPS), 2018 Brasília	Assessment of Wavelet-based Directional Overcurrent Protection Applied in a Distribution System with Doubly-fed Induction Generators	M. R. Marques, M. M. Leal, F. B. Costa and L. S. Barros

Bibliography

ABDELGAYED, T. S.; MORSI, W. G.; SIDHU, T. S. A new harmony search approach for optimal wavelets applied to fault classification. *IEEE Transactions on Smart Grid*, v. 9, n. 2, p. 521–529, March 2018. ISSN 1949-3053.

ABU-RUB, H.; MALINOWSKI, M.; AL-HADDAD, K. *Power electronics for renewable energy systems, transportation and industrial applications*. [S.l.]: John Wiley & Sons, 2014.

AGUILERA, C.; ORDUNA, E.; RATTA, G. Directional traveling-wave protection based on slope change analysis. *IEEE Transactions on Power Delivery*, v. 22, n. 4, p. 2025–2033, Oct 2007. ISSN 0885-8977.

ALVES, D. K. et al. Real-time power measurement using the maximal overlap discrete wavelet-packet transform. *IEEE Trans. Ind. Electron.*, v. 64, n. 4, p. 3177–3187, April 2017. ISSN 0278-0046.

ANDERSON, P. M.; ANDERSON, P. Power system protection. McGraw-Hill New York, 1999.

ASHOK, V.; YADAV, A.; ABDELAZIZ, A. Modwt-based fault detection and classification scheme for cross-country and evolving faults. *Electr. Power Syst. Res.*, v. 175, p. 105897, 2019. ISSN 0378-7796. Disponível em: <http://www.sciencedirect.com/science/article/pii/S0378779619302160>.

AUDLIN, L. J.; WARRINGTON, A. R. V. C. Distance relay protection for subtransmission lines made economical. *Electrical Engineering*, v. 62, n. 9, p. 574–578, Sept 1943. ISSN 0095-9197.

BHALJA, B.; MAHESHWARI, R. P. Wavelet-based fault classification scheme for a transmission line using a support vector machine. *Electric Power Components and Systems*, Taylor & Francis, v. 36, n. 10, p. 1017–1030, 2008.

BISWAL, M.; PATI, B. B.; PRADHAN, A. K. Directional relaying for double circuit line with series compensation. *IET Generation, Transmission & Distribution*, IET, v. 7, n. 4, p. 405–413, 2013.

BLACKBURN, J. L. *Symmetrical components for power systems engineering*. [S.l.]: CRC Press, 1993.

BOLLEN, M. H. J.; GU, I. Y. H. On the analysis of voltage and current transients in three-phase power systems. *IEEE Transactions on Power Delivery*, v. 22, n. 2, p. 1194–1201, April 2007. ISSN 0885-8977.

BURRUS, C. S.; RAMESH, A. G.; GUO, H. *Introduction to wavelets and wavelet Transforms*. New Jersey, USA: Prentice Hall, 1998.

CARVALHO, A. V.; FREIRE, A. R. F.; DE OLIVEIRA, H. M. Transient interaction between coupling capacitors voltage transformers and transmission lines. In: *2009 IEEE Power Energy Society General Meeting*. [S.l.: s.n.], 2009. p. 1–8.

CHEN, K.; HUANG, C.; HE, J. Fault detection, classification and location for transmission lines and distribution systems: a review on the methods. *High Voltage*, v. 1, n. 1, p. 25–33, 2016. ISSN 2397-7264.

CHEN, W. et al. Study of wavelet-based ultra high speed directional transmission line protection. *IEEE Transactions on Power Delivery*, IEEE, v. 18, n. 4, p. 1134–1139, 2003.

CHRISTIE, R.; DABBAGCHI, I. *30 Bus Power Flow Test Case*. 1993. Disponível em: <www.ee.washington.edu/research/pstca/pf30/pg_tca30bus.htm>.

COHEN, A.; DAUBECHIES, I.; VIAL, P. Wavelets on the interval and fast wavelet transforms. *Applied and computational harmonic analysis*, 1993.

COMMITTEE, I. P. S. R. et al. Emtp reference models for transmission line relay testing. 2004.

COSTA, F. B. Boundary wavelet coefficients for real time detection of transients induced by faults and power quality disturbances. *IEEE Transactions on Power Delivery*, v. 29, n. 6, p. 2674–2687, Dec 2014. ISSN 0885-8977.

COSTA, F. B. Fault-induced transient detection based on real-time analysis of the wavelet coefficient energy. *IEEE Transactions on Power Delivery*, v. 29, n. 1, p. 140–153, Feb 2014. ISSN 0885-8977.

COSTA, F. B.; DRIESEN, J. Assessment of voltage sag indices based on scaling and wavelet coefficient energy analysis. *IEEE Trans. on Power Del.*, v. 28, n. 1, p. 336–346, Jan 2013. ISSN 0885-8977.

COSTA, F. B. et al. Two-terminal traveling-wave-based transmission-line protection. *IEEE Trans. on Power Del.*, v. 32, n. 3, p. 1382–1393, June 2017. ISSN 0885-8977.

COSTA, F. B.; MONTI, A.; PAIVA, S. C. Overcurrent protection in distribution systems with distributed generation based on the real-time boundary wavelet transform. *IEEE Transactions on Power Delivery*, v. 32, n. 1, p. 462–473, Feb 2017. ISSN 0885-8977.

COSTA, F. B.; SOUZA, B. A.; BRITO, N. S. D. Effects of the fault inception angle in fault induced transients. *IET generation, transmission and distribution*, v. 6, n. 5, p. 463–471, 2012.

COSTA, F. B.; SOUZA, B. A.; BRITO, N. S. D. Real-time classification of transmission line faults based on maximal overlap discrete wavelet transform. In: *PES T D 2012*. [S.l.: s.n.], 2012. p. 1–8. ISSN 2160-8563.

COSTA, F. B. et al. Real-time detection of transients induced by high-impedance faults based on the boundary wavelet transform. *Trans. Ind. Appl.*, v. 51, n. 6, p. 5312–5323, Nov 2015. ISSN 0093-9994.

COSTA, F. B.; SOUZA, B. A. D.; BRITO, N. S. D. Detection and classification of transient disturbances in power systems. *IEEJ Transactions on Power and Energy*, v. 130, p. 910–916, 2010.

COURY, D. V. *Um estimador ótimo aplicado à proteção digital dos sistemas elétricos de potência*. Dissertação (Mestrado) — Escola de Engenharia de São Carlos, Universidade de São Paulo, 1987.

DAS, J. C. *Power system analysis: short-circuit load flow and harmonics*. [S.l.]: CRC press, 2016.

DAUBECHIES, I. Ten lectures on wavelets. In: *CBMS-NSF Regional Conference Series, Siam*. [S.l.: s.n.], 1992.

DONG, X.; KONG, W.; CUI, T. Fault classification and faulted-phase selection based on the initial current traveling wave. *IEEE Transactions on Power Delivery*, v. 24, n. 2, p. 552–559, April 2009. ISSN 0885-8977.

EISSA, M. A novel digital directional transformer protection technique based on wavelet packet. *IEEE Transactions on Power Delivery*, IEEE, v. 20, n. 3, p. 1830–1836, 2005.

EISSA, M.; MAHFOUZ, M. New high-voltage directional and phase selection protection technique based on real power system data. *IET Generation, Transmission & Distribution*, IET, v. 6, n. 11, p. 1075–1085, 2012.

EISSA, M. M. A novel digital directional technique for bus-bars protection. *IEEE transactions on power delivery*, IEEE, v. 19, n. 4, p. 1636–1641, 2004.

EISSA, M. M. A novel digital directional transformer protection technique based on wavelet packet. *IEEE Transation on Power Delivery*, v. 20, n. 3, July 2005. ISSN 0885-8977.

FORTESCUE, C. L. Method of symmetrical co-ordinates applied to the solution of polyphase networks. *Transactions of the American Institute of Electrical Engineers*, IEEE, v. 37, n. 2, p. 1027–1140, 1918.

FOURIER, J. B. J. B. *The analytical theory of heat*. [S.l.]: The University Press, 1878.

França, R. L. et al. Traveling wave-based transmission line earth fault distance protection. *IEEE Transactions on Power Delivery*, p. 1–1, 2020.

GAO, R. X.; YAN, R. *Wavelets: Theory and applications for manufacturing*. [S.l.]: Springer Science & Business Media, 2010.

GLOVER, J. D.; SARMA, M. S.; OVERBYE, T. *Power System Analysis & Design, SI Version*. [S.l.]: Cengage Learning, 2012.

GRAINGER, J. J.; JR., W. D. S. *Power System Analysis*. New York, USA: McGraw-Hill, 1994.

GROSSMANN, A.; MORLET, J. Decomposition of hardy functions into square integrable wavelets of constant shape. *SIAM journal on mathematical analysis*, SIAM, v. 15, n. 4, p. 723–736, 1984.

Guillen, D. et al. Fault detection and classification in transmission lines based on a psd index. *IET Generation, Transmission Distribution*, v. 12, n. 18, p. 4070–4078, 2018. ISSN 1751-8687.

GUZMÁN, A. et al. Traveling-wave and incremental quantity directional elements speed up directional comparison protection schemes. In: *14th International Conference on Developments in Power System Protection*. [S.l.: s.n.], 2018.

HAAR, A. Zur theorie der orthogonalen funktionensysteme. *Mathematische Annalen*, Springer, v. 69, n. 3, p. 331–371, 1910.

HE, Z. et al. Fault detection and classification in ehv transmission line based on wavelet singular entropy. *IEEE Transactions on Power Delivery*, v. 25, n. 4, p. 2156–2163, Oct 2010. ISSN 0885-8977.

IEEE. Ieee standard and american national standard for electrical and electronics diagrams (including reference designation class designation letters). *IEEE 315-1971 (ANSI Y32.2-1970)*, p. 1–92, Nov 1971.

Institute of Electrical and Electronics Engineers. *IEEE Standard Inverse-Time Characteristic Equations for Overcurrent Relays*. [S.l.], 1997.

JAYAMAHA, D.; LIDULA, N.; RAJAPAKSE, A. Wavelet based artificial neural networks for detection and classification of dc microgrid faults. In: IEEE. *2019 IEEE Power & Energy Society General Meeting (PESGM)*. [S.l.], 2019. p. 1–5.

JOHNS, A. T.; SALMAN, S. K. *Digital protection for power systems*. [S.l.]: IET, 1997.

JONES, D.; KUMM, J. J. Future distribution feeder protection using directional overcurrent elements. *IEEE Transactions on Industry Applications*, v. 50, n. 2, p. 1385–1390, March 2014. ISSN 0093-9994.

JUNG, C. et al. Wavelet based noise cancellation technique for fault location on underground power cables. *Electric Power Systems Research*, v. 77, n. 10, p. 1349 – 1362, 2007. ISSN 0378-7796. Disponível em: <http://www.sciencedirect.com/science/article/pii/S0378779606002495>.

KASZTENNY, B. et al. Fast ground directional overcurrent protection - limitations and solutions. *27th Annual Western Protective Relay Conference*, p. 22, October 2000.

KHAN, U. N.; SIDHU, T. S. A phase-shifting transformer protection technique based on directional comparison approach. *IEEE Transactions on Power Delivery*, v. 29, n. 5, p. 2315–2323, 2014.

KONG, Y.; ZHANG, B.; HAO, Z. Study of ultra-high-speed protection of transmission lines using a directional comparison scheme of transient energy. *IEEE Transactions on Power Delivery*, v. 30, n. 3, p. 1317–1322, 2015.

LAHIRI, U.; PRADHAN, A. K.; MUKHOPADHYAYA, S. Modular neural network-based directional relay for transmission line protection. *IEEE Transactions on Power Systems*, v. 20, n. 4, p. 2154–2155, Nov 2005. ISSN 0885-8950.

LEAL, M. M.; COSTA, F. B.; CAMPOS, J. T. L. S. Improved traditional directional protection by using the stationary wavelet transform. *Inter. Journal of Electrical Power & Energy Systems*, Elsevier, v. 105, p. 59–69, 2019.

LIANG, J.; ELANGOVAN, S.; DEVOTTA, J. A wavelet multiresolution analysis approach to fault detection and classification in transmission lines. *International Journal of Electrical Power & Energy Systems*, v. 20, n. 5, p. 327 – 332, 1998. ISSN 0142-0615.

LIU, Z. et al. Multiwavelet packet entropy and its application in transmission line fault recognition and classification. *IEEE Transactions on Neural Networks and Learning Systems*, v. 25, n. 11, p. 2043–2052, Nov 2014. ISSN 2162-237X.

LUO, S. et al. A directional protection scheme for hvdc transmission lines based on reactive energy. *IEEE Transactions on Power Delivery*, IEEE, v. 31, n. 2, p. 559–567, 2016.

MACKENZIE, D. et al. Wavelets: seeing the forest and the trees. *Beyond Discovery*, p. 1–8, 2001.

MALATHI, V.; MARIMUTHU, N.; BASKAR, S. Intelligent approaches using support vector machine and extreme learning machine for transmission line protection. *Neurocomputing*, v. 73, n. 10, p. 2160 – 2167, 2010. ISSN 0925-2312. Subspace Learning / Selected papers from the European Symposium on Time Series Prediction. Disponível em: <http://www.sciencedirect.com/science/article/pii/S0925231210000822>.

MALIK, H.; SHARMA, R. Transmission line fault classification using modified fuzzy q learning. *IET Generation, Transmission Distribution*, v. 11, n. 16, p. 4041–4050, 2017. ISSN 1751-8687.

MALLAT, S. A theory for multiresolution signal decomposition: the wavelet representation. *Pattern Analysis and Machine Intelligence, IEEE Transactions on*, v. 11, n. 7, p. 674–693, jul 1989. ISSN 0162-8828.

MEDEIROS, R.; COSTA, F.; SILVA, K. Power transformer differential protection using the boundary discrete wavelet transform. *IEEE Trans. on Power Del.*, PP, n. 99, p. 1–1, 2016. ISSN 0885-8977.

MISHRA, P. K.; YADAV, A.; PAZOKI, M. A novel fault classification scheme for series capacitor compensated transmission line based on bagged tree ensemble classifier. *IEEE Access*, v. 6, p. 27373–27382, 2018. ISSN 2169-3536.

MOZINA, C. J. Impact of green power distributed generation. *IEEE Ind. Appl. Mag.*, v. 16, n. 4, p. 55–62, July 2010. ISSN 1077-2618.

MURRAY, R. M. *A mathematical introduction to robotic manipulation*. [S.l.]: CRC press, 2017.

OBEID, N. H. et al. Early intermittent interturn fault detection and localization for a permanent magnet synchronous motor of electrical vehicles using wavelet transform. *IEEE Trans. Transport. Electrific.*, v. 3, n. 3, p. 694–702, Sept 2017.

ONS (Ed.). *Procedimentos de Rede*: Requisitos minímos para os sistemas de proteção, de registro de perturbações e de teleproteção. [S.l.], 2016. Sub-módulo 2.6.

PARIKH, U. B.; DAS, B.; MAHESHWARI, R. Fault classification technique for series compensated transmission line using support vector machine. *International Journal of Electrical Power & Energy Systems*, v. 32, n. 6, p. 629 – 636, 2010. ISSN 0142-0615. Disponível em: <http://www.sciencedirect.com/science/article/pii/S0142061509001938>.

PERCIVAL, D. B.; WALDEN, A. T. *Wavelet methods for time series analysis*. New York, USA: Cambridge University Press, 2000.

PERERA, N.; RAJAPAKSE, A.; MUTHUMUNI, D. Wavelet based transient directional method for busbar protection. In: *Proceedings of the International Conference on Power Systems Transients (IPST2011), Delft, The Netherlands*. [S.l.: s.n.], 2011. p. 14–17.

PEREZ, L. G.; URDANETA, A. J. Optimal coordination of directional overcurrent relays considering definite time backup relaying. *IEEE Trans. on Power Del.*, v. 14, n. 4, p. 1276–1284, Oct 1999. ISSN 0885-8977.

PHADKE, A. G.; IBRAHIM, M.; HLIBKA, T. Fundamental basis for distance relaying with symmetrical components. *IEEE Transactions on Power Apparatus and Systems*, v. 96, n. 2, p. 635–646, March 1977. ISSN 0018-9510.

PHADKE, A. G.; THORP, J. S. *Synchronized phasor measurements and their applications*. [S.l.]: Springer Science & Business Media, 2008.

PHADKE, A. G.; THORP, J. S. *Computer relaying for power systems*. [S.l.]: John Wiley & Sons, 2009.

PINTOS, L. de M.; MORETO, M.; ROLIM, J. G. Applicability analysis of directional overcurrent relay without voltage reference in microgrids. *IEEE Latin America Transactions*, IEEE, v. 14, n. 2, p. 687–693, 2016.

PRASAD, A.; EDWARD, J. B.; RAVI, K. A review on fault classification methodologies in power transmission systems: Part i. *Journal of Electrical Systems and Information Technology*, v. 5, n. 1, p. 48 – 60, 2018. ISSN 2314-7172. Disponível em: <http://www.sciencedirect.com/science/article/pii/S2314717217300065>.

PRASAD, A.; EDWARD, J. B.; RAVI, K. A review on fault classification methodologies in power transmission systems: Part ii. *Journal of Electrical Systems and Information Technology*, v. 5, n. 1, p. 61 – 67, 2018. ISSN 2314-7172. Disponível em: <http://www.sciencedirect.com/science/article/pii/S2314717216300836>.

RAJARAMAN, P. et al. Fault classification in transmission lines using wavelet multiresolution analysis. *IEEE Potentials*, v. 35, n. 1, p. 38–44, Jan 2016. ISSN 0278-6648.

RAVAL, P. D.; PANDYA, A. S. A hybrid pso-ann-based fault classification system for ehv transmission lines. *IETE Journal of Research*, Taylor and Francis, v. 0, n. 0, p. 1–14, 2020.

ROBBA, E. J. *Introdução a sistemas elétricos de potência: componentes simétricas*. [S.l.]: Inst. Nacional do Livro, Ministério da Educação e Cultura, 1973.

ROBERTS, J.; GUZMAN, A. Directional element design and evaluation. In: *proceedings of the 21st Annual Western Protective Relay Conference, Spokane, WA*. [S.l.: s.n.], 1994.

ROBERTS, J. B.; HOU, D. *Adaptive polarizing memory voltage time constant*. [S.l.]: Google Patents, 1998. US Patent 5,790,418.

SALEKI, G.; SAMET, H.; GHANBARI, T. High-speed directional protection based on cross correlation of fourier transform components of voltage and current. *IET Science, Measurement Technology*, v. 10, n. 4, p. 275–287, 2016.

Samet, H. et al. Efficient current-based directional relay algorithm. *IEEE Systems Journal*, v. 13, n. 2, p. 1262–1272, 2019.

SCHWEITZER, E. O. et al. Speed of line protection - can we break free of phasor limitations? In: *68th Annual Conference for Protective Relay Engineers*. [S.l.: s.n.], 2015. p. 448–461.

SCHWEITZER, E. O.; KASZTENNY, B.; MYNAM, M. V. Performance of time-domain line protection elements on real-world faults. In: *2016 69th Annual Conference for Protective Relay Engineers (CPRE)*. [S.l.: s.n.], 2016. p. 1–17.

SILVA, D. M. et al. Wavelet-based analysis and detection of traveling waves due to dc faults in lcc hvdc systems. *Inter. Jour. Elect. Power & Energy Syst.*, v. 104, p. 291–300, 2019. ISSN 0142-0615. Disponível em: <http://www.sciencedirect.com/science/article/pii/S0142061518309888>.

STEINMETZ, C. P. *Theory and calculation of alternating current phenomena*. [S.l.]: McGraw-Hill Book Company, Incorporated, 1916.

STEVENSON, W. D. J. *Elementos de análise de sistemas elétricos de potência*. [S.l.]: McGraw-Hill do Brasil, 1978.

TAVEIROS, F. E. V.; BARROS, L. S.; BEZERRA COSTA, F. Wind turbine torque-speed feature emulator using a dc motor. In: *2013 Brazilian Power Electronics Conference*. [S.l.: s.n.], 2013. p. 480–486.

UKIL, A.; DECK, B.; SHAH, V. H. Current-only directional overcurrent protection for distribution automation: challenges and solutions. *IEEE Transactions on Smart Grid*, IEEE, v. 3, n. 4, p. 1687–1694, 2012.

VALSAN, S. P.; SWARUP, K. Computationally efficient wavelet-transform-based digital directional protection for busbars. *IEEE transactions on power delivery*, IEEE, v. 22, n. 3, p. 1342–1350, 2007.

WANI, R. P. S. N. S. A novel approach for the detection, classification and localization of transmission lines faults using wavelet transform and support vector machines classifier. *International Journal of Engineering & Technology*, v. 7, n. 2.17, p. 56–62, 2018. ISSN 2227-524X.

YANG, L. et al. Optimal controller design of a doubly-fed induction generator wind turbine system for small signal stability enhancement. *IET Generation, Transmission Distribution*, v. 4, n. 5, p. 579–597, 2010.

YOUSSEF, O. A. A modified wavelet-based fault classification technique. *Electric Power Systems Research*, v. 64, n. 2, p. 165 – 172, 2003. ISSN 0378-7796.

YOUSSEF, O. A. Combined fuzzy-logic wavelet-based fault classification technique for power system relaying. *IEEE Transactions on Power Delivery*, v. 19, n. 2, p. 582–589, April 2004. ISSN 0885-8977.

ZAYED, A. I. *Advances in Shannon's sampling theory*. [S.l.]: CRC press, 1993.

ZIEGLER, G. *Numerical distance protection: principles and applications*. 2. ed. São Paulo: John Wiley & Sons, 2011.

ZIN, A. A. M. et al. New algorithm for detection and fault classification on parallel transmission line using dwt and bpnn based on clarke transformation. *Neurocomputing*, v. 168, p. 983 – 993, 2015. ISSN 0925-2312. Disponível em: <http://www.sciencedirect.com/science/article/pii/S0925231215006669>.

Appendix A

Power System

The parameters related to IEEE 30 bus power system and the doubly-fed induction generator (DFIG) are described in this Appendix.

A.1 Data from IEEE 30 Bus Power System

The IEEE 30 bus test system is a portion of the American Electric Power System located in the Midwestern at United State of America in August 20th, 1993 (CHRISTIE; DABBAGCHI, 1993). Its original topology is depicted in the Figure A.1 and its database was provided by AEP and entered in IEEE Common Data Format by the University of Washington. The data provided by IEEE is summarized in Figures A.2 and A.3.

Each bus on the system was associated with a number and name. The type provided by the third column in the Figure A.2, is defined according with the following code:

- 0 - Unregulated (load, PQ);
- 1 - Hold MVAR generation within voltage limits, (PQ);
- 2 - Hold voltage within VAR limits (gen, PV);
- 3 - Hold voltage and angle (swing, V-Theta).

The generators are located at the Bus 1 (Glen Lyn) and Bus 2 (Clayort). The present system do not possess any remote controlled bus or any shunt conductance. The MVA Base is 100 and the data was collected during winter season.

The first and second columns at Figure A.3 represent, respectively, the the non-unity tap side and the device impedance side, for ether transformers or phase shifters. The follows third and fourth columns depict the concentrated branches resistances and reactances. The line charging B is presented in column five and the last column shows the transformer tap ratio. All the lines are single transmission lines.

Based on the concentrated parameters, the distributed parameters were computed as presented in Table A.1, and the lines length are presented in Table A.2. The line between the bus 21 and the bus 22 has a 0.5 km. Therefore, the simulator was not able to run this line with distributed parameters.

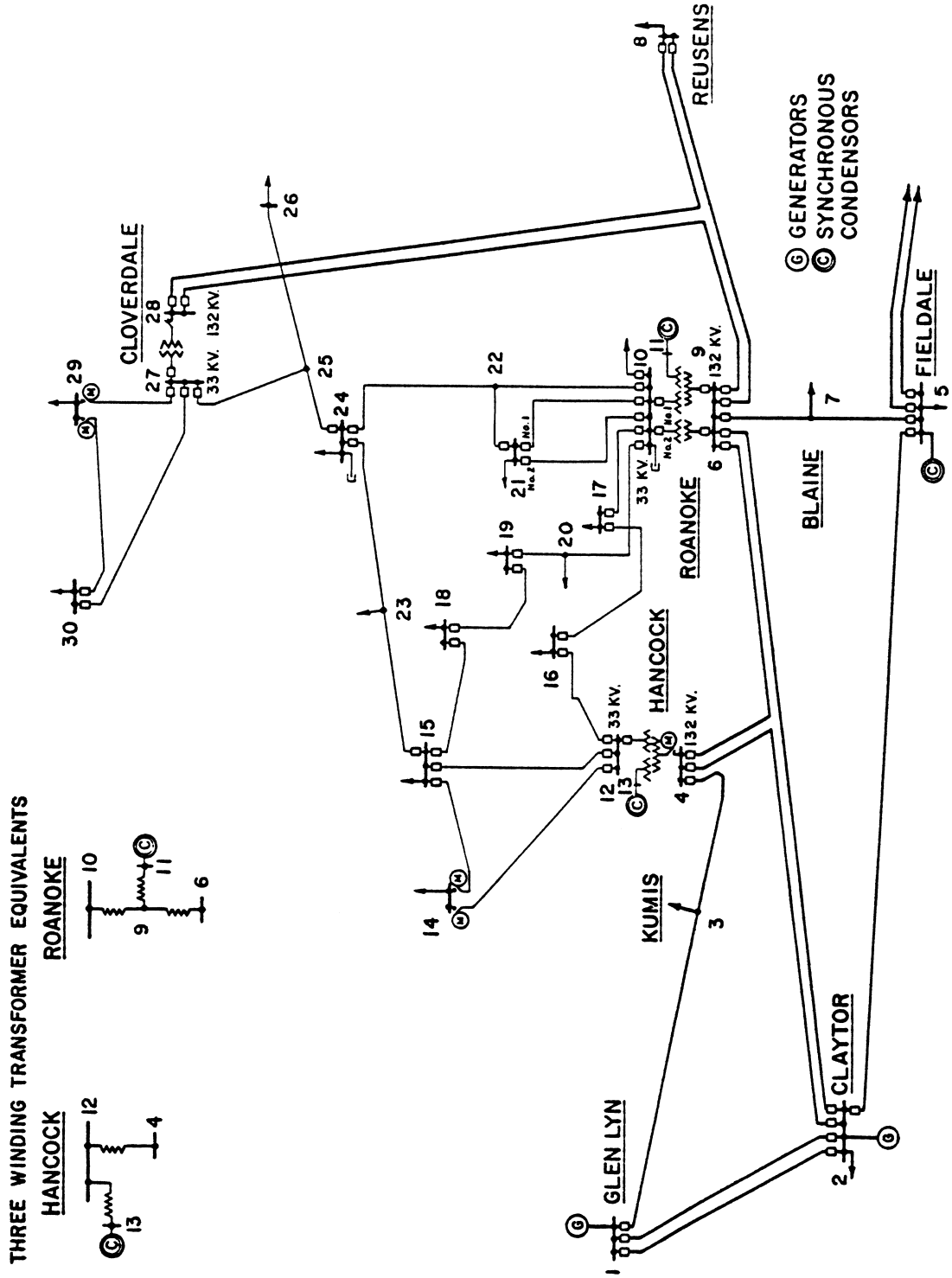

Figure A.1: IEEE 30 bus test system topology.

Bus number	Bus name	Load flow	Type	Final voltage	Final angle	Load MW	Load MVAR	Generation MW	Generation MVAR	Base KV	Desired voltage	Maximum MVAR	Minimum MVAR	Shunt susceptance
1	Glen Lyn	132	3	1.06	0	0	0	260.2	-16.1	132	1.06	0	0	0
2	Claytor	132	2	1.043	-5.48	21.7	12.7	40	50	132	1.045	50	-40	0
3	Kumis	132	0	1.021	-7.96	2.4	1.2	0	0	132	0	0	0	0
4	Hancock	132	0	1.012	-9.62	7.6	1.6	0	0	132	0	0	0	0
5	Fieldale	132	2	1.01	-14.37	94.2	19	0	37	132	1.01	40	-40	0
6	Roanoke	132	0	1.01	-11.34	0	0	0	0	132	0	0	0	0
7	Blaine	132	0	1.002	-13.12	22.8	10.9	0	0	132	0	0	0	0
8	Reusens	132	2	1.01	-12.1	30	30	0	37.3	132	1.01	40	-10	0
9	Roanoke	1	0	1.051	-14.38	0	0	0	0	1	0	0	0	0
10	Roanoke	33	0	1.045	-15.97	5.8	2	0	0	33	0	0	0	0.19
11	Roanoke	11	2	1.082	-14.39	0	0	0	16.2	11	1.082	24	-6	0
12	Hancock	33	0	1.057	-15.24	11.2	7.5	0	0	33	0	0	0	0
13	Hancock	11	2	1.071	-15.24	0	0	0	10.6	11	1.071	24	-6	0
14	Bus 14	33	0	1.042	-16.13	6.2	1.6	0	0	33	0	0	0	0
15	Bus 15	33	0	1.038	-16.22	8.2	2.5	0	0	33	0	0	0	0
16	Bus 16	33	0	1.045	-15.83	3.5	1.8	0	0	33	0	0	0	0
17	Bus 17	33	0	1.04	-16.14	9	5.8	0	0	33	0	0	0	0
18	Bus 18	33	0	1.028	-16.82	3.2	0.9	0	0	33	0	0	0	0
19	Bus 19	33	0	1.026	-17	9.5	3.4	0	0	33	0	0	0	0
20	Bus 20	33	0	1.03	-16.8	2.2	0.7	0	0	33	0	0	0	0
21	Bus 21	33	0	1.033	-16.42	17.5	11.2	0	0	33	0	0	0	0
22	Bus 22	33	0	1.033	-16.41	0	0	0	0	33	0	0	0	0
23	Bus 23	33	0	1.027	-16.61	3.2	1.6	0	0	33	0	0	0	0
24	Bus 24	33	0	1.021	-16.78	8.7	6.7	0	0	33	0	0	0	0.043
25	Bus 25	33	0	1.017	-16.35	0	0	0	0	33	0	0	0	0
26	Bus 26	33	0	1	-16.77	3.5	2.3	0	0	33	0	0	0	0
27	Cloverdle	33	0	1.023	-15.82	0	0	0	0	33	0	0	0	0
28	Cloverdle	132	0	1.007	-11.97	0	0	0	0	132	0	0	0	0
29	Bus 29	33	0	1.003	-17.06	2.4	0.9	0	0	33	0	0	0	0
30	Bus 30	33	0	0.992	-17.94	10.6	1.9	0	0	33	0	0	0	0

Figure A.2: Data bus from IEEE 30 bus test system.

Bus number	Bus number	Branch resistance	Branch reactance	Line charging	Transformer ratio
1	2	0.0192	0.0575	0.0528	0
1	3	0.0452	0.1652	0.0408	0
2	4	0.057	0.1737	0.0368	0
3	4	0.0132	0.0379	0.0084	0
2	5	0.0472	0.1983	0.0418	0
2	6	0.0581	0.1763	0.0374	0
4	6	0.0119	0.0414	0.009	0
5	7	0.046	0.116	0.0204	0
6	7	0.0267	0.082	0.017	0
6	8	0.012	0.042	0.009	0
6	9	0	0.208	0	0.978
6	10	0	0.556	0	0.969
9	11	0	0.208	0	0
9	10	0	0.11	0	0
4	12	0	0.256	0	0.932
12	13	0	0.14	0	0
12	14	0.1231	0.2559	0	0
12	15	0.0662	0.1304	0	0
12	16	0.0945	0.1987	0	0
14	15	0.221	0.1997	0	0
16	17	0.0524	0.1923	0	0
15	18	0.1073	0.2185	0	0
18	19	0.0639	0.1292	0	0
19	20	0.034	0.068	0	0
10	20	0.0936	0.209	0	0
10	17	0.0324	0.0845	0	0
10	21	0.0348	0.0749	0	0
10	22	0.0727	0.1499	0	0
21	22	0.0116	0.0236	0	0
15	23	0.1	0.202	0	0
22	24	0.115	0.179	0	0
23	24	0.132	0.27	0	0
24	25	0.1885	0.3292	0	0
25	26	0.2544	0.38	0	0
25	27	0.1093	0.2087	0	0
28	27	0	0.396	0	0.968
27	29	0.2198	0.4153	0	0
27	30	0.3202	0.6027	0	0
29	30	0.2399	0.4533	0	0
8	28	0.0636	0.2	0.0428	0
6	28	0.0169	0.0599	0.013	0

Figure A.3: Branch data from IEEE 30 bus test system.

Table A.1: Lines distributed parameters.

Linha (Bus-Bus)	Positive Sequence Paramiters			Zero Sequence Paramiters		
	Resistance (ohm/km)	Inductance (mH/km)	Capacitance (nF/km)	Resistance (ohm/km)	Inductance (mH/km)	Capacitance (nF/km)
1-2	0.1916	1.421	8.221	0.3934	3.870	5.646
1-3; 2-4; 2-5; 2-6; 3-4; 4-6; 5-7; 6-28; 6-7; 6-8; 8-28	0.1913	1.332	8.728	0.5009	4.730	5.779
10-17; 10-20; 10-21; 10-22; 12-14; 12-15; 12-16; 19-20	0.1702	1.031	11.407	0.3418	2.877	5.355
14-15; 15-18; 15-23; 16-17; 18-19; 22-24; 23-24; 24-25; 25-26; 25-27; 27-29; 27-30; 29-30	0.4263	1.129	10.374	0.7276	3.345	5.051

Table A.2: Lines length.

Line	1-2	1-3	2-4	2-5	2-6	3-4	4-6	5-7	6-28	6-7
Length (km)	14.25	41.67	40.08	44.62	39.67	8.53	9.32	26.1	13.48	18.45
Line	6-8	8-28	10-17	10-20	10-21	10-22	12-14	12-15	12-16	19-20
Length (km)	9.45	45.0	1.78	4.4	1.58	3.16	5.0	2.75	4.18	1.43
Line	14-15	15-18	15-23	16-17	18-19	22-24	23-24	24-25	25-26	25-27
Length (km)	3.71	4.06	3.75	3.59	2.4	3.32	5.01	6.11	7.05	3.87
Line	27-29	27-30	29-30							
Length (km)	7.71	11.19	8.41							

A.2 Doubly-Fed Electric Machine - DFIG

The topology of the DFIG is depicted in Figure A.4, with the back-to-back converter connected to the grid by the grid side converter (GSC) and in the opposite side connected to the rotor windings by the rotor side converter (RSC). The stator windings are connected directly to the electrical grid (TAVEIROS; BARROS; BEZERRA COSTA, 2013). The DFIG parameters are specified in Table A.3 (YANG et al., 2010).

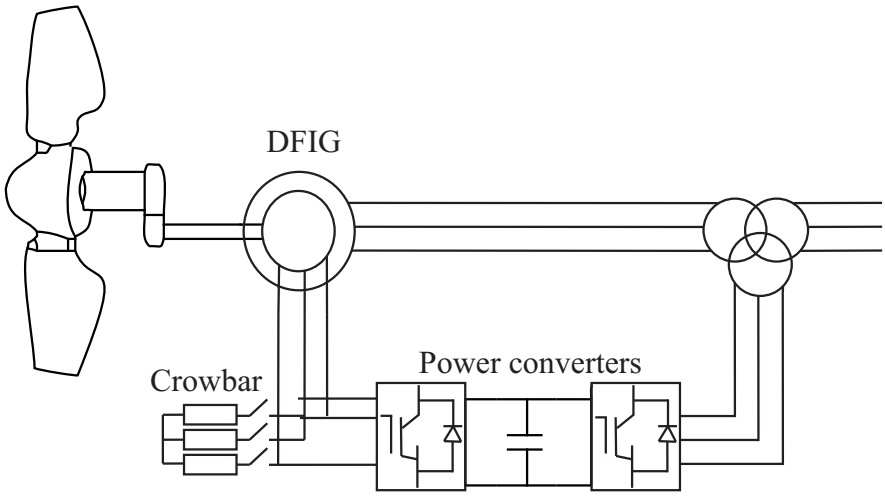

Figure A.4: DFIG topology.

Table A.3: DFIG parameters.

Param.	Value	Description
V_s	220 V	Stator voltage
S_n	1.5 kVA	Stator Power
p	2	Pole pairs
W_n	1800 rpm	Synchronous speed
R_s	0.993 Ω	Stator resistance
R_r	0.877 Ω	Rotor resistance
L_r	0.09327 H	Rotor inductance
L_s	0.08916 H	Stator inductance
L_m	0.0863 H	Mag. inductance
L_{si}	0.0575 H	Leakage inductance
J	0.0265 V	Inertia
C	430 μC	DC capacitor
R_f	0.4 Ω	Filter resistance
L_f	75 mH	Filter inductance
n	3	Turns ratio